THESIS FOR THE DEGREE OF DOCTOR OF ENGINEERING

Atomic Scale Degradation of Zirconium Alloys for Nuclear Applications

GUSTAV SUNDELL

CHALMERS

Department of Applied Physics

CHALMERS UNIVERSITY OF TECHNOLOGY

Göteborg, Sweden 2015

Atomic Scale Degradation of Zirconium Alloys for Nuclear Applications
GUSTAV SUNDELL

ISBN 978-91-7597-178-0
Doktorsavhandlingar vid Chalmers tekniska högskola
Ny serie nr 3859
ISSN 0346-718X

Department of Applied Physics
Chalmers University of Technology
SE-412 96 Gothenburg
Sweden
Telephone + 46 (0)31-772 1000

Cover:
Top left: APT reconstruction of OD^+ ions localized along an oxide grain boundary in Zr-2.5Nb. Center: HAADF STEM micrograph of the barrier oxide in autoclave-corroded Zircaloy-2. Top right: Grain boundary segregation of Fe (purple) and Ni (green) to grain boundaries in the metal (orange) and the oxide (blue). Bottom center: Distribution of Fe (blue), Cr (purple) and Sn (green) around a dislocation <c>-loop in Zircaloy-2 metal matrix subjected to 9 cycles of in-reactor exposure. Note that the APT reconstructions and the STEM micrograph all come from different samples.

Printed by:
Chalmers Reproservice
Gothenburg, Sweden 2015

Atomic Scale Degradation of Zirconium Alloys for Nuclear Applications

Gustav Sundell
Department of Applied Physics
Chalmers University of Technology

Abstract

Due to their low thermal neutron capture cross-section, zirconium alloys are widely used in the nuclear industry as fuel cladding and for structural components. The lifetime of the fuel assemblies in the reactors is primarily dictated by the ability of the cladding to withstand oxidation and hydrogen pick-up from the coolant water and radiation damage induced by the neutron flux.

In order to study the hydrogenation and irradiation damage of zirconium on the atomic scale, atom probe tomography (APT) is utilized. This technique offers some unique virtues for nanometer scale materials analysis, such as equal sensitivity to all elements and near-atomic resolution. However, as APT has rarely been used for hydrogen studies previously, methods for accurate qualitative and quantitative analysis need to be developed.

In this thesis, methods to control adsorption of hydrogen onto the APT specimen are explored. Techniques for hydrogen measurement are further developed using deuterium, whereby it is shown that hydrogen enters the alloy through grain boundaries in the oxide scale. A model for mitigation of hydrogen pick-up is proposed, in which oxide grain boundaries are decorated with transition metal alloying elements such as Fe and Ni, which affects the probability of reducing ingressing protons to form inert H_2 gas.

Zr alloys incur irradiation damage when subjected to the neutron flux in the reactor core, dissolving secondary phase particles and generating dislocation loops that embrittle the material. By studying the microstructure on the atomic scale before and after prolonged in-rector exposure, it is shown how the alloying elements in Zr interact with the irradiation-induced lattice defects.

Keywords: Atom probe tomography, Hydrogen pick-up, Hydrogen microanalysis, Corrosion, Zirconium alloys, Irradiation damage.

“With the breakdown of the medieval system, the gods of chaos, lunacy, and bad taste gained ascendancy.”

— John Kennedy Toole, *A Confederacy of Dunces*

Preface

The research work in this thesis was carried out at the Materials Microstructure Division at the Department of Applied Physics, Chalmers University of Technology, Göteborg, Sweden, during the period October 2010 to March 2015, under supervision of Professor Hans-Olof Andrén and co-supervision of Dr Mattias Thuvander.

List of appended papers

I. *Hydrogen analysis in APT: methods to control adsorption and dissociation of H_2*
G. Sundell, M. Thuvander and H.-O. Andrén
Ultramicroscopy, Vol. 132, 2013, pp. 285-289

II. *Enrichment of Fe and Ni at metal and oxide grain boundaries in corroded Zircaloy-2*
G. Sundell, M. Thuvander and H.-O. Andrén
Corrosion Science, Vol. 65, 2012, pp. 10-12

III. *Oxidation Mechanism in Zircaloy-2 – The Effect of SPP Size Distribution*
P. Tejland, H.-O. Andrén, G. Sundell, M. Thuvander, B. Josefsson, L. Hallstadius, M. Ivermark and M. Dahlbäck
Zirconium in the Nuclear Industry: 17th International Symposium, STP 1543, 2014, pp. 373-403

IV. *Tin clustering and precipitation in the oxide during autoclave corrosion of Zircaloy-2*
G. Sundell, M. Thuvander and H.-O. Andrén
Journal of Nuclear Materials, Vol. 456, 2015, pp. 409-414

V. *Toward a Comprehensive Mechanistic Understanding of Hydrogen Uptake in Zirconium Alloys by Combining Atom Probe Analysis with Electronic Structure Calculations*
M. Lindgren, G. Sundell, I. Panas, L. Hallstadius, M. Thuvander and H.-O. Andrén
Zirconium in the Nuclear Industry: 17th International Symposium, STP 1543, 2014, pp. 515-539

VI. *Direct observation of hydrogen and deuterium in oxide grain boundaries in corroded Zirconium alloys*
G. Sundell, M. Thuvander, A.K. Yatim, H. Nordin and H.-O. Andrén
Corrosion Science, Vol. 90, 2015, pp. 1-4

VII. *Barrier oxide chemistry and hydrogen pick-up mechanisms in zirconium alloys*
G. Sundell, M. Thuvander and H.-O. Andrén
To be submitted

VIII. *Influence of heat treatment on the solute concentrations in Zircaloy-2*
G. Sundell, M. Thuvander and H.-O. Andrén
To be submitted

IX. *Redistribution of alloying elements in Zircaloy-2 after in-reactor exposure*
G. Sundell, M. Thuvander, P. Tejland, M. Dahlbäck, L. Hallstadius and H.-O. Andrén
Journal of Nuclear Materials, Vol. 454, 2014, pp. 178-185

I wrote all the papers and did all the experimental work, with the exception of Paper III and V. In Paper III and V, I performed and evaluated the atom probe analyses and wrote the atom probe sections of the papers.

I also contributed to the following papers:

I. *Atom probe tomography of Oxide Scales*
K. Stiller, L. Viskari, G. Sundell, F. Liu, M. Thuvander, H.-O. Andrén, D. J. Larson, T. Prosa, D. Reinhard
Oxidation of Metals. Vol. 79, 2013, pp. 227-238

II. *Atomically Resolved Tissue Integration*
J. Karlsson, G. Sundell, M. Thuvander, M. Andersson
Nano Letters, Vol 14, 2014, pp. 4220-4223

TABLE OF CONTENTS

1. Introduction

1.1 Background

Perhaps the most important challenge that science and engineering face in the 21st century is to satisfy the rising energy demand in the world. Rapid economic growth in developing countries calls for improved standards of living, accommodated partly by increased electricity and fuel consumption. At the same time, consciousness of the devastating effects of climate change, caused by emission of greenhouse gases into the atmosphere, is now starting to exert influence over energy policies of governments worldwide. This has led to a surge of interest in renewable sources of energy over the past decades, such as photovoltaics[1], wind power[2] and biomass combustion[3].

While some of these techniques show great promise, renewable sources of energy are still far from being capable of replacing fossil fuels. This has brought renewed interest in nuclear power as an interim solution for electricity generation. Nuclear power has the advantage of producing significantly less carbon dioxide than fossil fuel combustion processes. Life cycle analysis shows that nuclear power is comparable to renewable energy sources in terms of emissions[4]. New generations of nuclear plants offer substantial improvements in terms of efficiency as well as safety. This has prompted many governments to expand their nuclear programs, and many countries are now constructing new Generation III-type plants. Today, more than 25 new reactors are under construction only in China[5]. Large-scale research projects are carried out across the world to develop new Generation IV technologies for nuclear power, which will see further improvements in thermal efficiency and fuel usage. The vast majority of reactors in operation today, however, are of type Generation II. Generation II reactors were first taken into operation in the 1950s, but commercial usage did not start until the late 1960s. Continuous improvements to the design have been made since, which has prolonged the lifetime of these early reactor types.

The efficiency of a nuclear plant is limited mainly by the temperature of the coolant in the reactor. Higher coolant temperatures increase the amount of available work that can be extracted from the system, in accordance with Carnot's theorem[6]. Another factor that can be improved is increasing the burn-up of the reactor fuel. Higher burn-ups increase the total energy output from the fuel, and, crucially, means that the number of the spent fuel assemblies decreases for a given energy output. The longer the fuel stays in the reactor, the less harmful material is left to dispose of when the fuel cycles are ended. Such enhancements of the nuclear plant performance put severe strains on the structural materials in the reactor. The components have to withstand heavy radiation doses as well as an intensely corrosive environment during their time of operation. This requires resilient mechanical properties in combination with good corrosion resistance.

Zirconium alloys were selected at an early stage for usage in nuclear reactor cores, as the low thermal neutron capture cross-section of zirconium prevents it from interfering with the neutron flux and contributes to a good neutron economy in the

reactor. They are currently utilized in virtually all nuclear reactors, as fuel cladding as well as structural parts in the core.

Two of the main limiting factors for the lifetime of the fuel cladding are the oxidation and the hydrogen pick-up, which are consequences of the waterside corrosion process in the reactor. Hydrogen pick-up causes serious embrittlement of the alloy and damages its advantageous corrosion properties. Despite several decades of research, the mechanism of hydrogen pick-up in zirconium alloys is yet to be fully understood. Many empirical studies have been carried out on the subject, and new alloys have been developed based on a trial-and-error approach of varying heat treatments and additions of alloying elements. In order to ultimately address the problem of hydrogenation of zirconium alloys, a mechanistic understanding of the fundamental principles that govern hydrogen uptake is needed.

Another critical degradation phenomenon of zirconium alloys is irradiation damage. Elastic interaction between fast neutrons from the fission process and the cladding causes changes in the microstructure that lead to hardening and eventually dimensional changes. This can have severe implications for the operational safety of the plant, as it may impede insertion of control blades into the core. Development of new alloys with more resilient properties at high burnups requires knowledge about the interaction between crystal defects, induced by neutron irradiation, and added alloying elements in the materials.

1.2 Aim of this study

This work is performed as part of the MUZIC-2 program, which is a collaborative project between industry and the academic partners University of Oxford, University of Manchester, Imperial College London, Penn State University and Chalmers University of Technology, aimed at elucidating the mechanisms that govern hydrogen uptake in zirconium alloys. The experimental work at Chalmers is focused on atom probe tomography analysis of fuel cladding materials.

The objectives of this study are:

- Investigate the possibility to perform qualitative and quantitative hydrogen analysis using atom probe tomography.

- Develop methods to perform microanalysis of the regions that are of importance for corrosion and hydriding of zirconium alloys.

- Study the distribution of alloying elements in the barrier oxide and around the metal-oxide interface of autoclaved zirconium alloys.

- Utilize the knowledge gained from atom probe analysis to formulate a hypothesis for the mechanisms behind hydrogen pick-up.

- Elucidate the evolution of alloying element distribution during neutron irradiation, with the view to individually establish their impact on in-reactor corrosion and irradiation damage.

2. Zirconium in the nuclear industry

2.1 Nuclear reactors

In a nuclear reactor controlled nuclear fission reactions take place, which generates heat through a series of nuclear chain reactions. Heat from the fission process is passed on to a coolant, typically water, which is used to produce steam that runs through a steam turbine to produce electric power that can be utilized for power distribution or propulsion. Fission is initiated and sustained by a neutron flux, which must be controlled during operation. In light water reactors (LWR), neutron flux in the reactor is regulated by the insertion of control rods into the reactor core or by injection of neutron absorbers in the coolant. Various designs exist in terms of moderator, fuel and coolant. In Swedish nuclear plants, only LWR are used where fast neutrons are slowed down in the fluid to become thermal neutrons, thereby triggering further fission. In the LWR design, a significant portion of thermal neutrons are absorbed by the water, which means that natural uranium cannot be used as fuel. Enrichment of the fissile uranium-235 isotope in the fuel is therefore necessary in order to sustain the chain reactions.

Two types of LWR reactors are in operation in Sweden; pressurized water reactors (PWR) and boiling water reactors (BWR). In PWRs the coolant is kept in liquid state at high pressures (usually around 150 bar[7]) in the reactor core, and passes on thermal energy to a secondary water circuit in a steam generator. A pressurizer regulates pressure in the loop, by adjusting the temperature of the coolant with electrical heaters. A vertical temperature gradient is present along the fuel bundles where the temperature at the bottom is around 275 °C, and the water is heated to 315 °C at the top[8]. In BWRs the water is brought to boil in the core and the electricity generation in the turbine occurs in the primary water circuit. BWRs operate at a significantly lower pressure (around 75 bar) than PWRs, which means that the boiling point of the coolant is reduced to about 285 °C[9]. A schematic illustration of a boiling water reactor is presented in Figure 2.1.

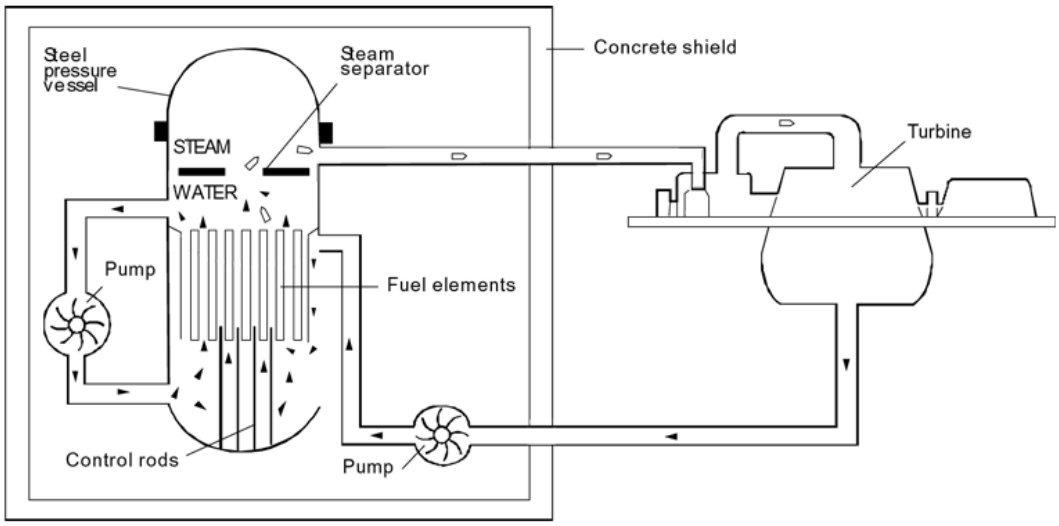

Figure 2.1: Schematics of a boiling water reactor[5].

The fuel in the Swedish reactors comprises pellets of uranium dioxide that is enriched in the fissionable U-235 isotope. The pellets are inserted into zirconium alloy cladding tubes of approximately 10 mm in diameter. The interior of the tube is sealed and pressurized with helium to reduce potential pellet-cladding interaction and improve thermal conductivity.

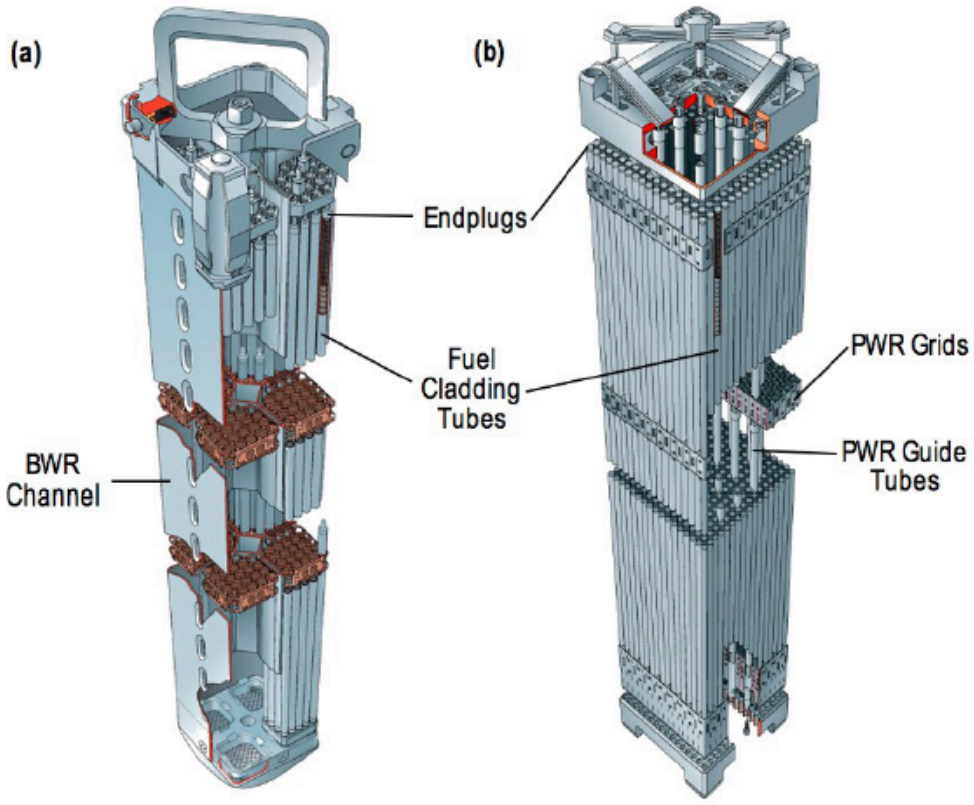

Figure 2.2: BWR (left) and PWR (right) fuel assemblies (courtesy of Westinghouse Electric Sweden AB).

Tubes are grouped together in bundles called fuel assemblies. BWR fuel assemblies are each enclosed in a box to ensure water and steam flow stability. Stainless steel control blades, containing compartments with highly neutron-absorbing material, can be inserted in the fuel assemblies to regulate the neutron flux in the reactor.
BWR and PWR fuel assemblies are presented in Figure 2.2.

2.2 Fuel cladding alloys

The aggressive environment in the reactor puts extreme requirements on the fuel cladding material. It has to withstand fission products from the inside and water at temperatures ranging from 280-350°C at high pressure containing oxidizing radiolysis products from the outer surface[9]. In addition it must not only endure collisions with fast (>1 MeV) neutrons, but also interfere as little as possible with the thermal neutron flux, in order to maintain high neutron efficiency in the reactor. Zirconium has a very low thermal neutron capture cross-section[10], which means that it is nearly transparent for low energy neutrons that have high probability of causing fission of the fuel. This

made it an attractive candidate for usage in early nuclear reactor cores. Pure zirconium, however, has relatively poor corrosion resistance and insufficient mechanical strength for usage in structural components. Experiments with Sn addition led to the development Zircaloy-1 for cladding in early BWR, but this alloy was soon abandoned in favor of Zircaloy-2. This alloy contains small amounts of Fe, Cr and Ni in addition to Sn, which significantly improved corrosion resistance. Zircaloy-2 is still widely used as BWR cladding, and subtle tinkering with heat treatments and chemistry has enabled improvements of its performance over the years.

PWR reactors have seen a larger number of zirconium alloys, but the most common in Europe today are ZIRLO™ (additions of Sn, Nb and Fe), M5™ (Nb) and Zircaloy-4 (Sn, Fe, Cr). Graphite-moderated RBMK reactors in Russia and heavy-water moderated CANDU reactors in Canada primarily use binary Zr-Nb alloys.

Table 2.1: Some common Zr alloys for nuclear applications and their alloying elements. Secondary phase particles (SPPs) found in the materials are also listed.

Alloy		Nominal content (wt%)						
	Usage	Sn	Fe	Ni	Nb	Cr	O	SPPs
Zircaloy-2	BWR, CANDU	1,2-1,7	0,07-0,20	0,03-0,08	-	0,05-0,15	0,125	$Zr(Fe,Cr)_2$ - $Zr_2(Fe,Ni)$
Zircaloy-4	BWR, PWR, CANDU	1,2-1,7	0,18-0,24	-	-	0,07-0,13	0,125	$Zr(Fe,Cr)_2$
M5	PWR	-	<500 ppm	-	0,8-1,2	-	0,125	β-Nb - $Zr(Nb,Fe)_2$
Zr-2.5 Nb	CANDU, RBMK	-	-	-	2,4-2,8	-	0,125	Nb enriched β-Zr (metastable)
ZIRLO	PWR	1,0-1,1	0,09-0,10	-	1,0-1,2	-	0,125	β-Nb - $(Zr,Nb)_2Fe$

In general, these alloys contain small amounts of trace elements, such as Si, P and C. Their solubility in α-zirconium is very low and they form small precipitates. The exact role of these particles in corrosion process has not been clearly established.

2.3 Microstructure and heat treatments

Pure solid zirconium exists in two phases; a hexagonal close-packed (hcp) structure at ambient temperature (α-zirconium), and a body centered cubic (bcc) structure at temperatures above 865°C (β-zirconium)[9]. Thus the relevant crystal structure for normal operation nuclear applications is the α-phase. Lattice parameters are $a = 0.323$ nm and $c = 0.515$ nm[11] which means that the lattice is compressed slightly in the c-direction with respect to the ideal hcp structure. A hexagonal unit cell is shown in Figure 2.3.

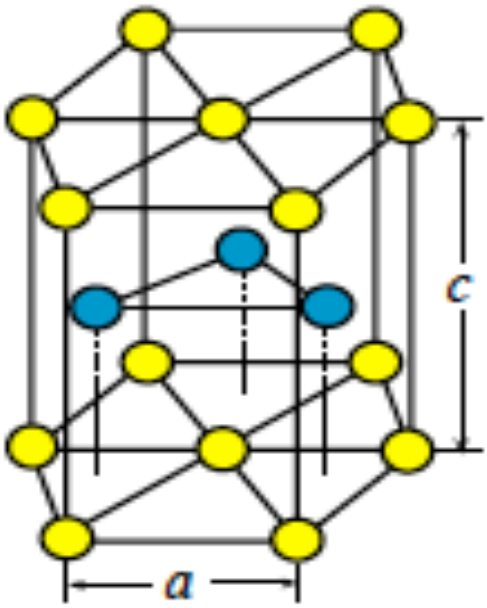

Figure 2.3: Hexagonal close packed unit cell[12].

Prolonged neutron irradiation leads to crystal growth in the basal plane and compression in the *c*-direction[13]. The hexagonal crystal structure gives the α-phase strongly anisotropic properties that must be accounted for in fuel cladding processing[14].

Zirconium alloys for fuel cladding applications are typically subjected to the following thermomechanical processing steps[9]:

- Hot forging in the β-phase at temperatures around 1000 °C. This dissolves secondary phase particles and gives rise to significant grain growth. Billets or slabs are formed.
- Water quenching from the β-phase at a temperature above 1000 °C. Upon quenching the β-grains undergo a bainitic or martensitic transformation to form α-lamellae. Alloying elements such as Fe, Cr and Ni are rejected by the α-front and precipitate as SPPs at the boundaries of the lamellae[15,16].
- Upper α-phase extrusion to form tubes (temperature 575-725°C.).
- A number of cold-rollings and subsequent anneals in vacuum at intermediate temperature (550-600 °C). Deformation of up to 80% is achieved where the final annealing leads to either a stress relieved (Zircaloy-4 cladding tubes) or a fully recrystallized state (Zircaloy-2 cladding tubes).

The resulting recrystallized microstructure in Zircaloy-2 cladding is highly textured with equiaxed grains. A characteristic pole figure for tube material is shown in Figure 2.4.

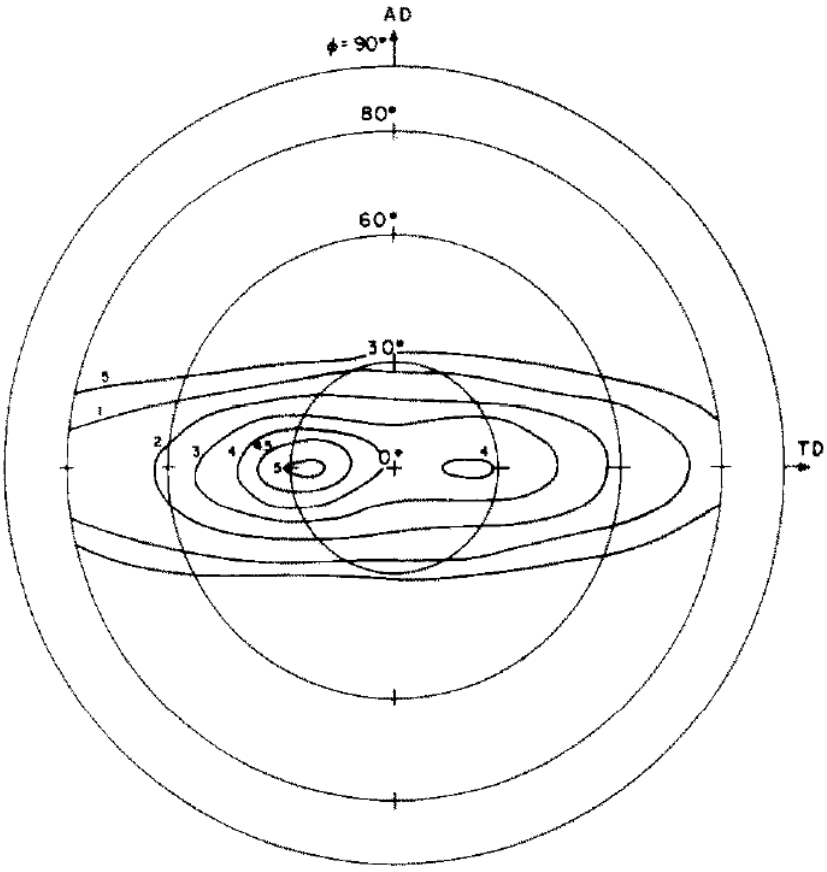

Figure 2.4: (0002) pole figure from Zircaloy-2. AD indicates the rolling direction (axial direction of the tube) and TD indicates the transverse direction (circumferential direction of the tube)[17].

The <c> axis lies in a plane perpendicular to the tube axis, often some 30 degrees from the radial direction (see Figure 4)[18], which improves the yield stress and makes the tubes more resistant to hoop stresses from internal pressure.

The size and distribution of SPPs are strongly dependent on the cold-rolling and annealing steps. This has led to some development work of heat treatments over the years in order to obtain optimal properties with regards to creep resistance and corrosion. Very subtle changes in SPP size in Zircaloy-2 can have a strong impact on hardness and corrosion properties[19,20].

Non-irradiated zirconium deforms plastically by activation of the principal dislocation glide system on prismatic planes in the <a>-directions[21,22], or by twinning[23]. Pyramidal slip may also occur at high temperatures or high deformation rates. In reactors the picture is more complicated, as irradiation-induced dislocation loops on prismatic planes constitute obstacles to the glide systems of the normal deformation modes. This can lead to the activation of dislocation channeling in the basal plane[24,25].

3. Corrosion behavior

3.1 Overview

One of the main limiting factors for the lifetime of zirconium fuel cladding tubes is corrosion. As a result, the oxidation properties of zirconium alloys have been studied extensively since the first commercial nuclear plants were taken into operation in the 1960's[26]. The native oxide that forms on Zr is monoclinic ZrO_2. The Zr-O phase diagram in presented in Figure 3.1. In ZrO_2 diffusion of oxygen is faster than diffusion of Zr, which results in an inward growing oxide scale[27]. The oxidation occurs by oxygen species generated in a water-splitting reaction at an oxide-water interface and has the overall corrosion reaction

$$Zr + 2\,H_2O \rightarrow ZrO_2 + 2H_2$$

The Pilling-Bedworth ratio is 1.55[28], causing a volume expansion that can only be accommodated by first deforming the underlying metal[29,30], and eventually stress relaxation by cracking of the oxide[31].

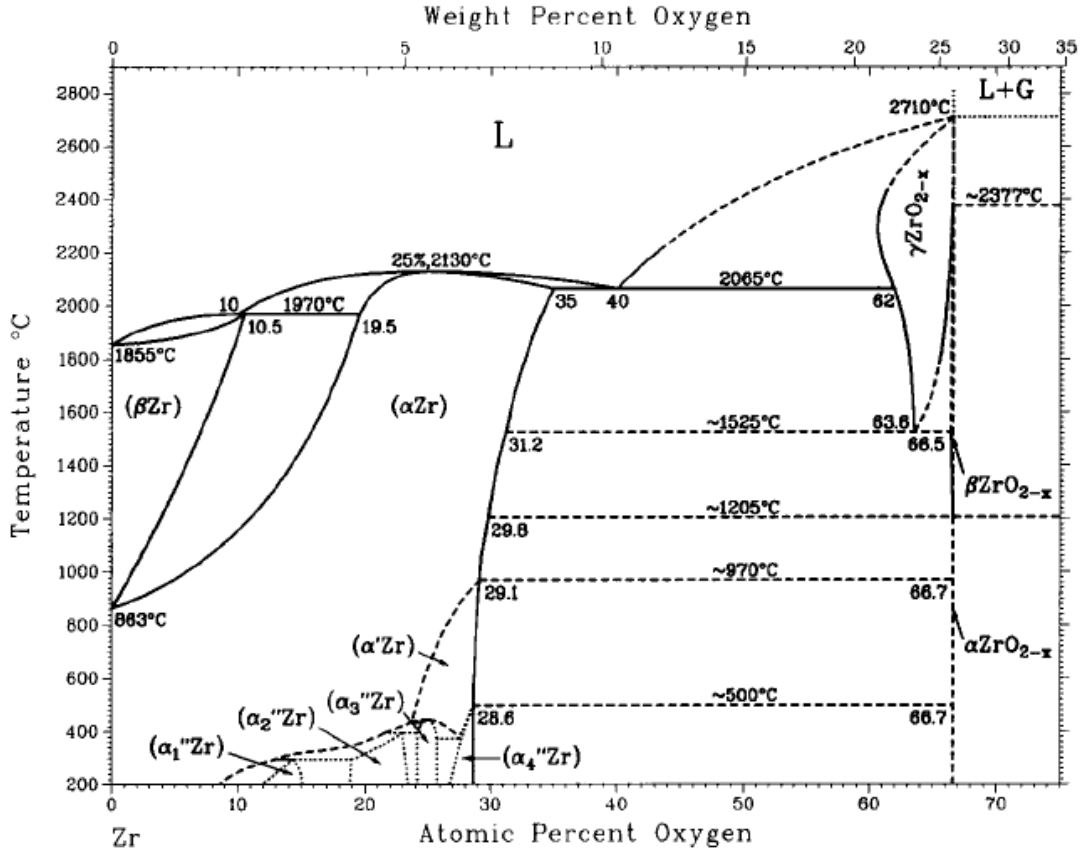

Figure 3.1: Zr-O binary phase diagram[32].

Unlike most structural materials, α-Zr has a rather high solubility of oxygen. At relevant temperatures for nuclear applications the solubility is approximately 29

at%[32]. Diffusion of oxygen in the metal is slower than in the oxide scale, which prevents oxygen saturation in the metal except for in the outermost regions[33].

3.2 Oxide Growth

The time dependence of the thickness of the ZrO_2 layer growing on top of a Zr alloy is usually described as $k\,t^n$ where k is a rate constant and n is typically smaller than 0.5, i.e. the rate is sub-parabolic[26]. This protective film stabilizes and collapses in a characteristic cyclic pattern (see Figure 3.2). Firstly a protective oxide is rapidly formed, slowing down growth significantly[34]. The appearance of the oxide is blackish at this stage, and grains are small and equiaxed[9]. Compressive stresses are high which leads to transformation of some monoclinic oxide to the high-pressure tetragonal oxide phase[35]. Upon further oxidation, monoclinic oxide with columnar morphology develops[36]. The column axes are perpendicular to the metal-oxide interface and have a width of approximately 25 nm[37]. The metal-oxide interface has a wavy morphology, which typically undulates with an amplitude of up to a few hundred nanometers for thinner oxides[38]. Various theories regarding the origin of these waves exist such as faster O^{2-} diffusion through certain oxide column grain boundaries[39], and SPP influence[40].

The protective oxide is stable up to a thickness of approximately 1.5-3 μm, depending on alloy and oxidation conditions, after which it breaks up and a rapid increase in growth rate occurs. This change in oxidation rate is referred to as *transition,* and this phenomenon has been studied extensively[41–45]. At this point, the fraction of tetragonal phase in the oxide decreases sharply[41]. Larger columnar grains that are elongated in a direction normal to the metal-oxide interface replace the small equiaxed grains[46].

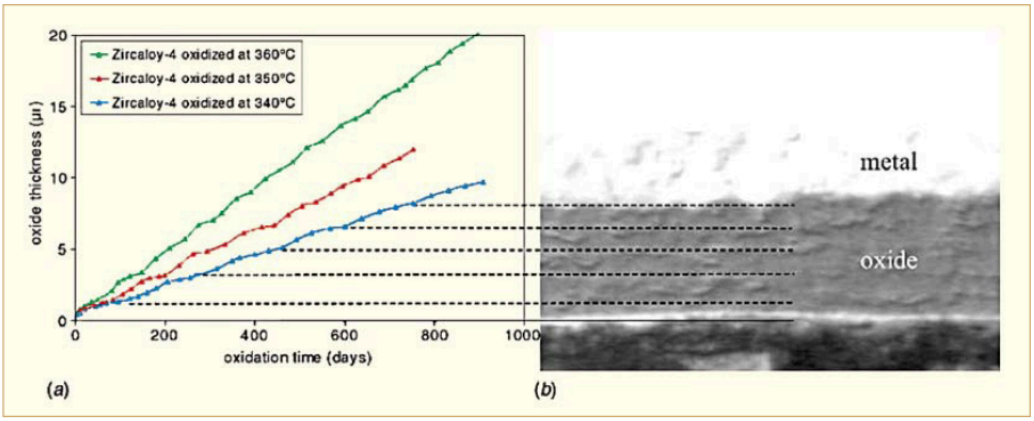

Figure 3.2: Cyclic growth rate of oxide scale on Zircaloy-4. Transitions are associated with cracks in the oxide[47].

These cycles of protective barrier oxide build-up, followed by collapse and rapid growth is repeated numerous times up until thicknesses of several tens, or even hundreds, of micrometers. Eventually a breakaway corrosion stage occurs[48], where the oxide offers no protection as large cracks and spallation will allow easy access for the

water to the metal-oxide interface[9]. Fuel bundles are removed from the reactor well in time before breakaway corrosion occurs.

In general, if the rate-limiting step of an oxidation process is dependent on solid-state diffusion of ionic or electronic species through an oxide scale, the thickness of the scale is proportional to the square-root of time[34,49,50]. Compliance with this parabolic rate law is often not observed in commercial zirconium alloys, which are in many cases closer to cubic kinetics[26]. This suggests the rate-limiting step may differ at different stages of the corrosion reaction. The oxide texture can have a large impact on the growth kinetics[46,51], which indicates that grain boundary diffusion is the dominating transport mechanism through the oxide[39,41].

In addition to the uniform corrosion, Zr alloys in BWR reactors may also suffer nodular corrosion[52]. This comprises nucleation of "blisters" of oxide that are associated with rapid growth and rupture of the uniform protective oxide. The problem of nodular corrosion is believed to be connected to large SPPs and has to a large extent been overcome by reducing SPP size[53,54].

3.3 Influence of alloying elements

Subtle differences in alloying elements can have an enormous impact on the corrosion behavior of the alloy[55]. What is true for fuel cladding in BWR may not necessarily be applicable in PWR plants[53]. Tin is added to virtually all LWR claddings, mainly for mechanical properties as it increases the yield strength of the alloy[9]. It is an α-stabilizer for Zr and is also known to stabilize the tetragonal ZrO_2 phase during corrosion[56]. Sn is fully soluble in the metal matrix as well as in the oxide, and does not form precipitates in commercial alloys. It has long been thought to improve the corrosion resistance[9]. However, this notion has been challenged in recent years[56,57]. One explanation for this is the presence of Sn(II) in the inner part of the oxide, which enhances oxygen diffusion[58,59]. In PWR alloys the trend in recent years is instead to reduce the Sn content. Examples of this are M5™ , Optimized ZIRLO™ and low Sn Zircaloy-4.

Niobium is known to delay transition[60]. However it appears that Nb-containing alloys oxidize faster in water vapor than the Nb-free Zircaloys, and they are hence not widely used in BWRs[61]. Nb diffuses very slowly in Zr, making the annealing time during the heat treatment very important[62]. The Zr matrix is typically supersaturated with Nb, which can lead to in-reactor precipitation of fine particles[63]. Nb in solution is proposed to constitute a dopant of the otherwise insulating ZrO_2 scale, which would increase the conductivity and provide faster electron transport[64]. If electron transport is indeed a rate-limiting step in the corrosion process, this should enhance corrosion of Nb-containing alloys.

Iron appears to have a very large impact on the corrosion resistance of Zr alloys. In Zircaloy-2 it forms precipitates with Cr and Ni, but is also soluble in very small amounts in the matrix[65]. This solubility has been subject to some discussion and its importance for the corrosion properties is debated[40,66]. The Fe-containing precipitates are more noble than Zr and they start to oxidize at some distance away from the

metal-oxide interface[42]. During this process Fe may diffuse out of the particle and form agglomerates of nearly pure iron oxide[67]. Like Nb, Fe in solution in the oxide is expected to increase the conductivity of the barrier oxide layer[36,42,52,68].

Chromium has a very low solubility in the Zr matrix and is only observed in Fe-containing SPPs in commercial alloys[69]. Corrosion studies have been performed on model alloys containing Cr but without Fe[55], where breakaway corrosion rates were attained with little protectiveness of the oxide layer. Clearly, synergistic effects between Fe and Cr are at play. Cr remains in the SPPs relatively far out in the oxide and as the particles are depleted of Fe they become amorphous[9,67].

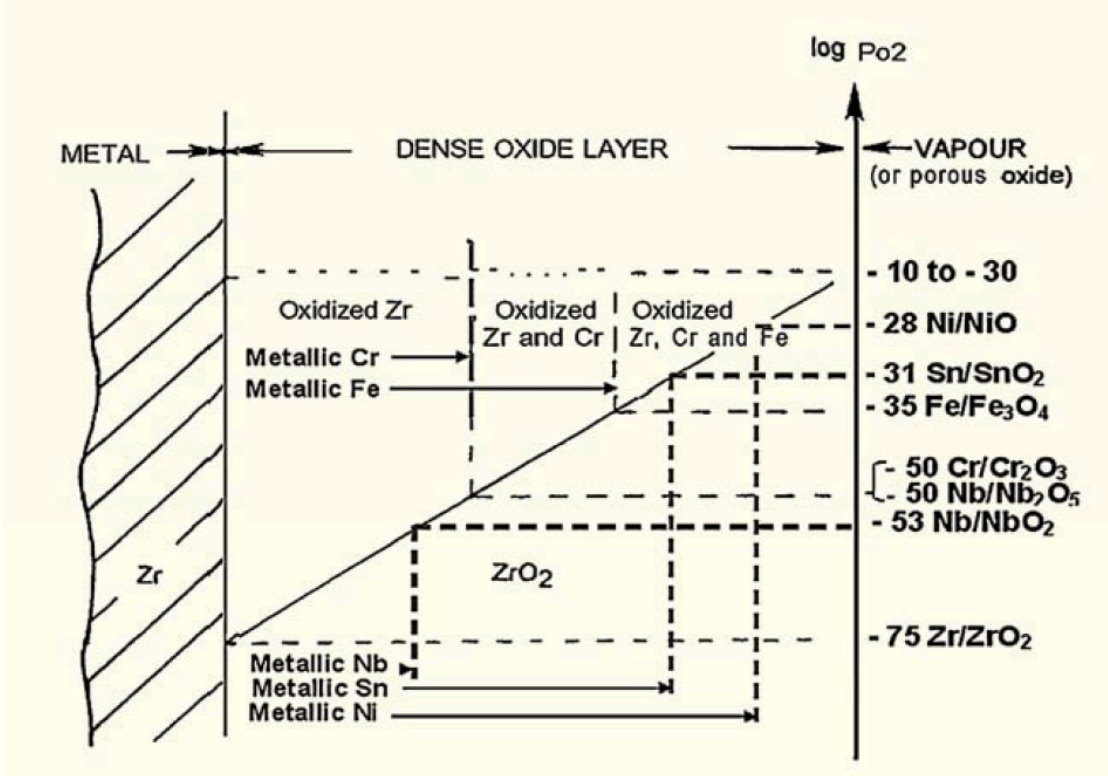

Figure 3.3: Stability (Ellingham) diagram of alloying elements in the oxide as a function of oxygen partial pressure[70].

Similarly to Fe and Cr, nickel has very low solubility in Zr and forms SPPs with Fe. It has been suggested that the distribution of Ni in the Zr matrix is non-uniform, which could make the alloy susceptible to nodular corrosion[71]. Nickel is the most noble of the transition metal alloying elements in zirconium and can thus be expected to oxidize reasonably far out in the oxide where the partial pressure of O_2 is higher[53]. The mobility of Ni in the oxide is reportedly low, and it tends not to migrate far from the original SPP region as it is oxidized[72]. It has been proposed that the delayed oxidation of precipitates may be associated with cracks and void formation in the oxide, thus reducing the protectiveness of the barrier layer[38]. The thermodynamic stability of the metallic species of some common alloying elements as a function of the partial pressure of O_2 is given in Figure 3.3[70].

3.4 Effects of irradiation

The fuel cladding will have little interaction with low energy thermal neutrons during operation in a nuclear reactor. However fast neutrons that have not been slowed down by the moderator will cause irradiation damage in Zr alloys[13]. The radiation will increase the number of vacancies in the Zr crystals, resulting in accelerated diffusion. As oxygen diffusion in the oxide is believed to be a possible rate limiting step, it was believed that similar processes would be at play in the oxide, leading to enhanced corrosion[73]. However, some studies of PWR cladding material does not give evidence for accelerated in-reactor corrosion, until after an oxide thickness of 5-6 μm was attained[26,74]. This implies that irradiation does not affect the presumably diffusion-controlled pre-transition corrosion rate. Instead it should be a factor in the transition mechanism where the oxide breaks down mechanically.

The conductivity of the oxide layer is often assumed to be higher in reactors than in autoclaves. β- and γ-radiation can be expected to cause excitations in the oxide scale, leading to increased electron mobility. One effect of the irradiation is amorphization and dissolution of precipitates[75–77]. Fe tends to migrate out of the SPPs in a similar fashion to the oxidation characteristics of Fe-containing precipitates. As SPPs are dissolving, elevated concentrations of alloying elements in the oxide grains are expected to act as dopants and enhance conductivity[72,78].

4. Hydrogen pickup

4.1 Overview

The overall corrosion reaction of zirconium (see section 3.1) also comprises the release of hydrogen. Some of the hydrogen that is formed in the water-splitting reaction will subsequently enter the Zr metal. To quantify this phenomenon a hydrogen pick-up fraction (HPUF) is defined as[79]

$$HPUF = \frac{H_{absorbed}}{H_{generated}}$$

This fraction may vary greatly in different alloys and reactor conditions. The mechanisms behind the process of hydrogenation are not known, despite the fact that the problem was recognized at an early stage.

4.2 Electrochemistry

Corrosion is an electrochemical process, which is governed by a set of redox reactions. Degradation of zirconium consists of a number of possible reactions and kinetic factors, which all can be rate determining given certain circumstances. The anodic reaction is

$$2O^{2-} + Zr \rightarrow ZrO_2 + 4e^-$$

A number of different cathodic reactions are plausible, such as[53]

$$2e^- + H_2O \rightarrow O^{2-} + 2H^0$$

$$2e^- + 2H^+ \rightarrow H_2$$

A water-splitting reaction may also occur at an oxide-water interface according to

$$V_O + H_2O \rightarrow O^{2-} + 2H^+$$

where V_O is an oxygen vacancy. In most cases, the majority of the hydrogen will diffuse out in the reactor water. Interestingly, the partial pressure of H_2 dissolved in the reactor coolant appears to have little effect on the hydrogen pick-up in the fuel cladding[53]. The third reaction is therefore likely beneficial in protecting the metal from hydrogen ingress, as once protons have been reduced, the resulting H_2 can be considered inert.

With the exception of nodular corrosion, Zr does not suffer crevice, pitting or other types of localized corrosion under normal reactor conditions. The anodic reaction can therefore be assumed to occur relatively homogeneously along the metal-oxide

interface. The anodic and cathodic reactions need not necessarily occur at the same site, which requires that an electronic or ionic current is facilitated. This means that the conductivity of the oxide is an important factor for the corrosion process. Pure ZrO_2 is a strong insulator with a band gap of 5.16 eV[80]. Reports do, however, claim that conductivity significantly increases during irradiation[81] and reactor operation[78]. This means that electrochemical considerations have to be taken into account when comparing autoclave and in-reactor corrosion mechanisms. Taylor proposed that the conductivity of the oxide governs where the cathodic sites for reduction are located, and suggested that an ideal oxide conductivity exists such that both oxidation rate and hydrogen pick-up can be minimized[82] (see Figure 4.1). Although a number of shrewd experimental schemes have been undertaken to elucidate the sites of the cathodic reactions[45,83–86], their locations around the oxide remain elusive.

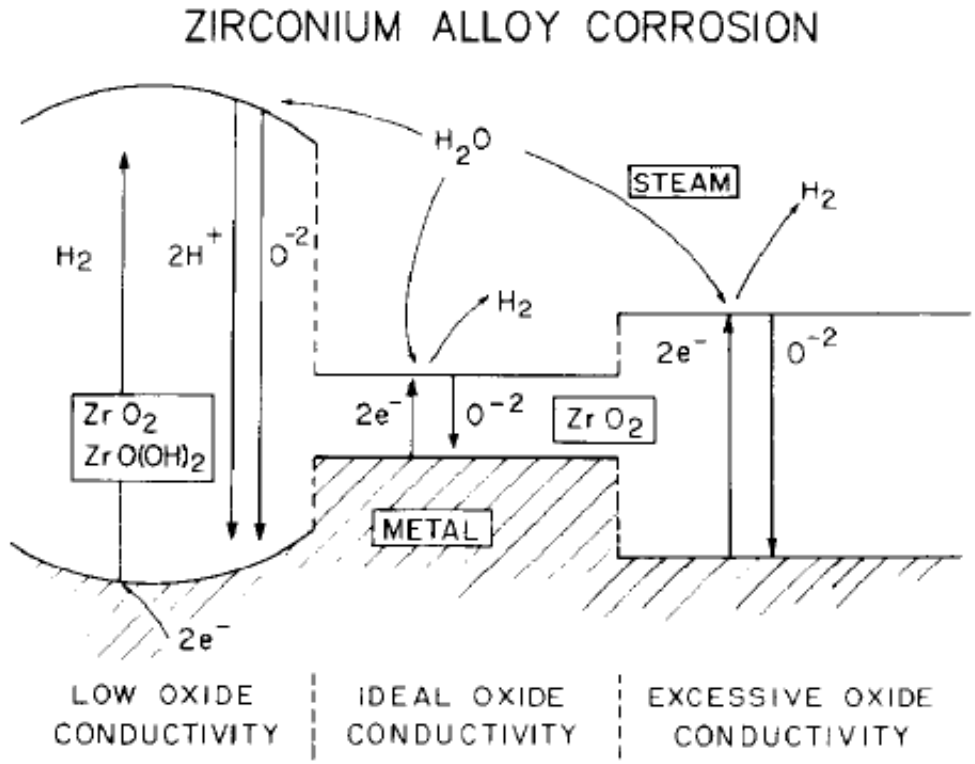

Figure 4.1: Corrosion kinetics at varying oxide conductivity, as suggested by Taylor[82].

4.3 Hydrides

Hydrogen has a relatively low solubility in α-Zr and will start precipitating as hydrides when the solubility limit is reached. The diffusivity of hydrogen in the Zr matrix is very high, which means that hydrides will not necessarily nucleate in the vicinity of the oxide but may also form in the interior of the cladding tube. The solubility is highly temperature dependent and differs significantly between operating and room temperatures. Under in-reactor conditions, a strong temperature gradient exists across the thickness of the cladding. The coolest part of the tube is the outer part, and this is consequently where the first hydrides will form during operation. The phase diagram for Zr-H is presented in Figure 4.2[87].

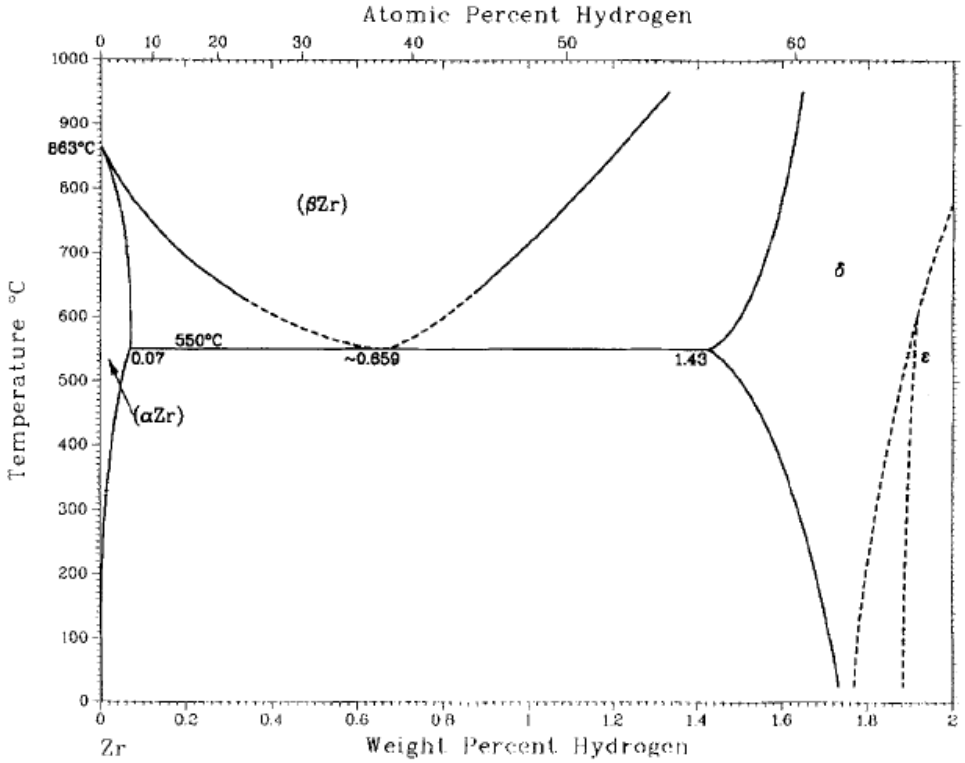

Figure 4.2: Zr-H binary phase diagram[87].

The most common hydride that is found in fuel cladding is the δ-hydride with typical stoichiometry $ZrH_{1.45\text{-}1.54}$. Some other metastable hydride phases also exist such as the γ-hydride (at high cooling rates) and the ζ-hydride, which is likely the first step of precipitation[88,89]. The γ-hydrides have the stoichiometry ZrH[90] and are of face centered tetragonal crystal structure. The ζ-hydride has the composition Zr_2H and is fully coherent with the α-Zr matrix[89]. At very high hydrogen concentrations, surpassing 70 atomic percent, an ε-hydride phase also exists[91].

The precipitation mechanism of hydrides has been studied extensively[92–94]. Upon rapid cooling or quenching the γ-hydrides form as platelets or needles parallel to the <1120> direction[93]. At lower cooling rates δ-hydrides form primarily at grain boundaries[94]. The precipitation is highly dependent on the stress situation in the tube, which is illustrated in Figure 4.3

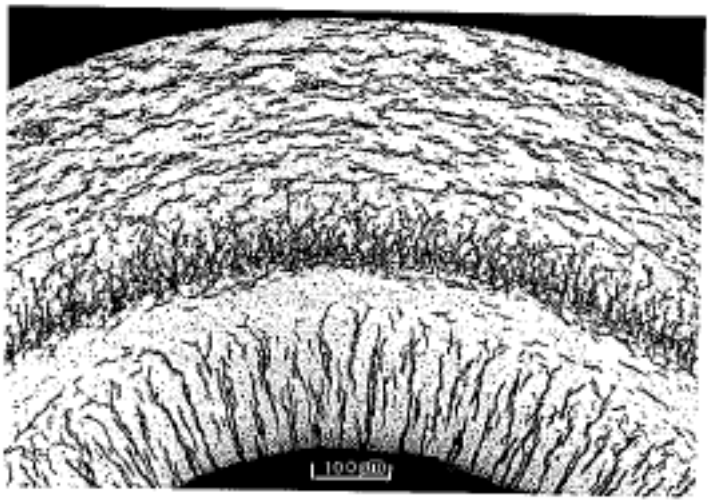

Figure 4.3: Delayed hydride cracking of a zirconium cladding tube[9]. Hydrides give dark contrast in the micrograph.

Here tensile hoop stresses, resulting from the internal pressure in the tube, have caused precipitation of hydrides in the radial direction. In the outer part of the tube hydrides precipitate in the basal plane, characteristic of the strong crystallographic texture[9].

At low burn-ups the hydrides are typically homogenously distributed throughout the tube, and have precipitated as the tube has cooled down from reactor temperature thus reducing the solubility. At high burn-ups hydrides tend to accumulate towards the outer surface of the tube, due to the temperature gradient during reactor operation that leads to the solubility limit being exceeded earlier there[95].

4.4 Effect on material properties

Hydrogen pick-up will have a significant detrimental impact on the material properties, both in-reactor and when handling the spent fuel assemblies. In reactor, hydrogen in solution will diffuse towards areas of low temperature or higher tensile stress[9]. The first case will lead to precipitation of a hydride rim near the outer surface when the terminal solubility is exceeded. Reports suggest that these hydrides may destroy the beneficial effects of the barrier oxide layer mechanically[96–98]. The formation of the hydride rim during operation is also reported to increase the corrosion rate with a factor of approximately 1.4[95]. Hydrogen diffusion towards areas of higher tensile stress may lead to delayed hydride cracking (DHC) of the tubes, which is a sub-critical crack growth mechanism in the material that must be avoided at any cost. DHC requires a crack in the material to be triggered, whereupon hydrogen in solution diffuses to the tip of the crack, where the stress is concentrated, and precipitates as brittle hydrides. Traces of DHC can be seen at the inner part of the tube in Figure 4.3, which is under tensile hoop stresses leading to crack propagation outwards in the radial direction[9].

A hydride rim also has a severe detrimental effect in case of strong power transients. Such transient may be a result of what is known as RIA (reactivity initiated accident), such as fuel pellet expansion or a sudden cladding temperature increase[95].

4.5 Factors influencing HPUF

Many phenomenological studies have been carried out both in reactor and in autoclave environments. The influence of various alloying elements has been tested systematically and reported in a number of publications[99–101] (see e.g. Figure 4.4).

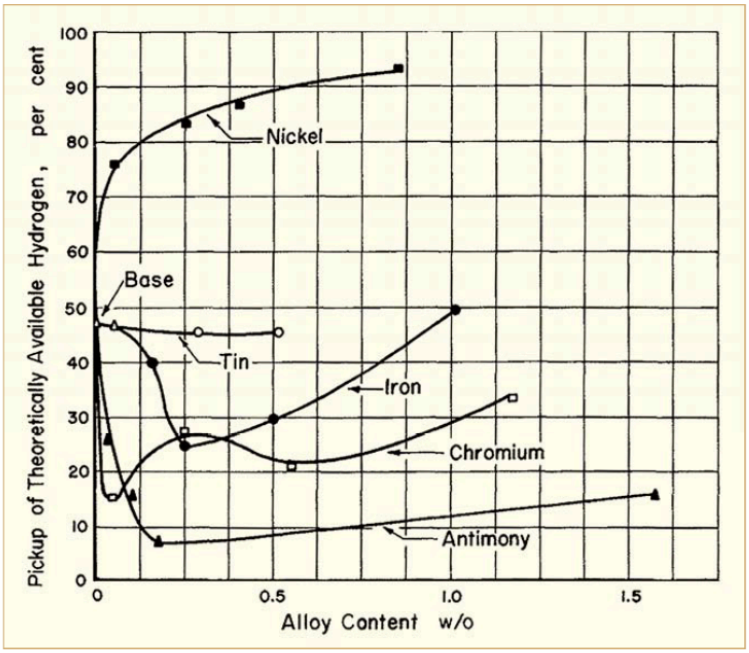

Figure 4.4: Influence of alloying elements on HPUF as measured by Berry[99].

However, a mechanistic understanding of the process, capable of explaining results from the various empirical studies has yet to emerge.

Several phenomenological studies have been dedicated to the relationship between hydrogen pick-up and the transition in oxidation rate. Harada and Wakamatsu report a peak in instantaneous HPUF just before transition, and a sharp decline in the post-transition regime[102]. This is illustrated in Figure 4.5, and the change in HPUF is attributed to increased resistance of the barrier layer. Similar results have been obtained using advanced neutron spectroscopy experiments[103,104].

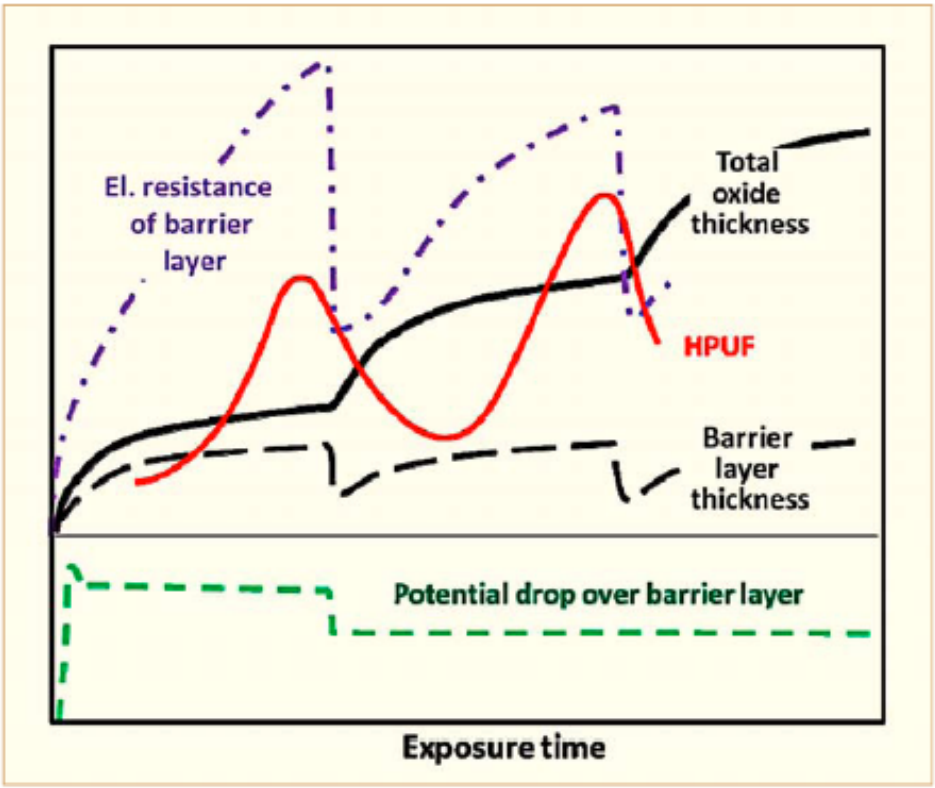

Figure 4.5: Correlation between HPUF, barrier layer thickness, total oxide thickness, electrical resistance of the barrier layer and potential drop over the barrier layer[53].

The conductivity of the barrier layer is identified as a critical factor for hydrogen pickup in many studies[105,106]. A conducting oxide will effectively move the cathode away from the metal, thus decreasing hydrogen ingress. Kakiuchi[107] and Une[101], on the other hand, propose that hydrogen diffusivity through the barrier layer is the rate-determining step for HPUF. The reduction in HPUF in Fe containing alloys is explained by a decrease in proton mobility in the oxide due to Fe atoms in solution. Garzarolli suggests that metallic bands in the oxide grain boundaries exist, caused by segregation of alloying elements[70]. The assumption that this kind of grain boundary segregation exists in the oxide is not verified experimentally, but some speculation follows that this may lead to fast diffusion paths which may act as windows for HPU. Bossis[108] and Hatano[109,110] propose that SPPs in the barrier layer could be short-circuits for hydrogen uptake, and link SPPs in the oxide to the presence of hydrides in the metal underneath.

Another plausible mechanism that has been put forward is that hydrogen traverses the oxide through microcracks and pores[64,85,86,111]. Porosity in the oxide has been observed using a number of different techniques[112–114].

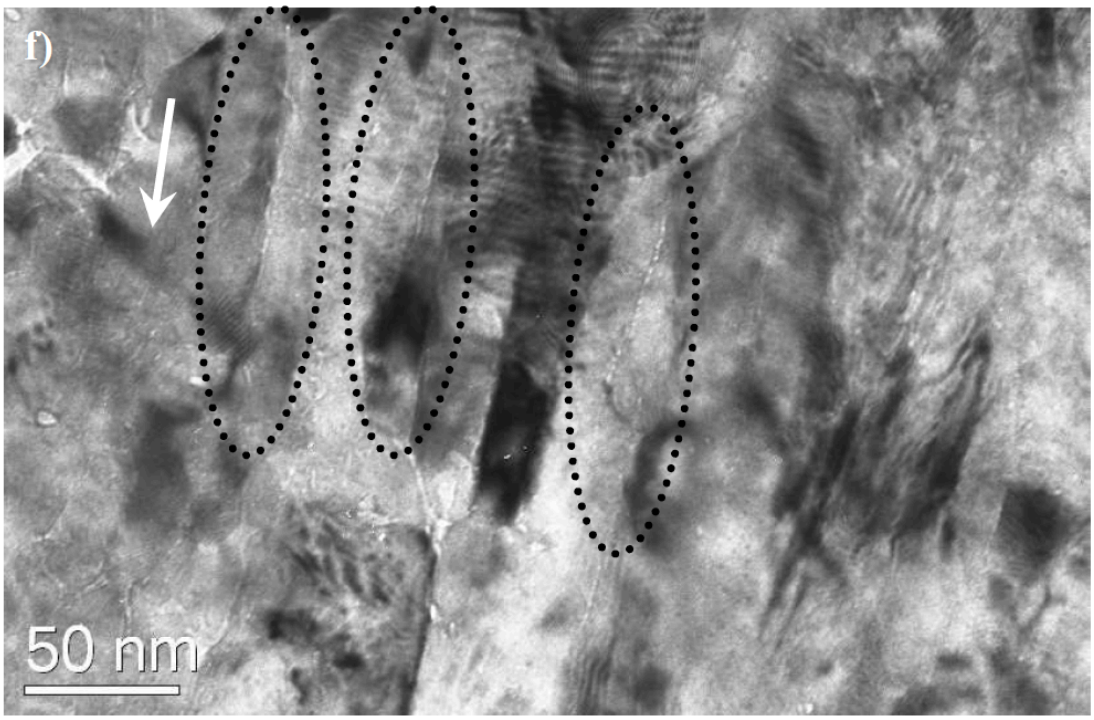

Figure 4.6: Transmission electron microscopy image of interconnected porosities and cracks in the oxide using Fresnel contrast imaging[115]. The oxide growth direction is indicated by the arrow.

Advanced transmission electron microscopy (TEM) studies have later shown that such porosity is often associated with secondary phases and grain boundaries in the barrier layer[115,116] (see Figure 4.6). Networks of these interconnected pores may provide a fast route for hydrogen transport to the metal.

The water chemistry in the reactor will have an influence on the hydrogen pick-up fractions of the cladding. Boric acid, which is used as neutron poison in PWR plants, reduces hydrogen pick-up significantly[117]. LiOH on the other hand, has a severe detrimental impact, which has been shown on many occasions[101,118,119]. From these results it seems apparent that acidic conditions are favorable to a basic pH with respect to the HPUF properties. As discussed earlier, the presence of dissolved H_2 in the reactor water appears to have little influence on the HPUF[53]. Dissolved oxygen on the other hand, has been shown to reduce pick-up[120].

5. Irradiation damage

5.1 Neutron-matter interaction

Although Zr has a low thermal neutron capture cross-section, it is susceptible to elastic interactions with fast (~1MeV) neutrons that are generated by the fission reactions in the fuel. Fast neutrons collide with atoms in the Zr lattice, transferring part of their kinetic energy in the collision[121]. The mean transferred energy to a primary knock-on atom (PKA) $E_{mean,\,PKA}$ can be calculated according to[122]

$$E_{mean,\,PKA} = 2\,E_n\,(m_{Zr}\;m_n)\,(m_{Zr} + m_n)^{-2}$$

where E_n is the kinetic energy of the neutron, m_{Zr} is the Zr atomic mass and m_n is the neutron mass. Taking E_n to be 1 MeV, this yields a kinetic energy of the PKA of 22 keV. If the energy transferred to a lattice atom exceeds a threshold of 40 eV[123], the atom will be knocked out of its lattice position. This will create a vacancy at its former lattice site and a self-interstitial at its new position, collectively referred to as a Frenkel pair. The mean number of lattice points affected by higher order collisions from a PKA can be calculated according to the modified Kinchin-Pease approximation[124]

$$n = 0.8\,E_{PKA}/2\,E_d$$

where n is the number of affected lattice points (i.e. Frenkel pairs), E_{PKA} is the kinetic energy of the PKA and E_d is the displacement energy of a lattice atom. With a PKA energy of 22 keV and a displacement energy of 40 eV, we find that a 1 MeV neutron may on average create 220 Frenkel pairs in a displacement cascade. Although most of these Frenkel pairs will rapidly recombine after the initial neutron-PKA collision, a few point defects will survive in the lattice. Throughout the lifetime of fuel cladding rods, every atom in the lattice will on average be displaced multiple times. The degree of irradiation is usually quantified in terms of the overall average dpa (displacements per atom) of the rod. Specific calculations of the dpa has to be performed for each position in a reactor, but an approximate conversion factor[9] is that 2 dpa corresponds to a fluence of approximately 10^{25} neutrons/m^2.

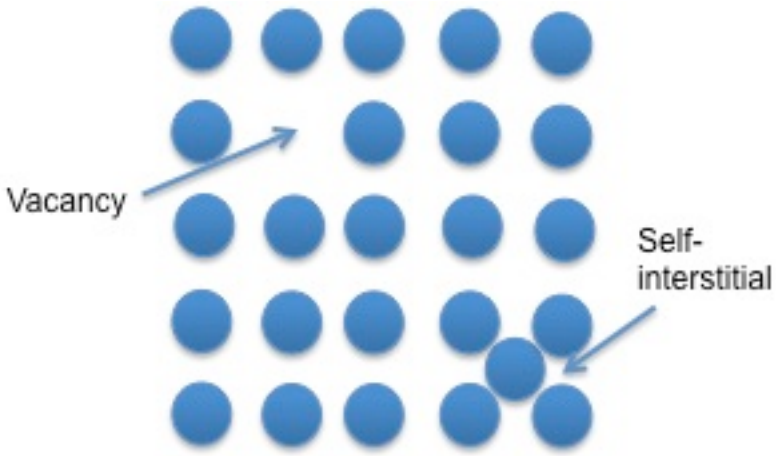

Figure 5.1: Schematic drawing of a Frenkel pair in a 2D cubic lattice.

The hcp structure of α-Zr gives rise to anisotropic diffusion properties in the crystal, whereby self-interstitials preferentially move along the <a>-directions in the basal plane[125]. Some sources also suggest anisotropy for vacancy migration[126]. Diffusion of self-interstitials is significantly faster than vacancy diffusion.

Table 5.1: Formation and migration energies for point defects in α-Zr[123,125–130].

	Vacancy	**Self-interstitial**
Formation energy (eV)	1.4-2.1	2.8-3.5
Migration energy (eV)	0.5-0.9	<a>-directions 0.01-0.06 <c>-directions 0.1-0.3

Defects that are not immediately annihilated can migrate to various sinks, such as grain boundaries and dislocations. In order to minimize their energy, defects may also coalesce to form dislocation loops on prismatic planes in the structure. These dislocations, commonly referred to as <a>-loops, are of vacancy and self-interstitial character in approximately equal proportions. <a>-loops start to form in the early stages of irradiation and very high densities are observed after the first cycles of in-reactor exposure[131]. The loops are typically stacked in layers parallel with basal planes in the structure[132]. Long-term irradiation at high doses will eventually also lead to the formation of loops on the basal planes in the materials - <c>-loops[13,131,133,134]. <c>-loops are exclusively of vacancy character and may grow to radii of several hundred nanometers[135].

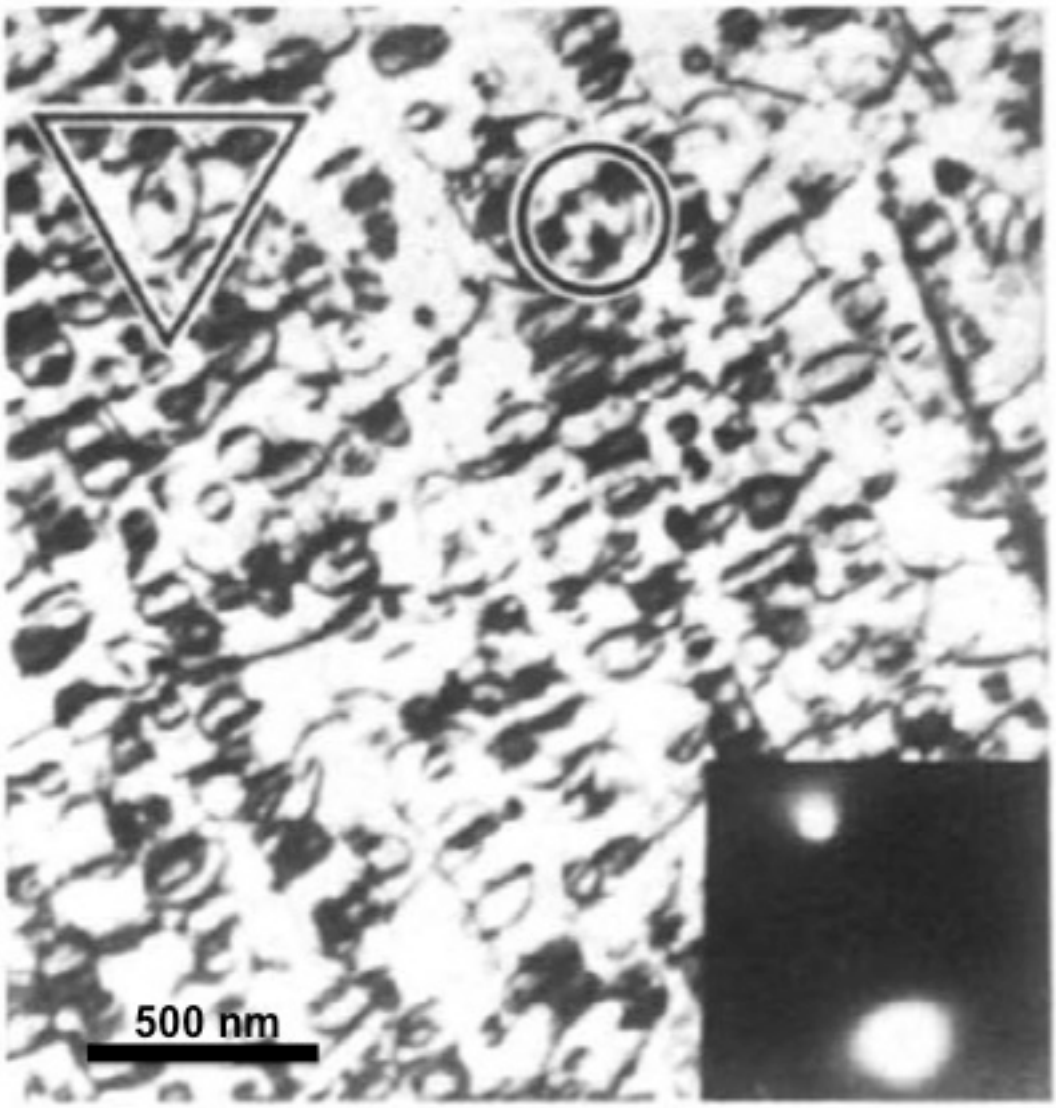

Figure 5.2: <a>-type dislocation loops in neutron irradiated zirconium[132]. The diffracting vector is [-2110].

Another effect of prolonged irradiation of Zirconium alloys is the gradual dissolution of intermetallic precipitates. In the Zircaloys, the first element to leave SPPs has been reported to be Fe[13,136]. Fe depletion is accompanied by amorphization of the $Zr(Fe, Cr)_2$ phase[77]. Reprecipitation of smaller particles throughout the matrix may occur[131], particularly in Nb-containing alloys where β-Nb needles form inside the α-grains[63,137].

5.2 Effect on material properties

The formation of large quantities of dislocation loops throughout the Zr lattice causes significant loss of ductility in the material. Loops are effective obstacles to dislocation movement and have a hardening effect on the macroscopic properties[138]. This may be a concern for instance in relation to pellet-cladding-interaction induced stress-corrosion cracking[13,139] and post-irradiation handling of the fuel assemblies[123].

In the absence of stress, textured Zr alloys undergo dimensional changes at constant volume when subjected to irradiation, referred to as irradiation growth[140–142]. Irradiation growth can have severe implications for the operational safety of the reactor, as it may lead to bowing and elongation of the cladding tubes. Bowing can be an obstacle for inserting the control blades into the core and should be avoided at any cost. Growth is characterized by a contraction of the crystals along the <c>-direction, and an elongation along the <a>-directions. This means that the highly textured fuel cladding rods are very susceptible to growth[143], manifested as macroscopic strain in the axial direction.

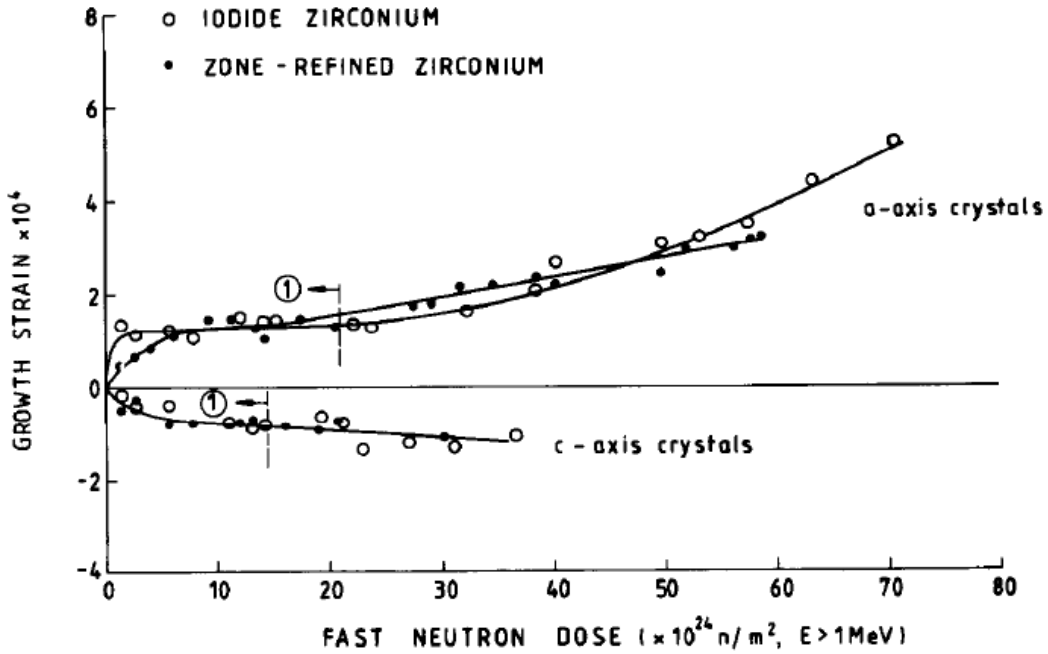

Figure 5.3: Typical growth characteristics of zirconium crystals under prolonged irradiation[144].

Growth is typically relatively fast during the first dpas of irradiation[144]. This stage of growth is associated with the formation of large numbers of <a>-loops. If the <a>-loops are primarily of interstitial character, they will contribute to the fast initial growth[131]. Another possible factor is the bias in diffusion rates between interstitials and vacancies, that may lead to interstitials moving along basal planes to grain boundaries. Growth then slows down, as the number density of <a>-loops saturate. Eventually a breakaway stage of growth occurs, normally associated with the formation of vacancy <c>-loops in the basal plane[145].

The role of the alloying elements in the irradiation growth process has not been unequivocally established. It has been suggested that Fe stabilize embryonic <c>-loops[131], and would therefore have a detrimental impact on the growth properties. The metallurgical difficulty in producing low-Fe Zr crystals makes it difficult to isolate the effects of Fe[146]. High Sn contents have been shown to increase the growth rates of binary alloys, whereas in Zircaloy-2 such detrimental effects are cancelled, suggesting synergistic effects between alloying elements[147].

Creep rates in zirconium alloys are significantly enhanced by neutron irradiation. The pressure difference between the cladding interior and the coolant water may cause a reduction in fuel rod diameter. The influence of microstructure is multi-faceted and complicated, involving e.g. stress states, temperature and grain size[140].

6. Experimental techniques

6.1 Hydrogen analysis

Being the lightest element in the periodic table, its inherent volatility makes hydrogen an extremely difficult proposition for microanalysis. For zirconium alloys, an abundance of different microscopy techniques have been applied over the years to investigate hydriding mechanisms. Traditional optical microscopy allows for imaging of coarse hydrides that may form in bulk zirconium, but its relatively poor resolution prohibits examination of uptake kinetics on an atomic or molecular level. Similarly, X-ray or electron diffraction techniques can yield information about hydride phases, but due to their slight size hydrogen atoms in solid solution do not affect the Zr lattice parameter to any discernable level. Energy dispersive X-ray spectroscopy (EDX) in an electron microscope has good spatial resolution, but is not sensitive to lighter elements in the periodic table and can therefore not be applied for direct hydrogen analysis. Electron energy loss spectroscopy (EELS) is suitable for hydrides[148], but does not suffice for detection of hydrogen in solution. Vibrational spectroscopy, such as Raman and infrared, is indeed sensitive to hydrogen containing molecular complexes, but suffers from poor spatial resolution, making the spectra difficult to interpret. Secondary ion mass spectroscopy (SIMS) is equally sensitive to all elements, and has good spatial resolution (in ideal cases below 50 nm). This is a method that has been applied with some success on zirconium alloys[45,101]. With sub-nanometer scale spatial resolution in combination with complete elemental sensitivity, atom probe tomography is a unique tool for microanalysis on the atomic level. It has successfully been used previously for microstructural examination of zirconium alloys[52,65,149–153].

6.2 Atom probe tomography

6.2.1 Overview

Atom probe tomography is based on ejection of surface atoms from a needle-shaped specimen, by subjecting it to very high electric fields[154]. The electric field, generated by subjecting the specimen to a strong positive DC potential, will, if an additional voltage or laser pulse is superimposed, cause controlled ionization of surface atoms of the tip in a process called field evaporation. Once ionized, a surface atom will be repelled by the tip and accelerated by the field toward a detector.

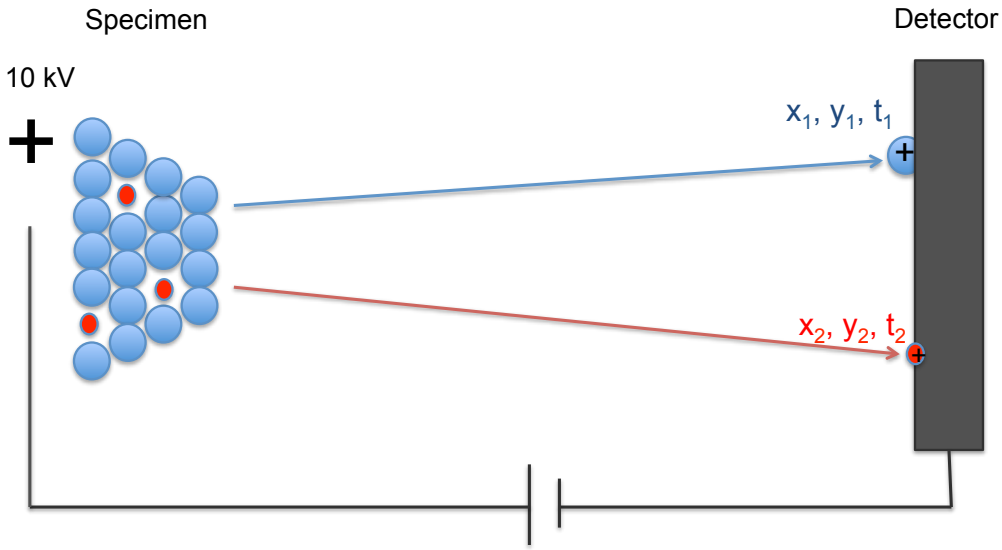

Figure 6.1: Schematic illustration of the APT analysis chamber.

Each ion that hits the detector, whether in atomic or molecular form, is registered and ascribed a time of flight (as measured from the instant of the voltage pulse) and a lateral position where it hits the detector. By assuming that only the atoms in the surface layer of the specimen are field evaporated, it is possible to evaluate their spatial position as well as atomic mass individually. This allows for reconstruction of the three-dimensional atomic configurations in the analyzed specimen[155]. A crude schematic illustration of the experimental setup is presented in Figure 6.1.

6.2.2 Principles of operation

For references to this section, see[156,157].

Atom probe analysis is performed in an ultra-high vacuum chamber (UHV), where the pressure is held as low as possible by a system of pumps. Modern atom probes work at pressures in the 10^{-9} Pa range or below. The samples are cooled to cryogenic temperatures (typically 20-100 K) in order to minimize diffusion of surface atoms, hence improving the resolution of the analysis.

Atom probe specimen must have the shape of very sharp needles, with a tip radius on the order of tens of nanometers. A high positive DC voltage, on the order of kilovolts, is then applied to the specimen to produce a very high electric field around the apex, which is slightly lower than the evaporation field of the material (typically 10-60 GV/m). The needle is mounted at a distance of approximately 40 micrometers away from a circular aperture that is held at a zero potential and serves as a counter-electrode. Clearly, a prerequisite for an electric field to form around the atom probe specimen is that the applied potential can propagate through the needle, i.e. the material has to have at least some electrical conductivity. Another prerequisite is that

the specimen is able to withstand the high mechanical stress (Maxwell stress) that is induced by the high electric field (typically 0.5-18 GPa on the tip surface).

Field evaporation is initiated by superimposing an additional voltage pulse on the specimen (voltage pulsed mode) or by heating the apex of the tip, using a laser beam (laser pulsed mode). These ultrashort voltage pulses (on the order of nanoseconds) will drain surface atoms of their electron density[158] (i.e. negative charge), and cause them to ionize. The process is thermally activated and can therefore be initiated by rapid local heating of the apex by the laser pulse as well[159]. A schematic diagram of the evaporation field dependence on temperature and field strength is presented in Figure 6.2

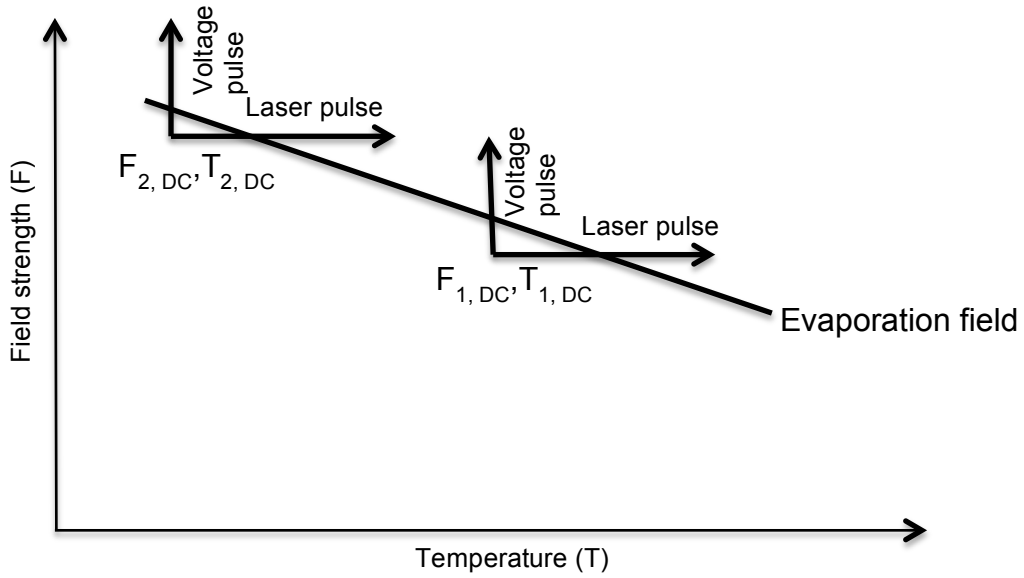

Figure 6.2: Schematic evaporation field dependence on temperature and field strength. Laser pulses are marked as horizontal arrows and voltage pulses as vertical arrows.

In a region close to the surface, atoms may also undergo additional ionization to higher charge states by electron tunneling from the ion into the specimen[160]. This is referred to as post-ionization. The final charge state is determined solely by the magnitude of the electric field in the tip vicinity, and can be used at a later stage in the spectrum evaluation to estimate the field strength during analysis[161].

Once an atom has been field evaporated, thereby ionized, it is accelerated along electric field gradients away from the tip[162]. Equating the potential energy for the ion at the specimen surface with the kinetic energy acquired from acceleration by the electric field yields

$$n\, e\, V_0 = \tfrac{1}{2}\, m\, d^{\,2}\, t^{\,-2}$$

where n is the charge state of the ion, e is the elementary charge, V_0 is the voltage at the tip (for electric pulsing $V_0 = V_{DC} + V_{pulse}$), m is the mass of the ion, d is the distance to the detector and t is the flight time for the ion from specimen to detector.

Rearranging this equation yields

$$m/n = 2\, e\, V_0\, t^{\,2}\, d^{\,-2}$$

Consequently, it is possible to correlate the measurable parameters (V_0 and t) and constants (e and d) on the right-hand side of the equation with a mass-to-charge ratio. This is the fundamental principle for mass spectroscopy, which will be discussed in more detail later on.

The APT instrument used in this study contains an energy-compensating lens – a reflectron[163,164]. The reflectron is used to make corrections for energy deficits of ions that are field evaporated at the later stages of an electric pulse, hence not attaining the full energy $ne(V_{DC}+V_{pulse})$. This is achieved by reducing the flight path length of lower energy ions through the lens, as compared with full energy ions. Thus, the mass resolution of the instrument can be improved significantly in voltage pulsed mode.

When the ions have traversed the vacuum chamber, they are registered at a detector. The detector consists of microchannel plates and an anode. The channel plates are made of materials with high secondary electron yield, so that the ion impact will give rise to a cascade of electrons. The electrons are accelerated toward the anode where they produce a charge pulse. This charge travels in two opposite directions along a delay-line in the detector and the relative pulse delay between the two electrodes (ends of the delay-line) determines where the ion has hit the detector, i.e. its lateral position[155]. By using two perpendicular delay-lines the x-y hit coordinate of the ion is determined. The detector used in this work has a third, redundant delay-line at 45° to the perpendicular ones, to improve the multi-hit capability of the detector.

6.2.3 Experimental factors

Although present day atom probe analysis is largely an automated process, a set of experimental parameters must be selected by the operator of the instrument. These parameters may greatly influence the outcome of the experiment as well as the interpretation of the output data. Brittle materials are unsuitable for voltage pulsing due to the large stress variations that are induced in the specimen by varying electric fields, and should therefore be analyzed in laser-pulsing mode.

Field evaporation of the sample is typically controlled by defining an evaporation rate for the sample. The evaporation rate is the percentage of applied pulses, voltage or laser, which will generate a hit on the detector. Once the operator has specified a rate, the software will adjust the applied voltage so as to maintain an even field evaporation at this rate. Typical values are in range of 0.2-3%. Modern day atom probe instruments allow for very high pulse rates of up to 1 MHz[165], which means that large volumes of data can be obtained very fast.

The temperature at which the experiment is performed will influence the evaporation field of the specimen[166,167], as is apparent from Figure 6.2. A high specimen temperature may induce surface diffusion on the apex of the tip[168], which will

decrease the spatial resolution. This is particularly important during laser pulsing, where instantaneous temperature rises of hundreds of degrees Kelvin may be generated for a few nanoseconds[169]. The charge states of the atoms that hit the detector are also closely related to the laser energy, as the field strength is reduced for higher temperatures. Care therefore has to be taken when selecting laser pulse energy, so that the desired charge states are obtained and spectral overlaps are minimized.

In voltage pulsing mode, the pulse fraction, defined as V_{pulse}/V_{DC}, is another parameter that can be adjusted. If too small pulse fractions are selected, issues with field evaporation between pulses may arise. This will result in decreased detection efficiency, and possibly also loss of data for elements with low evaporation field that are field evaporated at times of DC potential between pulses[170].

6.2.4 Data analysis

A modern day atom probe instrument has the capability to examine dimensions of approximately 100x100 nm laterally, while stretching up to 1 μm along the axis of analysis. Such volumes contain tens or even hundreds of millions of atoms. This gives rise to vast amounts of data that require considerable computing power to process. As described previously, each event on the detector is associated with a mass-to-charge ratio as well as three spatial coordinates. The output data is normally arranged into a mass spectrum, where the number of detector events (counts) for each mass-to charge ratio (Da) is presented. A typical mass spectrum from APT analysis of Zircaloy-2, ranging from 0-35 Da is presented in Figure 6.3

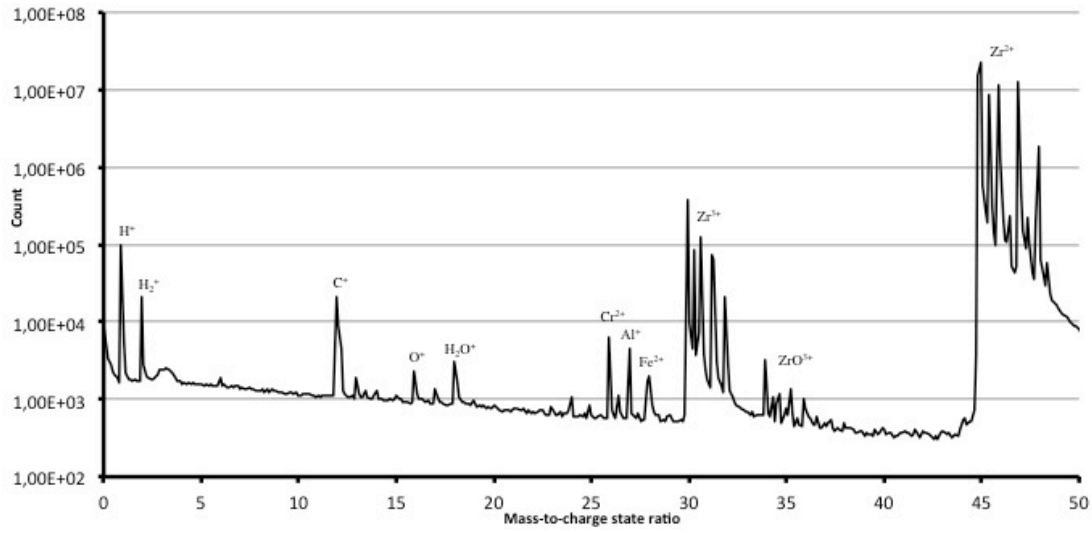

Figure 6.3: Typical mass spectrum from APT analysis of Zircaloy-2, ranging from 0-50 Da. Logarithmic counts scale.

Each element carries a characteristic "fingerprint" in the form of its isotope distribution. Zirconium for instance has five isotopes, where the mass distribution is 51.45% at 89.905 atomic mass units (amu), 11.22% at 90.906 amu, 17.15% at 91.905 amu, 17.38% at 93.906 amu and 2.8% at 95.908 amu. Every element in the periodic table has its own unique isotope distribution, which, in most cases, allows for distinguishing possible overlaps between peaks that may occur in mass spectra.

Once the peaks in the mass spectrum have been evaluated and attributed to the corresponding atomic or molecular species, a 3D reconstruction may be created. This permits detailed examination of the analyzed volumes, where for example information such as concentration gradients, precipitate compositions and grain boundary chemistry can be extracted through the software.

6.2.5 Limitations and artifacts

The main limiting factor for the volumes of data that can be obtained from APT is the tendency of specimen to fracture during analysis. The strong electric fields in the tip vicinity induce high stresses in the material[171], which may lead to rupture of the specimen. This is particularly prevalent for materials with poor conductivity, such as oxides. Therefore, care has to be taken during sample preparation to ensure that the applied potential can propagate to the apex of the tip. Preparation of samples for analysis of the zirconium-zirconia system must be carried out so that the majority of the specimen consists of conducting Zr metal, with only a small scale of insulating ZrO_2 on top. In spite of the insulating nature of oxides, laser-pulsed APT analysis surprisingly works, but has a tendency to give poor mass resolution due to thermal effects[172] and energy deficits arising from potential drops across the oxide top layer[173].

A pervading difficulty in mass spectroscopy is peak overlaps. In Zircaloy-2 a number of such overlaps exist, which must be taken into consideration to ensure accuracy in quantitative compositional analysis[151]. One example is an isotope of the ZrO^{2+} peak at 56 Da in the spectrum, which coincides with minor alloying element Fe^{+}. To overcome this one may take advantage of the field-dependent post-ionization charge state distributions, and bring about a high field strength so that most of Fe ions end up doubly charged at 28 Da.

The atomic detection efficiency in the APT instrument used in this study, which is equipped with a reflectron, is approximately 37%. This means that two-thirds of the field evaporated ions are lost and not accounted for in the data evaluation. Normally this is not a cause for great concern, as losses occur indiscriminately across the periodic table. In some cases however, certain ions evade detection and lead to erroneous compositions. Examples of this are some carbides and oxides[174–176].

6.3 Sample preparation

6.3.1 Electropolishing

The traditional way of preparing samples for APT is an electrochemical polishing technique[177]. It is a comparatively quick and simple method that permits multiple samples to be fabricated conveniently. In a first step a rod of approximate dimensions 0.2x0.2x20 mm is produced from the material of interest. This can be done through

various cutting or machining processes. The rod is then fastened in a sample holder and mounted in an electrochemical cell as illustrated in Figure 6.4.

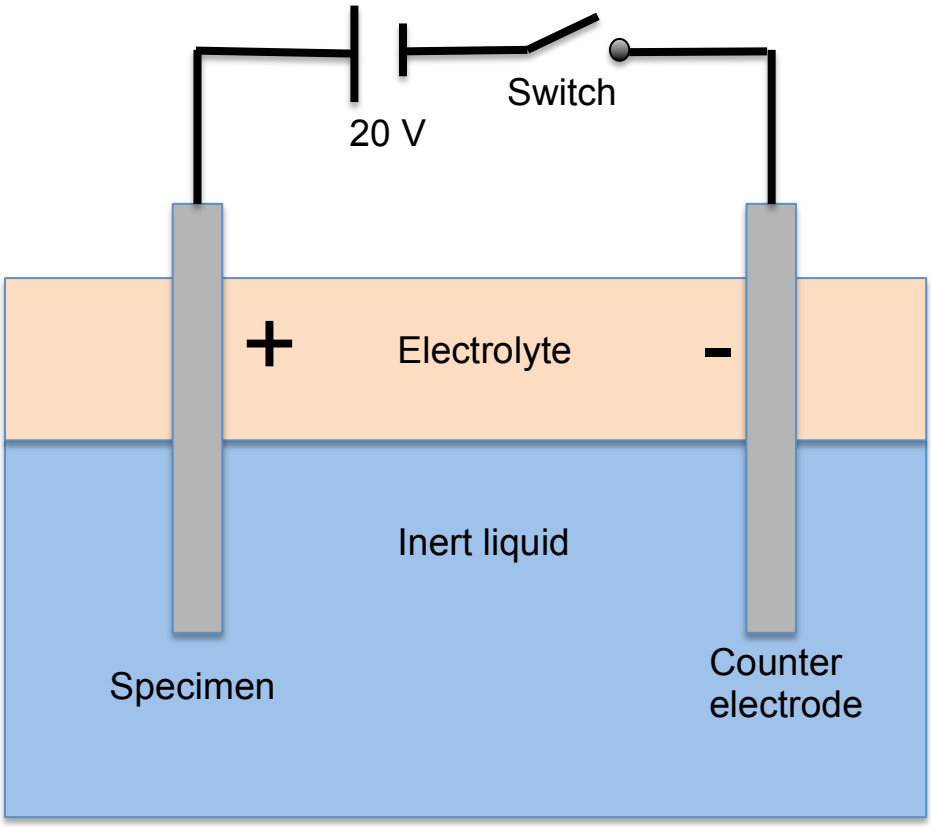

Figure 6.4: Schematics of the electrochemical cell setup during electropolishing.

A positive voltage is then applied to the specimen, where electropolishing will take place on the surface of the part of the material that is immersed in electrolyte. The electropolishing is maintained until a neck is formed on the sample. At this point, the initial electrolyte is replaced with a more dilute solution. A second electropolishing step is performed until the two ends of the rod separate and two needles are formed. This sample preparation technique is ideally suited to analysis of the bulk of materials. However if specific regions are of interest, such as precipitates, grain boundaries or phase interfaces, the electropolishing method may be inadequate as there is no way of asserting that such volumes will be included in the analysis. Electropolishing must then be complemented with correlative TEM imaging of the tip, to ensure that the regions of interest are captured in the APT analysis[178].

6.3.2 FIB-SEM lift-out technique

The combined scanning electron microscope and focused ion beam (FIB-SEM) has opened up new possibilities in sample preparation for microanalysis, both for APT and transmission electron microscopy[179–182]. Scanning electron microscopes (SEM) use an electron beam that is focused through a system of electrostatic and magnetic lenses onto a specimen. Various signals are created and can be used to analyze the sample, such as X-rays (chemical composition), backscattered electrons (atomic

number contrast) and secondary electrons (topographical contrast). The focused ion beam (FIB) has a similar working principle, but the beam instead consists of ions, typically from a liquid metal source. Due to the significantly higher mass of the ions, the FIB can be used for sputtering of material in the sample. The FIB is also equipped with a micromanipulator needle, to which samples can be attached by deposition of platinum.

The lift-out procedure starts by deposition of a protective layer of Pt over the region of interest. Ion sputtering is then used to produce trenches at an angle of approximately 30° from the surface normal, on either side of the Pt strip. The needle is inserted into the chamber and the sample is attached onto it by Pt deposition.

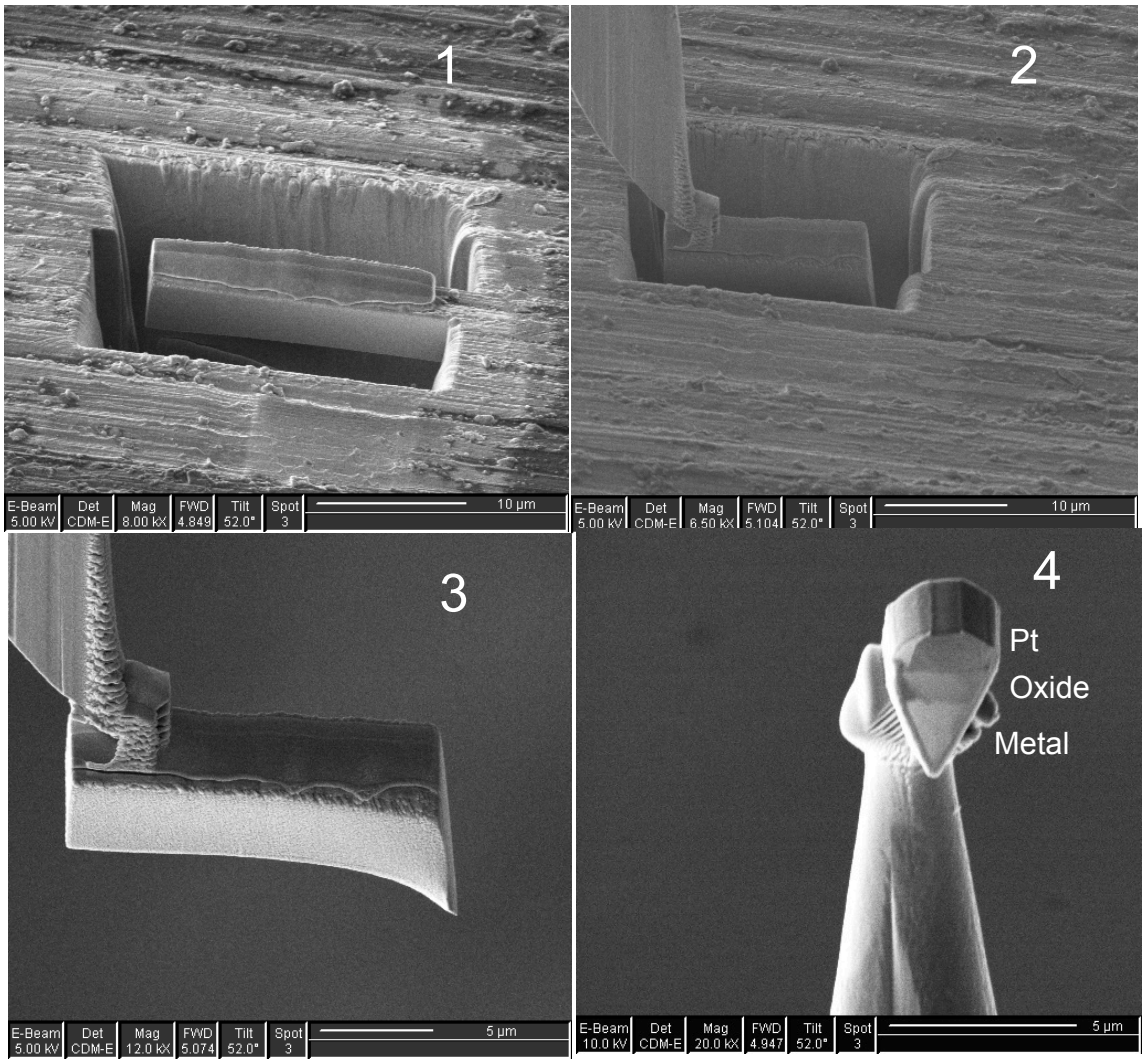

Figure 6.5: Lift-out sample preparation technique in FIB-SEM. A wedge-shaped sample is attached to a micro-manipulator needle. Slices of the wedge are then mounted on pre-fabricated Si posts**.**

Slices of the wedge-shaped specimen are subsequently attached to pre-fabricated Si posts on a wafer. The posts are conical, with the end truncated to a radius of approximately 1 µm. The lift-out procedure is depicted in Figure 6.5.

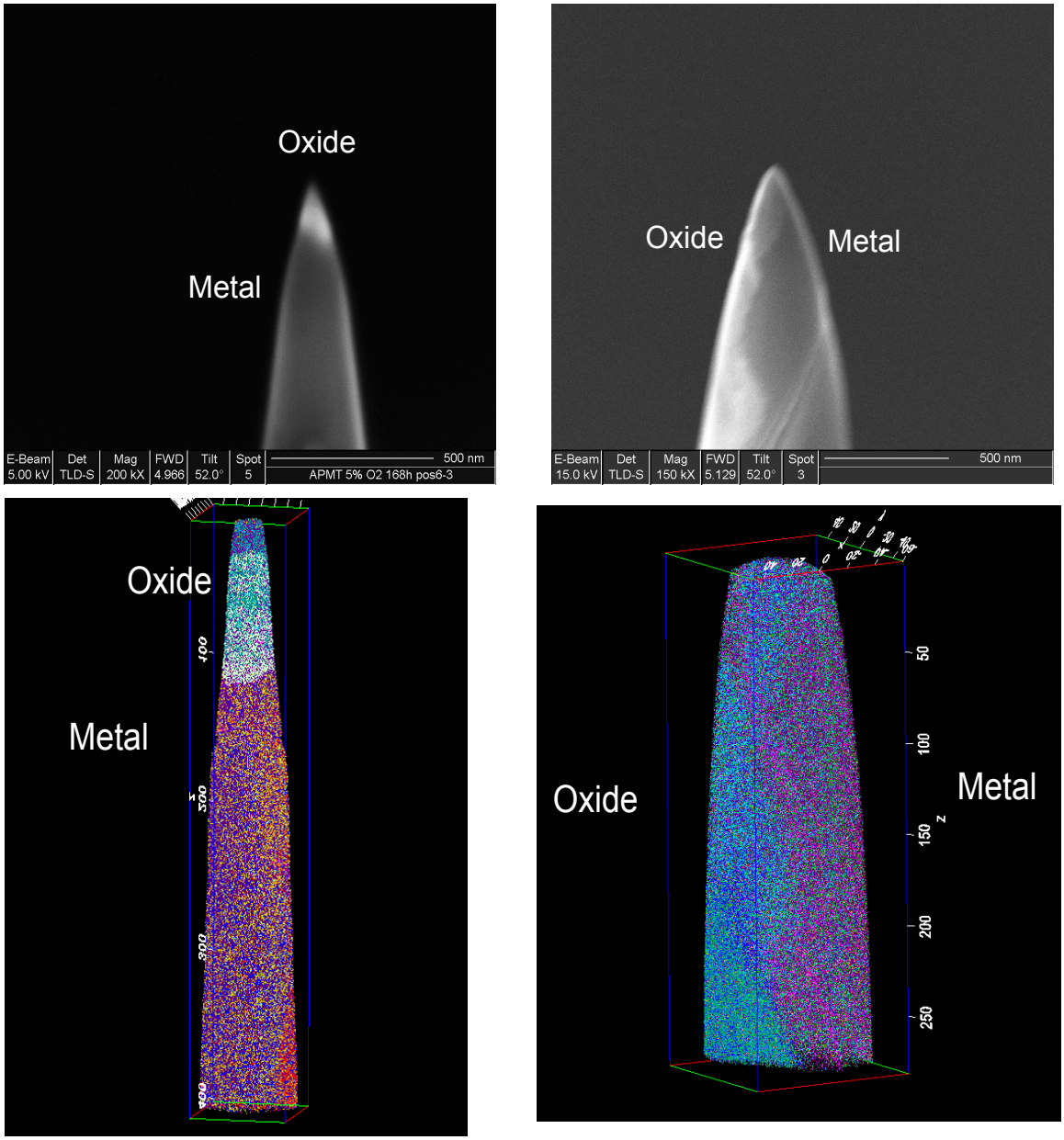

Figure 6.6: Final shape of specimen before APT analysis (above), and APT reconstructions of the same specimen (below).

Once the specimen is fixed to the post with Pt deposition, annular ion milling is performed to create a sharp needle shape where the apex is placed in the region of interest. Figure 6.6 shows two final tip shapes and the corresponding APT reconstructions.

7. Studied materials

7.1 Paper I

For the experiments in the first paper, which is focused chiefly on method development for hydrogen analysis in APT, a material was needed that may readily withstand extensive analysis without significant risk of early fracturing. This puts the following requirements on the specimen material:

- Good electrical and thermal conductivity
- Reasonably high strength and ductility
- Reproducible and straight-forward APT needle preparation

For these reasons an alloy containing 80% Ni, 20% Cr and small amounts of Si was selected. The name of the alloy is Nikrothal 80, manufactured by Kanthal (now Sandvik Heating Technology). Nickel based alloys have been analyzed since the early days of the atom probe technique[183–185] and are known to be highly suitable for APT analysis. APT needles can readily be prepared through electropolishing of Nikrothal wires. In addition, Ni based alloys are relatively insensitive to atmospheric corrosion, which prevents the formation of an insulating oxide film at the needle surface during sample preparation and pre-experiment handling.

7.2 Papers II-IX

The materials that have been analyzed in the zirconium related papers are predominantly commercial alloys that are in wide use in industry today. The main focus of this study has been to understand degradation of Zircaloy-2, an alloy that is used as fuel cladding in BWR plants, but also for various structural parts in other reactor designs. Complementary microanalysis has also been performed on other zirconium-based materials, such as the common PWR material ZIRLO™ and a binary Zr-2.5Nb alloy, widely used in Canadian CANDU reactors.

7.2.1 Zircaloy-2

The investigated Zircaloy-2 materials in this study are primarily tubes of the Westinghouse designated LK2 and LK3 heat treatment schemes. LK2 and its modern counterpart LK3 have been in use in BWRs for decades and extensive data on their corrosion behavior exists, both from autoclave tests and in-reactor[19,29,38,70,186–188]. The two alloys have slight differences in chemical composition, as presented in Table 7.1.

Table 7.1: Chemical composition of the commercial Zircaloy-2 materials in this study. Data supplied by manufacturer Sandvik Materials Technology.

Alloy	***Composition (wt%)***				
	Sn	***Fe***	***Cr***	***Ni***	***O***
LK2	1.46	0.12	0.10	0.05	0.12
LK3	1.32	0.17	0.10	0.05	0.13

The cumulative heat treatment parameter of Zircaloy-2 is described by a normalized annealing parameter *A*, given by

$$A = \Sigma\, t_i \exp(-Q/RT_i)$$

where *i* corresponds to the *i*th heat treatment after the final β-quenching of the material at the temperature T_i during the time t_i, R is the gas constant, and Q is the activation energy for diffusion (264 kJ/mol) . The heat treatment will have an impact on the average SPP size of the material, and differs between LK2 and LK3. It will also produce a fully recrystallized microstructure. The modifications in chemistry and heat treatment also give rise to differences in hardness and strength. A summary of the heat treatments is given in Table 7.2.

Table 7.2: Heat treatment parameter, average SPP size and yield stress for the commercial Zircaloy-2 materials in this study. Data supplied by manufacturer Sandvik Materials Technology and Ref[189].

Alloy	***log A***	***Average SPP diameter (nm)***	***Yield stress (MPa)***
LK2	-16.0	22	215
LK3	-13.9	84	180

The materials were corrosion-tested in steam in static autoclaves for various times, in order to simulate BWR conditions. The pressure in the autoclaves were 10.3 MPa and temperatures of 400°C and 415°C were used for the 1-2 μm and 9 μm oxide thickness samples, respectively. Oxidation data for the analyzed materials is presented in Table 7.3.

Table 7.3: Autoclave data and corresponding oxide thicknesses for the analyzed commercial Zircaloy-2 materials in this study. Data provided by manufacturer Sandvik Materials Technology.

Alloy	*Temperature (°C)*	*Time (days)*	*Oxide thickness (µm)*
LK2	400	3	1.3
	400	6	2.3
	415	30	8.8
LK3	400	3	1
	400	15	1.8
	415	60	9

Autoclave corrosion and hydrogen pick-up data for LK3 oxidized in 360°C water at saturation pressure is presented in Figure 7.1 (courtesy of Westinghouse Electric Company LLC). The in-reactor corrosion behavior of LK2 and LK3 is presented in Figure 7.2.

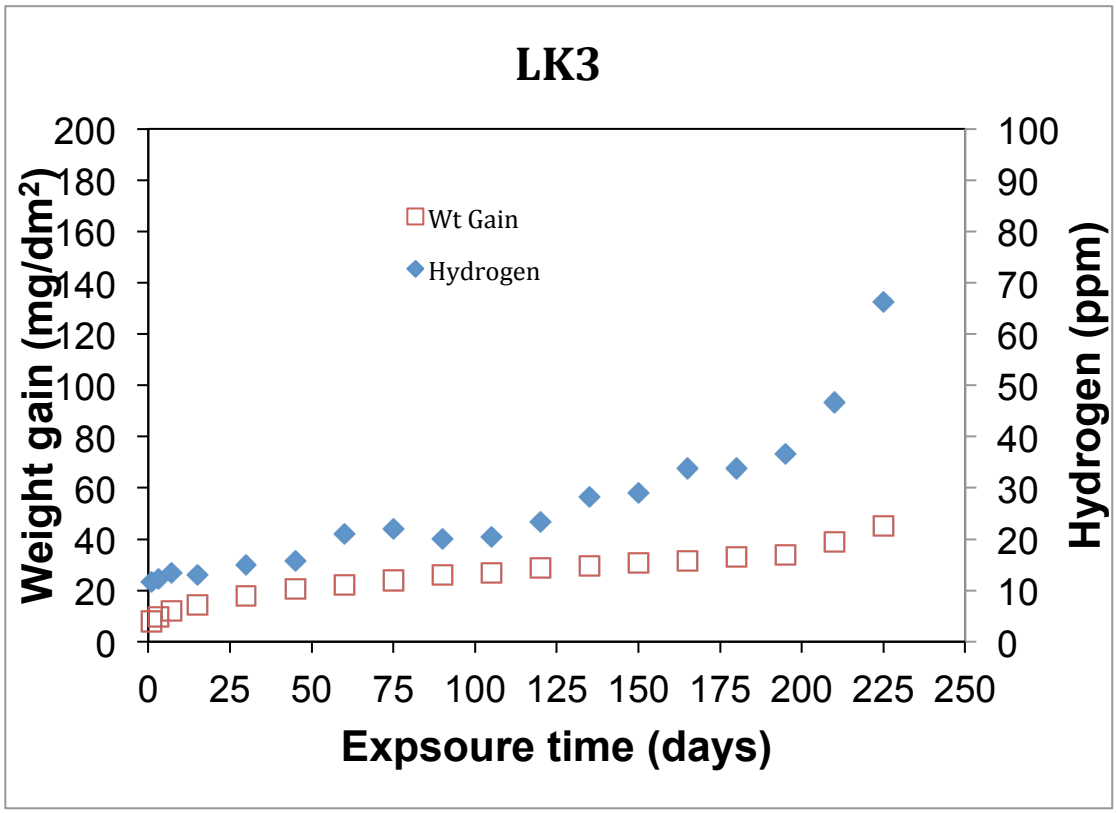

Figure 7.1: Oxidation and hydrogen pick-up data for Zircaloy-2 of the LK3 heat treatment scheme, autoclave-corroded in 360 °C water at saturation pressure. Courtesy of Westinghouse Electric Company LLC[190].

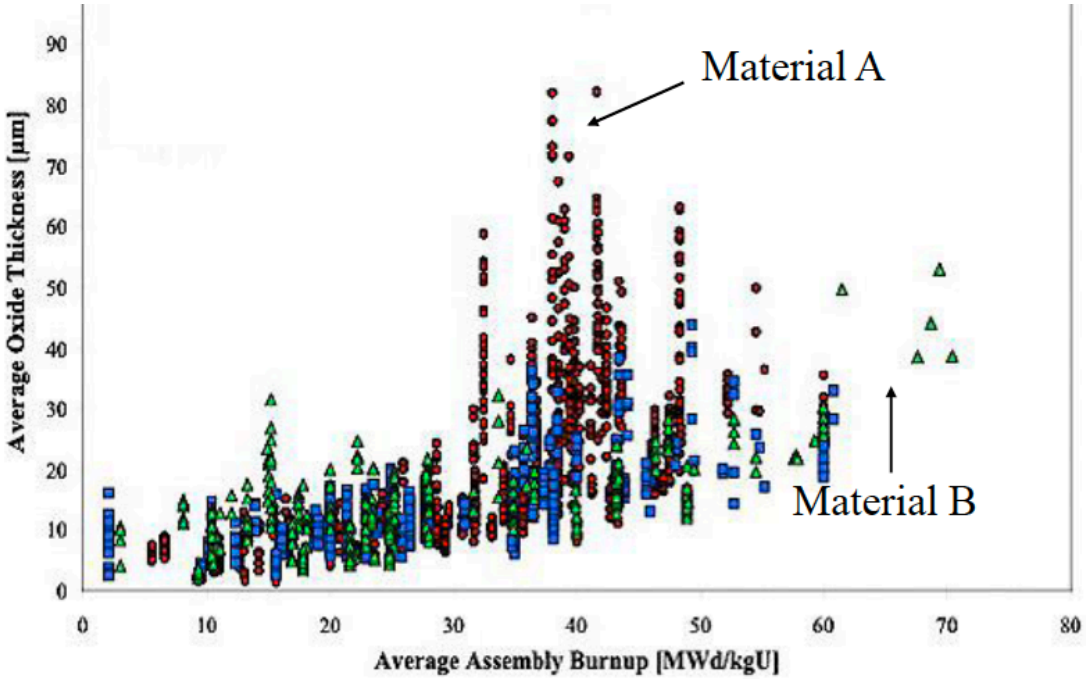

Figure 7.2: In-reactor corrosion behavior of the LK2 and LK3 alloys[188]. LK2 is referred to as 'Material A' (circles) and LK3 as 'Material B' (triangles) in the figure.

The microstructure of the bulk metal in LK3 after in-reactor exposure has also been extensively analyzed with TEM previously[186] (see Figure 7.3). This provides valuable reference for comparisons with the APT results in this thesis.

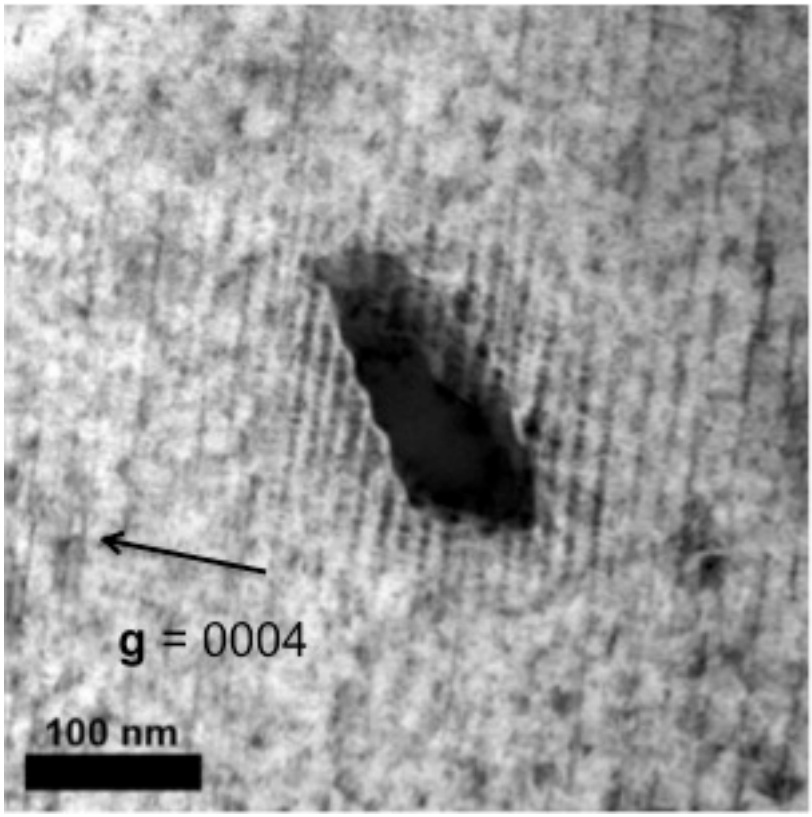

Figure 7.3: TEM micrograph of a partially dissolved $Zr(Fe, Cr)_2$ particle after 3 cycles of in-reactor exposure (approximately equivalent to 15 dpa)[186].

A β-quenched Zircaloy-2 material with a series of custom heat treatments is investigated in ***Paper VIII***. A detailed description of the annealing times, temperatures and cooling rates is given in ref[40].

7.2.2 Zr-2.5Nb

A Zr-2.5Nb pressure tube material used in CANDU reactors has also been studied in this thesis (***Paper VI and VII***). Like the Zircaloy-2 cladding, the autoclave and in-reactor performance of this alloy has also been extensively studied in previous works[63,116,191,192]. Apart from the addition of 2.5% Nb (by weight), the alloy also contains 1140 wt ppm of Fe. After a water-quenching step from the β-phase, the material was extruded and cold-worked to produce tubes of 112 mm outside diameter. The tubes were then stress-relieved in steam at 400°C for 24 hours. This gives rise to a microstructure of elongated α-grains, surrounded by a network of β-filaments. The β-phase is metastable and contains most of the added Nb. A TEM micrograph of the microstructure around the metal-oxide interface is shown in Figure 7.4.

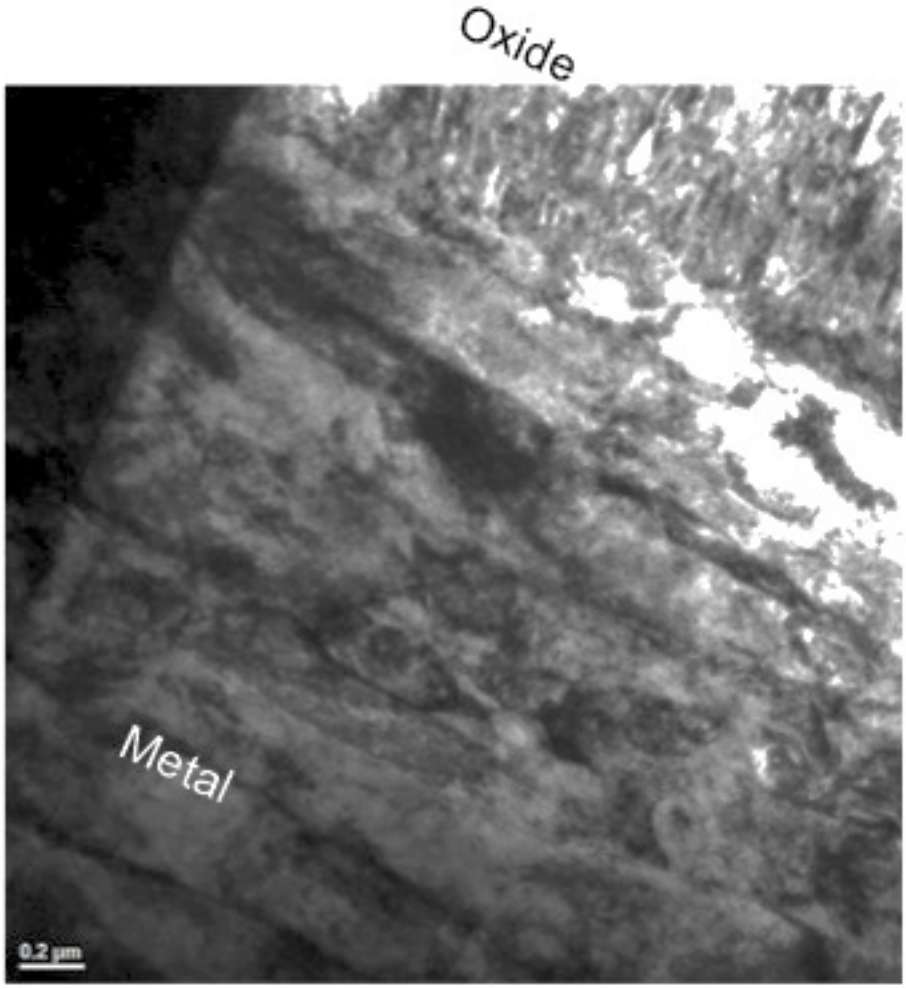

Figure 7.4: Bright-field TEM micrograph of the metal-oxide interface region of the analyzed Zr-2.5Nb material.

The material was corroded in a heavy water autoclave operated at 335 °C. LiOH was added to the autoclave solution, raising the pH to 10.5. The mass gain and deuterium pick-up properties are presented in Figure 7.5.

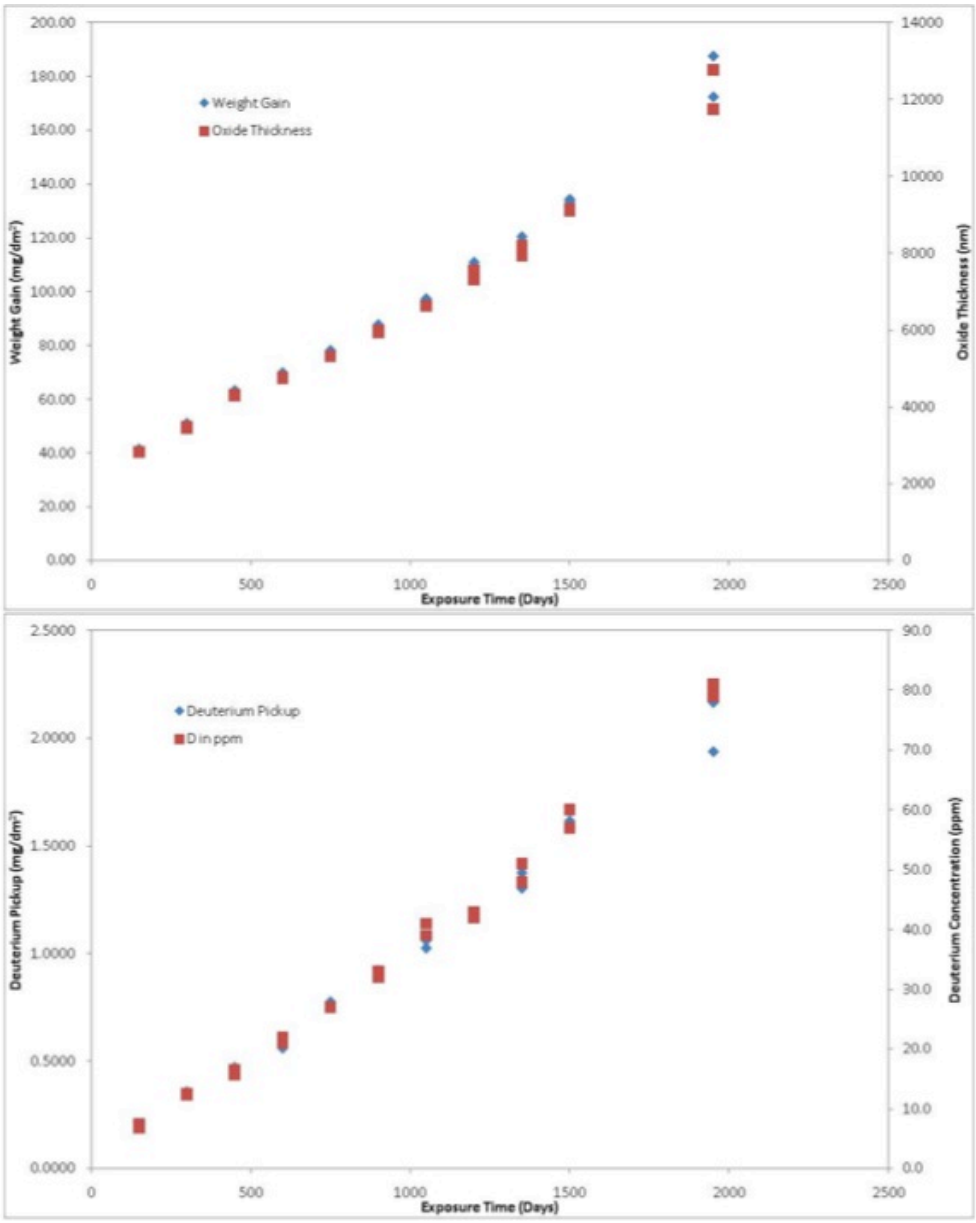

Figure 7.4: Corrosion kinetics and deuterium pick-up for the analyzed Zr-2.5Nb pressure tube material. Courtesy of Atomic Energy of Canada Limited.

8. Summary of results and discussion

8.1 Outline of the papers

This work was performed as a part of the MUZIC-2 program (Mechanistic Understanding of Hydrogen Pickup in Zirconium), which is a joint project involving industry and universities aimed at gaining knowledge of the process of hydrogen pick-up in zirconium alloys. Only very limited work has been performed to study hydrogen with APT previously, thus some groundwork in terms of method development was necessary. ***Paper I*** is concerned with the adsorption mechanisms for hydrogen-containing gases in the APT vacuum chamber. This is of importance for the quantification of hydrogen content in materials, as adsorbed species will field evaporate along with the material itself and give rise to erroneously high hydrogen signal. ***In Papers II, III and IV*** the oxide and the metal-oxide interface region of a commercial Zircaloy-2 oxidized in steam is examined, and the distribution of alloying elements around the interface is mapped. ***Paper V*** is more theoretical in nature, and the findings from ***Papers II-IV*** are put in to the context of general electrochemical mechanisms behind hydrogen pick-up, outlined from atomistic modeling by Mikaela Lindgren and Itai Panas. One of the key ideas of the proposed mechanism in ***Paper V*** is the migration of hydrogen through hydroxylated oxide grain boundaries. In ***Paper VI*** this hypothesis is experimentally confirmed, using the experience gained from from ***Paper I*** and exposing samples to heavy water autoclaves. ***Paper VII*** aims to tie all the prior observations together in the framework of a general mechanism for hydrogen pick-up. In ***Papers VIII and IX*** the focus was shifted primarily to characterize the bulk metal before and after irradiation, so as to highlight the effects of alloying elements on irradiation damage.

8.2 Summary of the thesis work

8.2.1 Hydrogen measurement

As the available literature on the behavior of hydrogen in APT is scarce, the initial focus of this work was to investigate the feasibility of hydrogen analysis, and to what extent experimental parameters can be optimized for minimal adsorption of gaseous H_2 from the vacuum chamber. By carefully examining the influence of factors like temperature, electric field and tip geometry, it was concluded that it is not possible to eliminate adsorption entirely during analysis. However, choosing the right set of parameters enables control over which hydrogen-containing species that will appear in the mass spectra. The physical mechanisms behind this process are as follows (see ***Paper I***):

- H_2 molecules in the vacuum chamber are polarized by the electric field and attracted to the surface through a dipole-dipole interaction.
- H_2 resides on the surface in molecular form in a field-adsorbed state.
- H_2 is desorbed from the surface by a conventional field evaporation process, whereby it is ionized to H_2^+ or dissociated to two protons at higher field strengths.

A schematic of this process is presented in Figure 8.1. At very high field strengths (applicable during voltage pulsing), gas molecules may undergo field ionization before adsorption is possible. This may lead to reduced quantities of hydrogen in the mass spectra. Under normal APT analysis conditions in laser pulsing mode, hydrogen is detected in both atomic and molecular form. The quantity of adsorbed hydrogen species typically range between 0.05 - 1.5% of the total ion count in the spectra.

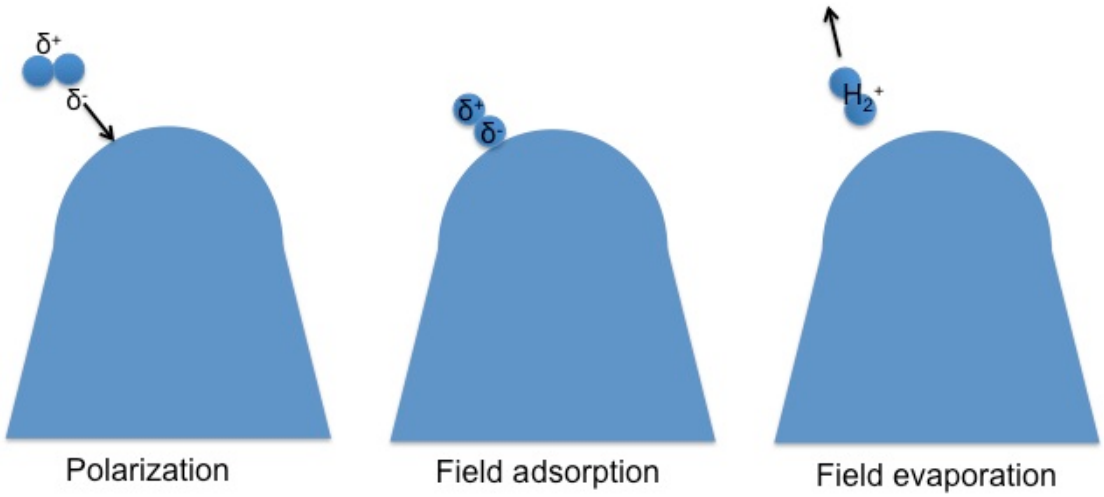

Figure 8.1: Schematics of the dominating H_2 adsorption-desorption mechanisms on the APT tip during normal analysis conditions.

Although one can draw some comfort from the fact that it is possible to suppress the supply of hydrogen to the tip during APT analysis, the conclusion of these early experiments is that it is necessary to compare H_2O-corroded samples with materials

corroded solely in D_2O if the assumed small amounts of hydrogen that is present in the oxide scales are to be unambiguously identified.

8.2.2 First analyses of zirconium

The next step was to start to examine Zircaloy-2 samples. Zr alloys are notoriously prone to fracture during APT analysis[193,194], so it was essential to develop a reliable procedure for tip preparation using FIB-SEM. After some initial testing it became apparent that analyses from bulk of the oxide tended to give only very limited volumes of data with poor data quality. However, by fabricating tips that contained only a small cap of oxide on top of metal the yields could be increased significantly. Unlike the bulk oxide, the regions around the metal-oxide interface proved highly suitable for APT analysis.

A surprising and striking observation from the first APT analyses of the metal-oxide interface region was the presence of large amounts of Fe and Ni (but not Cr) segregation to grain boundaries and dislocation networks in the oxygen-saturated region of the outermost metal grains (see Figure 8.2).

The abundance of grain boundaries was unexpected, as the small volume of an APT analysis renders it improbable to capture a grain boundary in a material with a grain size of approximately 5-10 μm. Taking into account the high number of dislocation-like features in the metal near the interface, the only reasonable explanation for these observations is that they were not in fact original high angle boundaries, but sub-grain boundaries formed by creep deformation of the metal. The phase transformation from Zr to ZrO_2 is associated with a volume expansion of 55%. As the oxide grows inwards, there is no free surface to accommodate this expansion, and the metal substrate must therefore start to yield. Due to the extremely low solubility of Fe and Ni in the matrix, the new defects will quickly attract segregating species (see ***Paper II***).

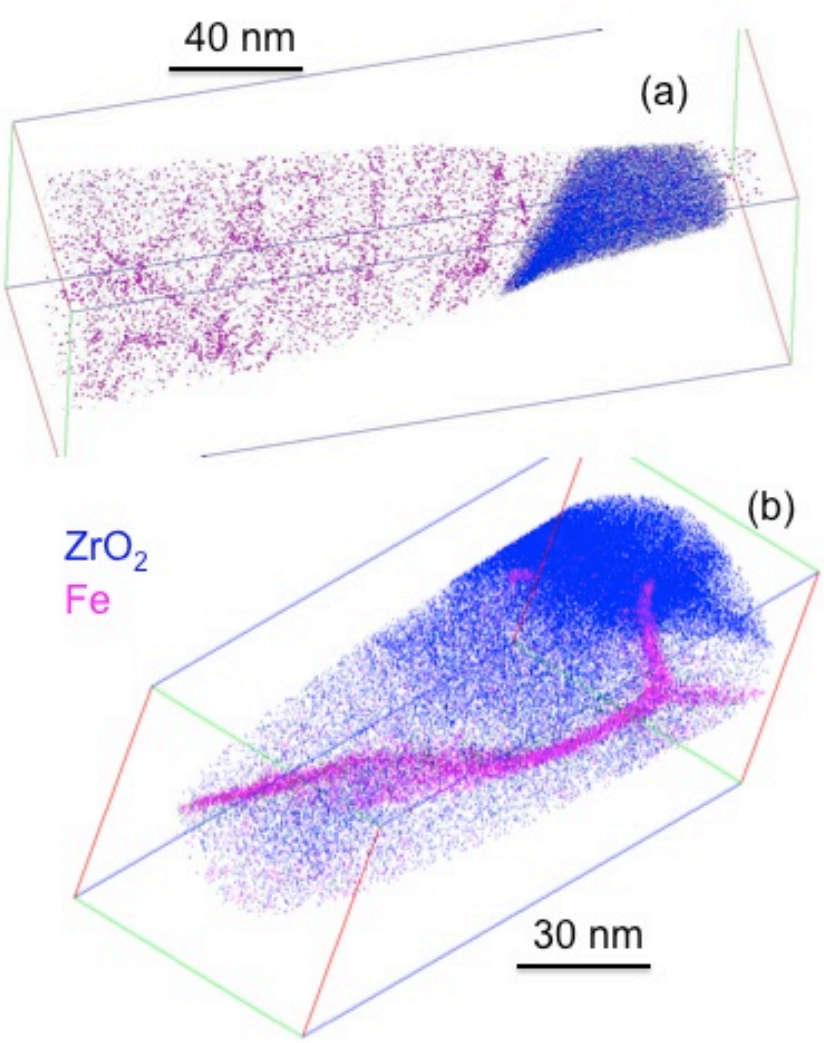

Figure 8.2: Segregation of Fe to dislocations (a) and grain boundaries (b) around the metal-oxide interface in Zircaloy-2 corroded to a 1 μm oxide thickness.

Interestingly, the planar segregation of Fe and Ni – not Cr – to sub-grain boundaries was observed to continue uninterrupted into the advancing oxide, across the oxide front. Consequently, the oxide appears to inherit the grain boundary chemistry of the creep-deformed outer grains as the metal is consumed (see figure 8.3). Very little Fe, Ni and Cr were found to reside in solution in the alloy.

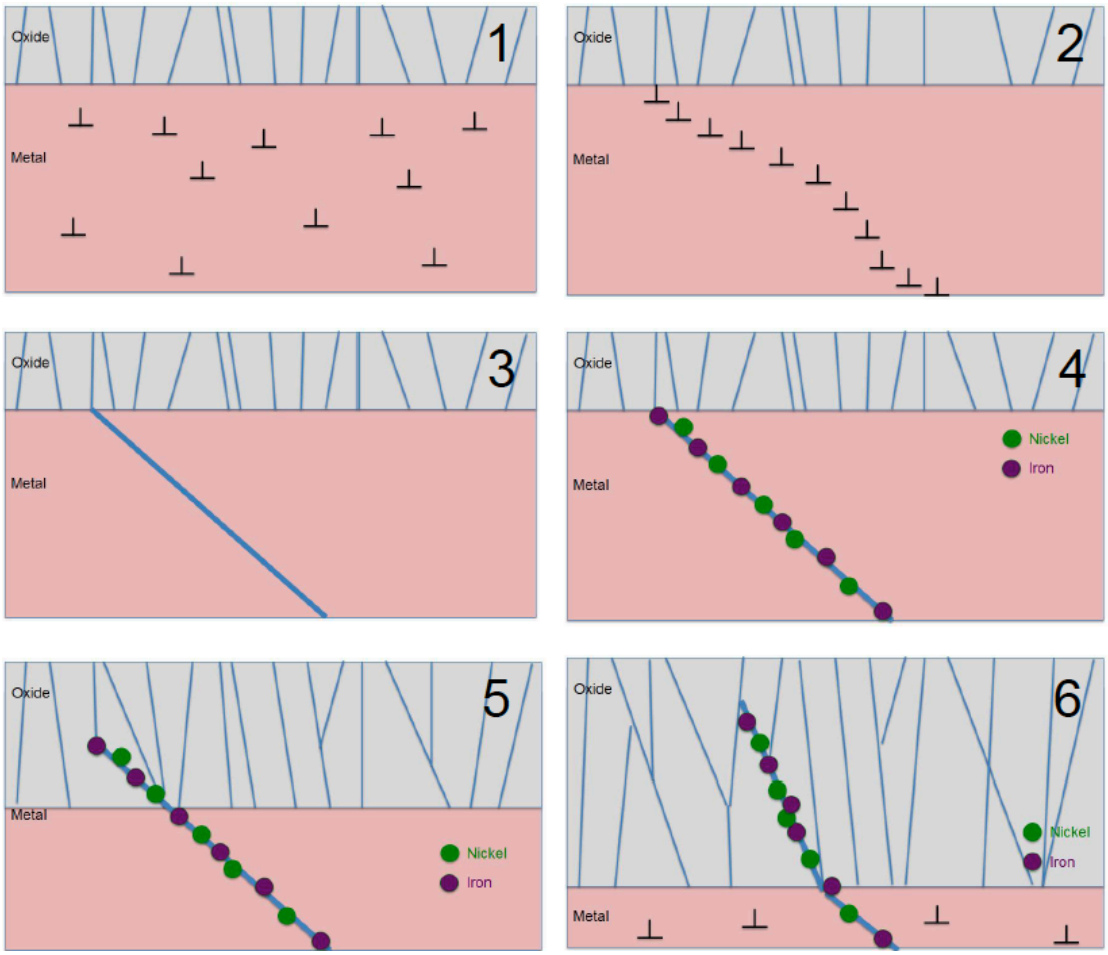

Figure 8.3: Schematics of the deformation induced by the oxide growth and subsequent segregation of Fe and Ni to newly formed sub-grain boundaries.

It is important to note that this segregation does not apply to all grain boundaries in the oxide. The oxide grain size is extremely small, so most boundaries will not be decorated with Fe and Ni.

A large number of SPPs of both the $Zr_2(Fe, Ni)$ and the $Zr(Fe, Cr)_2$ families were analyzed in the metal-oxide interface region. Upon examination, theses particles proved not to contain any elevated concentrations of hydrogen and the hypothesis of SPPs being hydrogen sinks[108–110] could be discarded.

Mapping of the oxygen distribution around the metal-oxide interface revealed a highly irregular and complicated sub-oxide structure (see ***Paper III***). The suboxide has a composition of Zr_xO_{1-x} where x ranges between 0.45-0.55. From the materials investigated in this study, there is nothing to suggest that the thickness of the suboxide would by coupled to the transition. Instead, it appears to increase monotonously in thickness with the total oxide thickness.

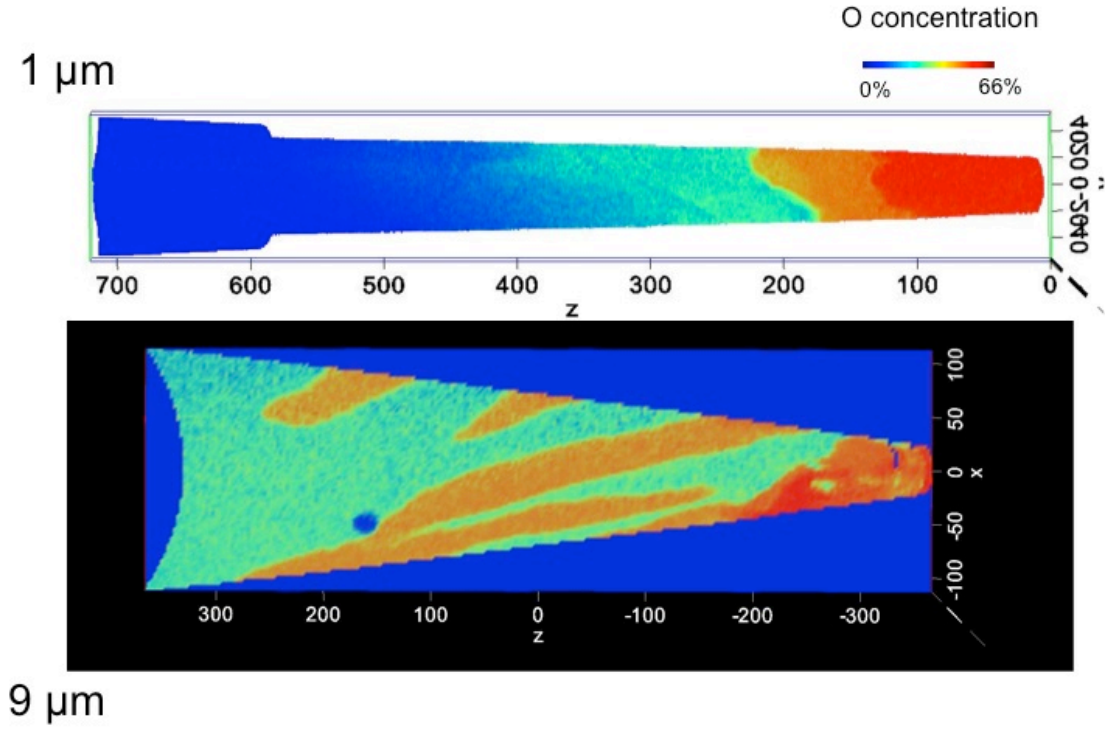

Figure 8.4: Suboxide distribution (orange) from Zircaloy-2 corroded to 1 and 9 µm oxide thicknesses. The blue dot in the 9 µm oxide analysis corresponds to a $Zr(Fe, Cr)_2$ type SPP.

The suboxide layer is typically followed by an oxygen saturated metal zone (~30 at% oxygen) and a subsequent oxygen diffusion profile into the metal Underneath the diffusion zone, large accumulations of hydrogen were often observed. Based on the observations in ***Paper I***, we could now with some confidence ascribe these features to hydrides resulting form the corrosion process. A heat map of hydrogen and oxygen distributions around the metal-oxide interface in a pre-transition Zircaloy-2 is presented in Figure 8.5.

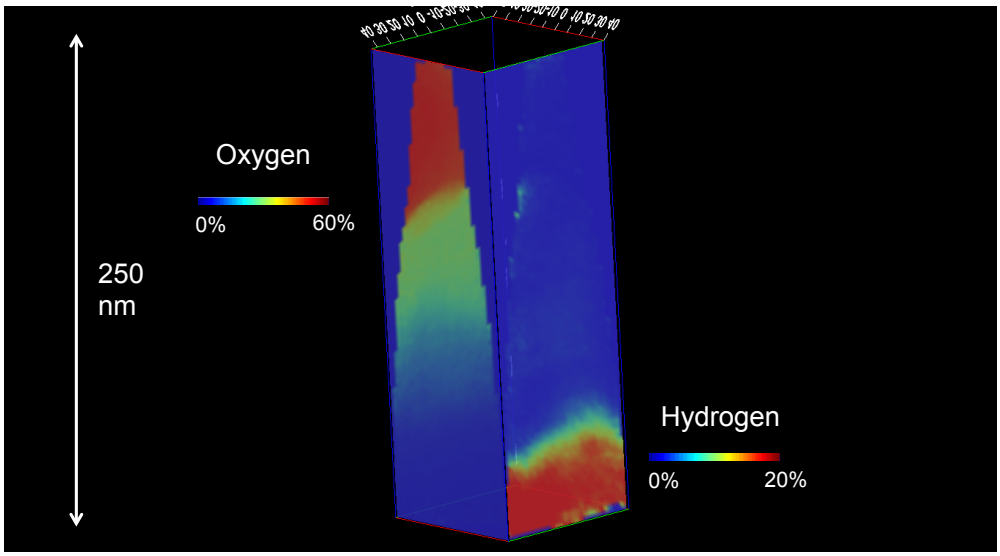

Figure 8.5: Oxygen and hydrogen heat maps from APT analysis of the metal-oxide interface region in 1 µm oxide Zircaloy-2.

From a hydrogen pick-up perspective, the most pertinent observation from these initial analyses of the metal-oxide interface was the presence of Fe and Ni in oxide grain boundaries. Small additions of Fe and Ni in zirconium are well known to have an enormous impact on corrosion and hydrogen pick-up properties, and it is therefore of essence to establish their distributions in the protective oxide scale. Aliovalent transition metals in grain boundaries of the otherwise strongly insulating oxide are likely to act as local dopants, and may provide local transport paths for electronic current. This was substantiated by the band structure calculations performed by Lindgren and Panas in ***Paper V***. A channel for electron transport may serve to move the cathodic reaction away from the metal, thus reducing hydrogen pick-up. Moreover, Lindgren's and Panas' calculations also suggested that proton reduction would be suppressed in Ni-infused grain boundaries, which may explain the detrimental impact of Ni addition on the hydrogen pick-up properties.

8.2.3 Barrier oxide

While the metal-oxide interface region proved to be highly suitable for APT analysis, the true obstacle for hydrogen ingress is the barrier oxide. For this reason, the focus of the APT analyses was shifted from the suboxide and outermost metal grains to the interior of the barrier layer. The oxide has low electrical and thermal conductivity, is a poor absorber of green light and contains high internal stresses as well as large numbers of lateral cracks and voids. All of these factor contribute to induce premature fracture of APT tips during analysis, and has a detrimental impact on the quality of the mass spectra. This means that a slightly different approach to sample preparation and APT analysis was required. Visits to other universities with APT instruments equipped with UV lasers did not significantly improve oxide analyses. Laser-pulsing with green light at higher intensities was instead used and the number of prepared tips was increased to compensate for the high failure rate of the specimens. After some painstaking efforts a large body of data from the barrier layer was accumulating.

The concentrations of Sn that is added to commercial zirconium alloys are fully soluble in the α-Zr matrix. This could be confirmed from the APT analysis of the metal in this work. However, as data from the oxide was collected, it transpired that the Sn distribution was altered compared to the metal. Clusters of Sn were detected close to the metal-oxide interface, and a few hundred nanometers out in the oxide, fully developed Sn particles were observed (see ***Paper IV***).

Upon inspection of the SPPs in the oxide, it became apparent that the Fe distribution also changed after incorporation in the oxide scale. While the oxide-embedded $Zr(Fe,Cr)_2$ SPPs close to the metal-oxide interface showed similar composition as those in the metal, albeit with some oxygen ingress, particles several hundred nanometers out in the barrier layer were seen to be very low in Fe content.

For thermodynamic evaluation of oxide growth in multiple component metallic alloys, Ellingham diagrams[195] are often consulted. Although chemical kinetics is not accounted for, Ellingham diagrams describe the stability of metallic species at various temperatures as a function of partial pressure of an oxidizing agent (and conversely: the stability of an oxide as a function of partial pressure of a reducing agent). In the protective regime of the Zr oxidation cycle, a gradient in oxygen partial pressure

exists across the barrier layer. As all alloying elements in Zr alloys are more noble than Zr itself, it is expected (and observed[196]) that they remain metallic for some time after incorporation in the oxide scale.

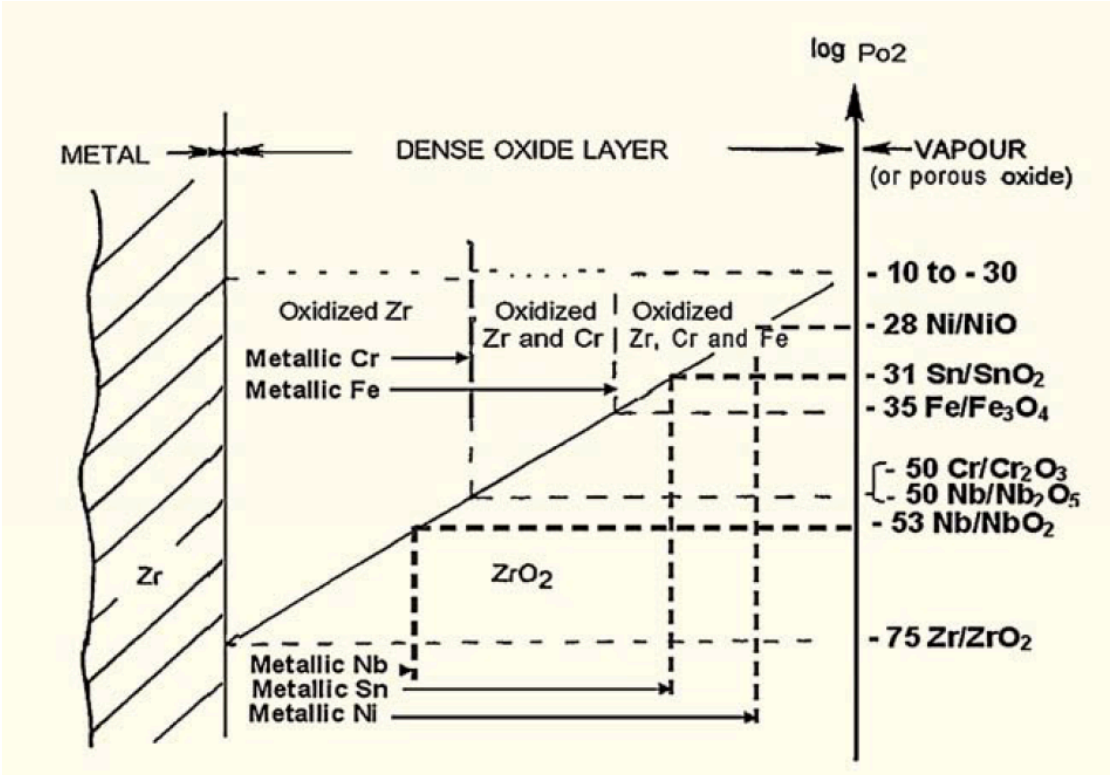

Figure 8.6: Stability (Ellingham) diagram of alloying elements in the oxide as a function of oxygen partial pressure[70].

Correspondingly for Sn, a thermodynamic driving force to remain metallic exists across the inner part of the barrier layer in the passive regime. As Sn is fully soluble in the α-Zr matrix, it will likely be incorporated in the oxide at substitutional Zr sites. The observed clustering, and subsequent precipitation of Sn is interpreted in the light of the Ellingham diagram as a sign of the driving force to stay metallic at the effective local oxygen partial pressure.

Partitioning of Fe and Cr in the $Zr(Fe, Cr)_2$ particles in the oxide has also been reported in the literature[67], and the results from this study are in good agreement with these observations. It was found here that the Fe:Cr ratio is unchanged up to an SPP oxygen content of approximately 50%, after which Fe segregation occurs. Cr is more active than Fe, and when the Cr in the particles is no longer stable, Fe segregates in order to remain in a metallic state. Thus it appears that the Ellingham diagram can successfully predict the behavior also of Fe and Cr in the oxide. Due to the low number density of $Zr_2(Fe, Ni)$ SPPs, and the limited APT analysis yields in the oxide, too few particles from this family could be analyzed to draw any conclusions regarding their behavior through the oxide scale.

8.2.4 Hydrogen in the oxide

One of the fundamenal predictions of the Lindgren and Panas model for hydrogen pickup is the presence of hydroxide species along oxide crystallite boundaries. These hydroxide bonds had been inferred from FTIR spectroscopy of the oxide by

Ramasubramanian previously[64,85], but their location in the oxide had not been confirmed. Therefore special attention was given to possible hydrogen-containing peaks in grain boundaries in the APT data. Although no explicit crystallographic information can be retrieved from the oxide, the previously demonstrated presence of Fe could be used to identify grain boundaries. When evaluating the hydrogen-containing signals in the APT mass spectra from the oxide, it quickly became apparent that the OH^+ peak at 17 Da would often co-localize with Fe along planar features in the oxide. While this is a first indication of hydrogen enrichment, the initial experiments on Ni-based material revealed that H_2 adsorption from the chamber had a strong dependence on electric field and the elevated hydrogen level at grain boundaries might therefore be an artifact. For this reason it was decided that the best way to go forward would be to make use of deuterium, to enable discrimination between corrosion products and adsorbed gas.

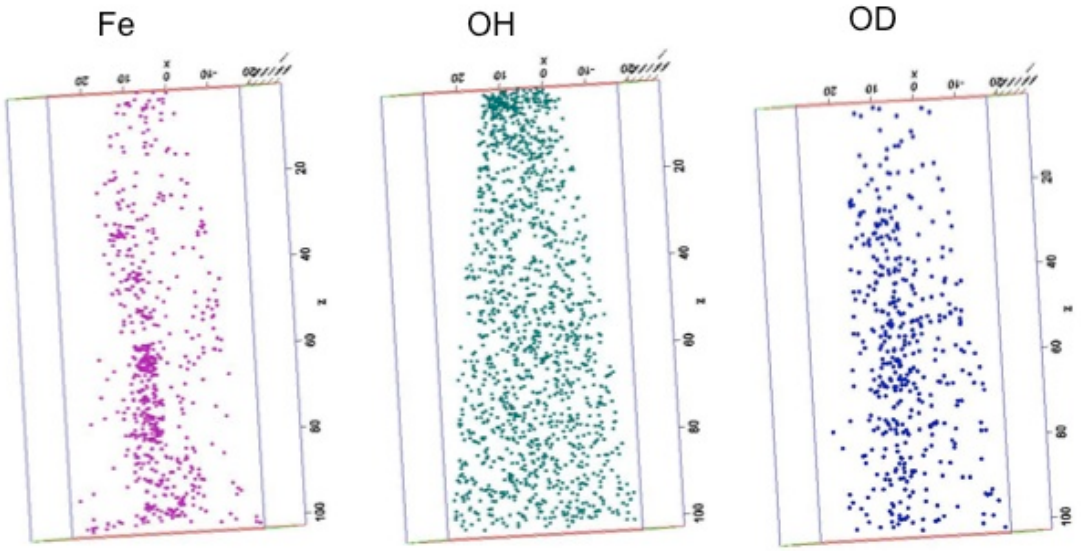

Figure 8.7: Spatial distribution of the Fe^{2+}, OH^+ and OD^+ ions in a mass spectrum from oxide of the Zr-2.5Nb material corroded in D_2O. The OH^+ peak in this spectrum stems solely from adsorbed hydrogen species in the analysis chamber, as no hydrogen was present during the corrosion process.

Unlike European LWR designs, Canadian CANDU reactors use heavy water (D_2O) as moderator. Contact was therefore made with the research center at Atomic Energy of Canada Limited (AECL), who agreed to supply a Zr-2.5Nb material exposed exclusively to heavy water in autoclaves. APT analysis of the D_2O-corroded samples revealed that the localized hydrogen-containing peak at 17 Da was shifted to higher mass by 1 Da, and was instead found at 18 Da in the spectra (see ***Paper VI***). This shift is a very strong indication that the hydrogen uptake through the passive oxide occurs along crystallite boundaries. Moreover, the scarcity with which these H and D-decorated boundaries were encountered in the APT analyses suggests a localized uptake process, where only a limited fraction of boundaries in the oxide are active channels for hydrogen transport.

If one postulates that the cathodic half-cell reaction takes place *within* the oxide scale, then one is also left to explain where the evolving H_2 gas ends up if it does *not* enter the metal. As SPPs can be assumed to act as active cathodes due to their positive

electrochemical potential with respect to the Zr matrix[197], the void that is typically found above the particles can also be expected to contain trapped H_2. Likewise, if grain boundaries are active cathodes as proposed by Lindgren and Panas[198], we should also expect to find signs of gas evolution between oxide crystallites. TEM foils from the barrier layer were therefore prepared, and grain boundaries were subsequently imaged using a Fresnel contrast technique[199] to look for porosity. Consistent with TEM studies of other Zr alloys[116,200,201], pores of a few nanometers in size were indeed found along boundaries in the oxide (see ***Paper VII***). Considering that the barrier oxide is under large compressive stresses[30,44,56], one would expect such porosity to be stabilized by a high gas pressure. The porosity is often seen to form networks along the boundaries that suggest that evolving gas may also escape through the oxide to the coolant.

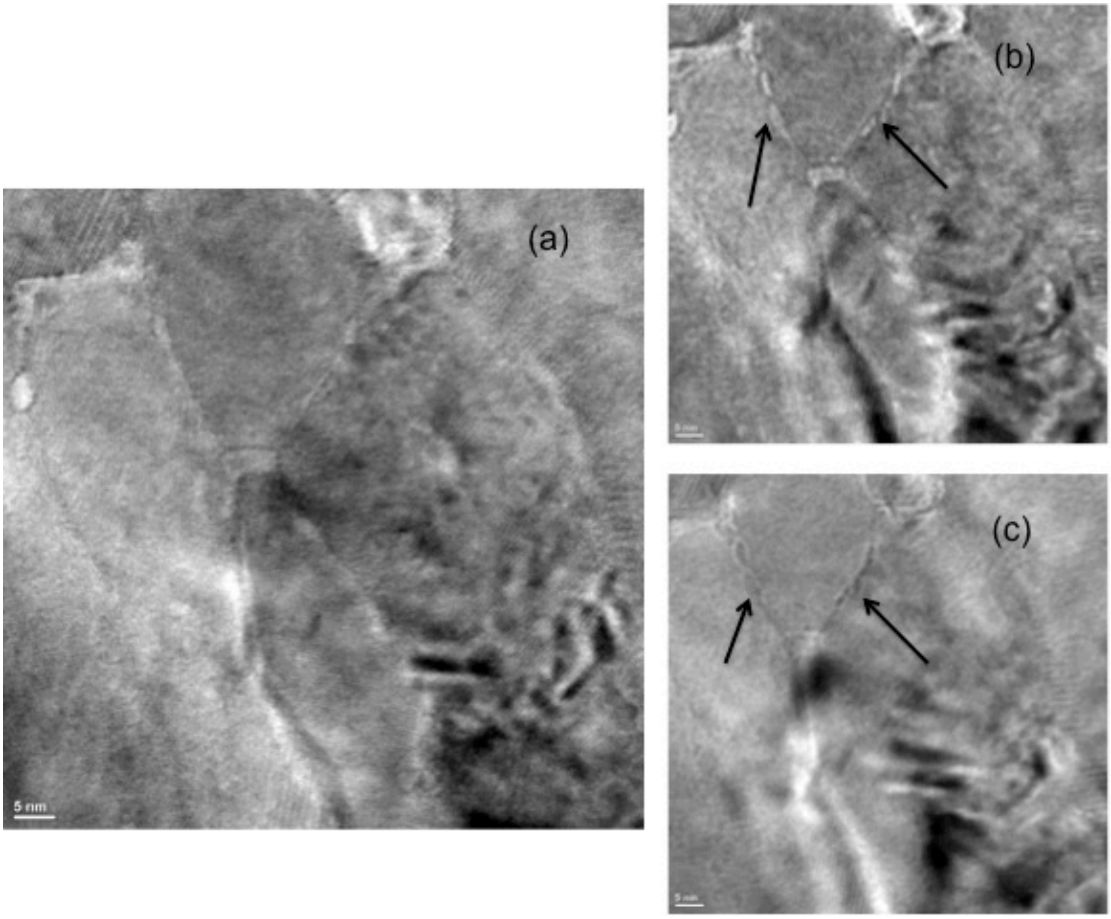

Figure 8.8: In-focus bright field (a) and Fresnel contrast imaging (b) and (c) of the porosity along oxide grain boundaries.

8.2.5 Hydrogen pick-up mechanism

Based on the findings in the this work the following understanding of the hydrogen pick-up mechanism during a corrosion cycle emerges:

- Upon the first exposure of the alloy surface to the coolant, the rate of oxidation is very fast. The oxide layer is at this stage electronically short-circuited by SPPs that penetrates the scale, or by a Cabrera-Mott type electron

tunneling process[202]. This leads to a low instantaneous hydrogen pick-up as hydrogen may evolve at an oxide-water interface.

- As the oxide grows to a thickness of a few hundred nanometers, the larger SPPs do no longer pierce the scale and the growth rate slows down. Embedded SPPs may still serve as active cathodes, reducing the pick-up fraction. At this point, the volume expansion of the oxide will start to induce creep deformation of the underlying metal, causing Fe (and where applicable also Ni) to segregate.
- At an oxide thickness of approximately 1 μm, the surface is passivated. Due to slow electron transport through the insulating oxide, hydrogen has to move inward along grain boundaries in the form of hydroxyls, drawing the cathode closer to the metal-oxide interface. This is reflected in the development of grain boundary porosity in the oxide where H_2 evolves. Hydrogen pick-up is suppressed if the local electron transport is enhanced in Fe-doped boundaries. At this point, the instantaneous hydrogen pick-up is high.
- When the metal can no longer accommodate the stresses that are induced by the growing oxide, the oxide fractures and suffers a mechanical breakdown. The passivity of the oxide is lost as vertical cracks causes water to permeate to the metal-oxide interface, and a new corrosion cycle begins.
- Water penetrating the depth of the scale through lateral cracks will lead to rapid oxidation rates at transition. This will quickly release large amounts of H_2 in the cavities, leading to elevated local partial pressures. The hydrogen pick-up rates are therefore higher *after* the first transition, as cathodic reactions no longer occur at the outer surface of the cladding.

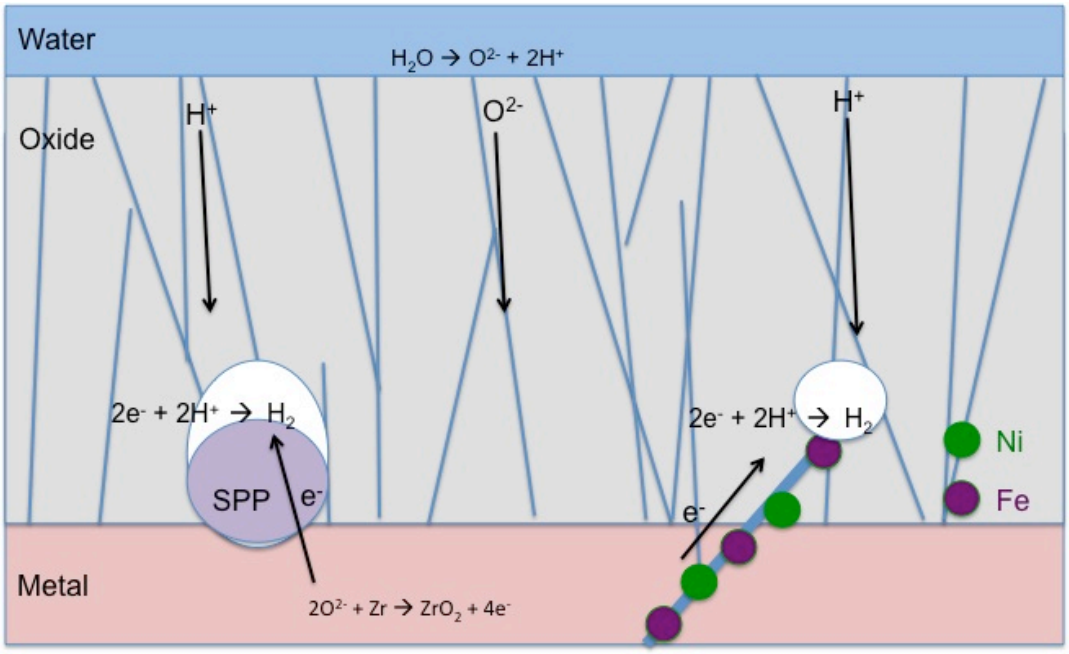

Figure 8.9: Schematic of how reduction sites within the oxide mitigate hydrogen pick-up by moving the cathode away from the metal during the passive oxide regime. Note that oxygen moves as vacancies are being generated by oxidation at the metal-oxide interface.

8.2.6 Matrix chemistry and irradiation effects

In parallel to the corrosion and hydrogen pick-up studies that are primarily related to the properties of the oxide and the metal-oxide interface region, APT analyses of bulk metal samples have also been conducted. One longstanding unresolved issue has been the concentration of transition metal alloying elements in α-Zr matrix[40,52,66,152,203]. As these concentrations are very low, they have proved difficult to unequivocally determine with conventional techniques. APT is in principle capable of determining concentrations as low as a few atomic ppm under ideal conditions and is therefore ideally suited to the task.

A β-quenched Zircaloy-2 material was subjected to a series of annealing times at 770 °C followed by various cooling times[40]. The matrix content of Fe, Cr, Al and Ni were then evaluated and compared to the concentrations found in a commercial LK3 cladding material (see ***Paper VIII***). It was evident that some solubility of Fe and Cr exists at 770 °C. With very fast cooling rates, it is possible to retain approximately 60 wt ppm of Cr and 10-15 wt ppm of Fe in solution. No Ni was detected in the matrix. The matrix of the commercial alloy was found to contain virtually no Cr and Ni and approximately 15 wt ppm of Fe.

Owing to collaboration with Studsvik Nuclear AB, a series of samples from Zircaloy-2 cladding materials (LK3) exposed in BWR power plants could also be analyzed with APT (see ***Paper IX***). Due to the high failure rate of specimen from the oxide, it was decided that this study should be dedicated to analysis of the bulk metal, as only a small number of samples would be made available for cost and sample activity reasons. In combination with the analyses of the fresh β-quenched material, this would allow for mapping of the alloying element distribution over a life cycle of the cladding. Exposure times of special interest were identified to be 3 and 9 annual cycles of exposure, corresponding to equivalent doses of approximately 15 and 40 dpa, respectively. Samples were retrieved with the *in situ* FIB-SEM lift-out technique at the Studsvik laboratory, and subsequently brought to Chalmers, where tips were finally sharpened, also using FIB-SEM. The irradiated metal matrix turned out to be surprisingly well suited to APT analysis, which meant large volumes of data could be collected from a limited number of samples at hand.

Already after 3 cycles inside the reactor, Fe concentrations in the matrix are elevated with respect to the fresh material. Signs of nanoscale clustering are apparent, although Fe concentration varies between different analyses. The cluster number densities agree reasonably well with what is expected for <a>-loops, and it is likely that they nucleate at, or in the strain field of such crystal defects. The Sn distribution is not entirely homogeneous throughout the matrix, and segregation features that are interpreted to be dislocation strain fields were observed. Little Cr and no Ni were found in the matrix of the 3 cycle material.

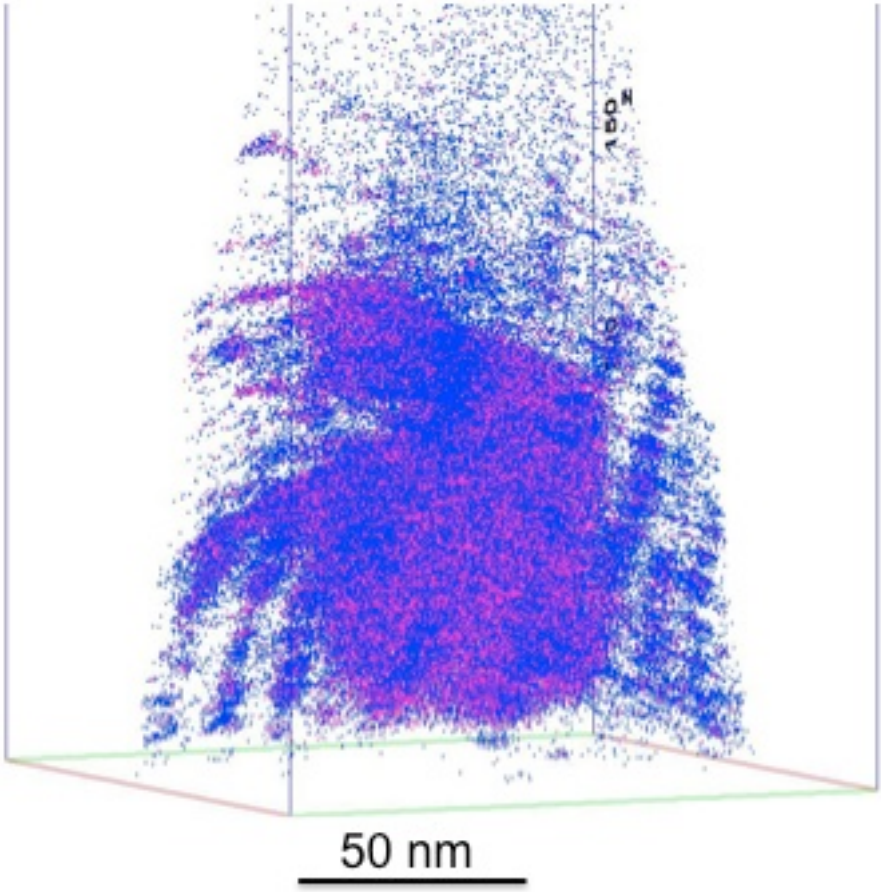

Figure 8.10: Migration of Fe (blue) and Cr (pink) out of an SPP along basal planes in 3 cycle Zircaloy-2 cladding.

After 3 cycles, SPP dissolution could readily be observed with APT. Fe, and to a lesser extent Cr, moves out of the particles along basal planes, where they form clusters (see figure 8.10). The clusters are aligned on planar features that are believed to be basal planes in the crystal. This is in strikingly good agreement with TEM observations from the same material[186] (compare e.g. with figure 7.2). At this point, the $Zr(Fe, Cr)_2$ particles have lost virtually all their Fe content to the matrix.

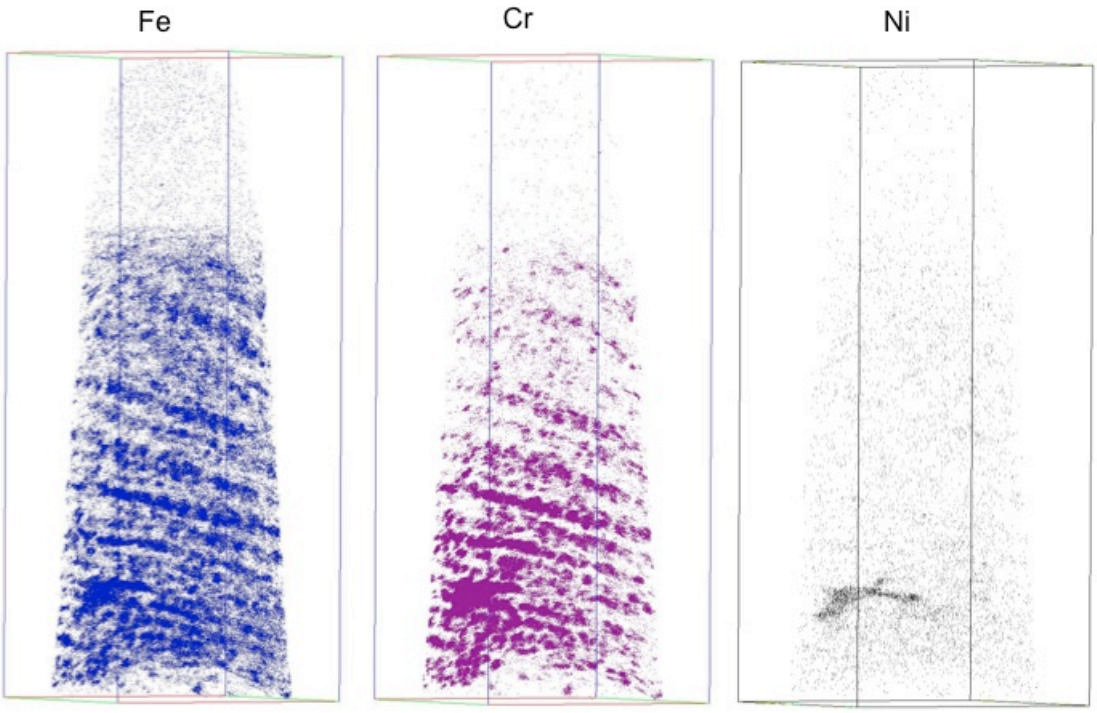

Figure 8.11: Typical distributions of Fe, Cr and Ni in the matrix of the 9 cycle Zircaloy-2 fuel cladding. The size of the box is 120x120x400 nm^3.

In the 9 cycle material, large number densities of Fe and Cr-rich clusters were encountered over most of the metal matrix (see figure 8.11). As in the 3 cycle samples, clusters are arranged in planes with approximately 10 nm spacing, believed to be basal planes. Comparison with TEM micrographs[186] implies that they are related to <a>-loops. In regions where little Fe and Cr were detected, Sn showed signs of similar cluster formation. A distinct anti-correlation between Fe and Cr segregation and Sn segregation was evident. In a few analyses of the 9 cycle material, small amounts of Ni were seen in the matrix. Ni appears to exhibit similar segregation behavior as Fe, and was exclusively found in nanosized clusters together with Fe and Cr.

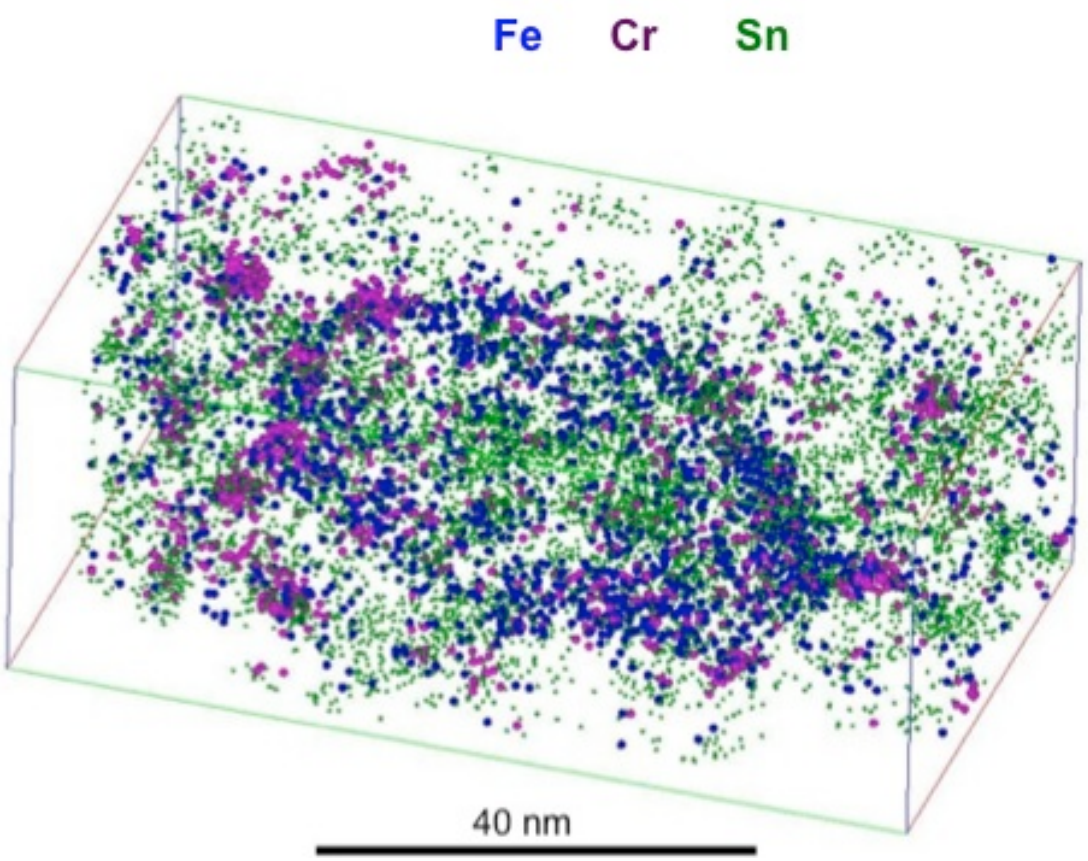

Figure 8.12: Segregation of Fe, Cr and Sn around a <c>-loop in the material subjected to 9 annual in-reactor cycles.

The accelerated growth phenomenon is often linked with the formation of <c>-component loops in the structure[135,140]. APT analysis revealed that the dislocation line of the <c>-loops was decorated with Fe, and Cr clusters were dotted along their periphery (see figure 8.12). In regions low in Fe and Cr, signs of interaction between Sn and <c>-loops were observed. As <c>-component loops are believed to be unstable in a pure α-Zr matrix, it is likely that Fe serves as a loop stabilizer, thereby promoting irradiation growth. Already after 3 cycles, Fe is relatively abundant in the matrix compared to the fresh material, as a result of SPP dissolution. After 9 cycles, significant amounts of Fe are spread out across the matrix, which facilitates nucleation of large number densities of <c>-component loops.

9. Suggestions for future work

Over the course of this project, a number of ideas for complementary experiments to further expand the understanding of the hydrogen pick-up process have emerged. Following on from previous work by Cox[83], it is essential to gain a better understanding of the electrochemical kinetics of the cathodic reactions. Therefore, it would be of interest to perform *in situ* corrosion testing in an environmental scanning electron microscope (ESEM). This technique enables direct imaging of a wet corroding surface under a low H_2O pressure at elevated temperatures. Active cathodic sites should under such circumstances be evolving H_2 gas, possibly visible through bubble formation on the surface. By subsequently using a FIB-SEM, cross-sections from sites of hydrogen evolution can be produced for careful structural and chemical analysis.

If, as is postulated in this thesis, hydrogen evolves in the interior of the barrier layer during the protective regime, a fast oxidation process at high temperatures may leave pockets of H_2 within the oxide scale. These relatively large H_2 quantities may be detected with vibrational spectroscopy techniques[204] or Raman scattering[205]. Electron energy loss spectroscopy (EELS) in using TEM has been successfully applied to measure other gases in nanosized cavities in different materials[206–208]. Although it is unlikely that the volatile H_2 gas would remain in cavities during TEM sample preparation and subsequent analysis under the electron beam, this may be an experimental approach worth pursuing.

The atom probe technique has great potential for correlative microanalysis, for instance in conjunction with TEM[178]. As the hydrogen pick-up is likely to be localized to certain grain boundaries in the oxide, it would be of interest to correlate APT analysis with crystallographic studies, such as scanning nanobeam diffraction[209] (NBD) or transmission Kikuchi diffraction[210] (TKD). With these methods, possible preferential grain boundary misorientation angles for hydrogen migration could be elucidated.

Finally, it should be noted that autoclave corrosion is an inadequate simulation of the real in-reactor degradation process. The initial APT studies of irradiated materials that are presented in this thesis merely give a hint of the substantial microstructural changes that the cladding undergoes during service in the core. If the in-reactor corrosion process is to be fully understood, extensive examinations of cladding materials that have been subjected to real nuclear reactor conditions are required.

Acknowledgements

Financial support for this project was provided by Westinghouse Electric Sweden AB, Sandvik Materials Technology AB, Vattenfall Nuclear Fuel AB, the Electric Power Research Institute (EPRI) and the Swedish Research Council (Vetenskapsrådet).

On a personal level, I would like to thank a number of people for their help and assistance in the creation of this thesis:

First of all my main supervisor Prof. Hans-Olof Andrén for guidance, support and contagious enthusiasm for the subjects of zirconium corrosion and atom probe analysis. I am also very thankful for your excellent project leadership skills and ability to always give constructive feedback on manuscripts and presentations, however busy you are!

My co-supervisor Dr Mattias Thuvander for introducing me to all the practicalities of atom probe tomography, and always taking the time to discuss experiments and results. I am also very grateful for being given the opportunity to pursue other research topics, which has made PhD life even more inspiring and exciting.

My colleagues Prof. Itai Panas and Mikaela Lindgren from the Chemistry Department for a very good and stimulating collaboration, and for their good company at meetings and conferences.

The industrial participants in the project group from Sweden; Lars Hallstadius, Mats Dahlbäck, Magnus Limbäck, Maria Ivermark, Kenneth Göransson, Pascale Sotto-Vangeli and Mats Åslund at Westinghouse, Mattias Ahlm, Per Witt and Jonas Lundin at Sandvik, Bertil Josefsson and David Schrire at Vattenfall and Aylin Kucuk at EPRI for their important and valuable scientific input at our meetings.

Lars Hallstadius and Mats Dahlbäck at Westinghouse, and Pia Tejland and Daniel Jädernäs at Studsvik for facilitating work with irradiated samples.

The participants in the international MUZIC-2 program for fruitful scientific discussion at out meetings.

My officemates during my time at Chalmers Pavleta, Amine and Dr Boll for keeping me in good company.

The infrastructure unit at Applied Physics, particularly Anders Kvist and Ola Löfgren, for their technical support.

All the past and present members of the M2 and EOG divisions for creating a nice working environment, among them; distinguished Star Trek-enthusiast Torben Boll, spiritual counselor Olof Bäcke, wisecracking funnymen Stefan Gustafsson and Anders Kvist, zorroing Excel-connoisseur Jonathan Weidow, supportive mentor and travel-organizer Krystyna Stiller and my personal language teachers Amine Yousfi (French), Leif Viskari (Australian English) and Haiping Lai (Haipinglish).

As I suspect that my parents Kickan and Gunnar will take special interest in this particular section of the thesis, I will take the opportunity to express my gratitude to them too. Thank you for your support and encouragement through this work and beyond!

Finally, thanks to my delightful late grandmother Gunnel, my outstanding brother Erik and my amazing sister Kerstin for inspiration!

Göteborg, March 2015

References

1. Nelson, J. *The physics of solar cells*. (World Scientific, 2003).

2. Ackermann, T. *Wind power in power systems*. (Wiley Online Library, 2005).

3. Koppejan, J. & Van Loo, S. *The handbook of biomass combustion and co-firing*. (Routledge, 2012).

4. Warner, E. S. & Heath, G. A. Life cycle greenhouse gas emissions of nuclear electricity generation. *J. Ind. Ecol.* **16,** S73–S92 (2012).

5. Nuclear Power in China (retrieved 2015-02-06). at <http://www.world-nuclear.org/info/Country-Profiles/Countries-A-F/China--Nuclear-Power/>

6. Cengel, Y. A., Boles, M. A. & Kanoglu, M. *Thermodynamics: an engineering approach*. (McGraw-Hill New York, 1998).

7. Franklin, D. G. & Lang, P. M. Zirconium-alloy corrosion. A review based on an International Atomic Energy Agency (IAEA) meeting. *Zirconium in the Nuclear Industry: 9th International Symposium, ASTM STP 1132* 3–30 (1991).

8. Adamson, R., Garzarolli, F., Cox, B., Strasser, A. & Rudling, P. *ZIRAT12 Special Topic Report: Corrosion Mechanisms in Zirconium Alloys , IZNA7-8, Advanced Nuclear Technology International Europe AB*. (2007).

9. Lemaignan, C. & Motta, A. T. in *Materials Science and Technology - A Comprehensive Treatment, Volume 10B: Nuclear Materials Part II* (eds. Cahn, R. W., Haasen, P., Krams, E. J. & Frost, B. T.)

10. Pomerance, H. Thermal Neutron Capture Cross Sections. *Phys. Rev.* **88,** 412–413 (1952).

11. Goldak, J., Lloyd, L. T. & Barrett, C. S. Lattice Parameters, Thermal Expansions, and Grüneisen Coefficients of Zirconium, 4.2 to 1130K. *Phys. Rev.* **144,** 478–484 (1966).

12. Kasap, S. O. *Principles of electronic materials and devices*. **81,** (McGraw-Hill New York, NY, 2006).

13. Adamson, R. B. Effects of neutron irradiation on microstructure and properties of Zircaloy. *Zirconium in the Nuclear Industry: 12th International Symposium, ASTM STP 1354* 15–31 (2000).

14. Holt, R. A. & Ibrahim, E. F. Factors affecting the anisotropy of irradiation creep and growth of zirconium alloys. *Acta Metall.* **27,** 1319–1328 (1979).

15. Östberg, G. Determination of the composition of the second phase in Zircaloy. *J. Nucl. Mater.* **7,** 103–106 (1962).

16. Östberg, G. & Attermo, R. Structure transformations in Zircaloy-2 during hot working processes. *J. Nucl. Mater.* **5,** 120–127 (1962).

17. Knorr, D. B. & Pelloux, R. M. Quantitative characterization of crystallographic textures in zirconium alloys. *J. Nucl. Mater.* **71,** 1–13 (1977).

18. Cheadle, B. A., Ells, C. E. & Evans, W. The development of texture in zirconium alloy tubes. *J. Nucl. Mater.* **23,** 199–208 (1967).

19. Andersson, T., Thorvaldsson, T., Wilson, A. & Wardle, A. M. Improvements in Water Reactor Fuel Technology and Utilization. *IAEA, Vienna, Austria* 435–449 (1987).

20. Tejland, P. & Andrén, H. O. Origin and effect of lateral cracks in oxide scales formed on zirconium alloys. *J. Nucl. Mater.* **430,** 64–71 (2012).

21. Tenckhoff, E. *Deformation mechanisms, texture, and anisotropy in zirconium and zircaloy*. (ASTM International, 1988).

22. Tenckhoff, E. Review of deformation mechanisms, texture, and mechanical anisotropy in zirconium and zirconium base alloys. *Zirconium in the Nuclear Industry: 14th International Symposium, ASTM STP 1467* 26–49 (2005).

23. Akhtar, A. & Teghtsoonian, A. Plastic deformation of zirconium single crystals. *Acta Metall.* **19,** 655–663 (1971).

24. Onimus, F., Monnet, I., Béchade, J. L., Prioul, C. & Pilvin, P. A statistical TEM investigation of dislocation channeling mechanism in neutron irradiated zirconium alloys. *J. Nucl. Mater.* **328,** 165–179 (2004).

25. Onimus, F., Béchade, J. L., Duguay, C., Gilbon, D. & Pilvin, P. Investigation of neutron radiation effects on the mechanical behavior of recrystallized zirconium alloys. *J. Nucl. Mater.* **358,** 176–189 (2006).

26. Cox, B. Some thoughts on the mechanisms of in-reactor corrosion of zirconium alloys. *J. Nucl. Mater.* **336,** 331–368 (2005).

27. Cox, B. & Pemsler, J. P. Diffusion of oxygen in growing zirconia films. *J. Nucl. Mater.* **28,** 73–78 (1968).

28. Bedworth, R. & Pilling, N. The Oxidation of Metals at High Temperatures. *J Inst. Met.* **29,** 529–591 (1923).

29. Tejland, P. & Andrén, H.-O. Oxidation induced localized creep deformation in Zircaloy-2. *J. Nucl. Mater.* **444,** 30–34 (2014).

30. Platt, P. *et al*. A study into stress relaxation in oxides formed on zirconium alloys. *J. Nucl. Mater*. **456,** 415–425 (2015).

31. Hillner, E., Franklin, D. G. & Smee, J. D. Long-term corrosion of Zircaloy before and after irradiation. *J. Nucl. Mater*. **278,** 334–345 (2000).

32. Abriata, B. J. P., Bariloche, C. A., Versaci, R. & Constituyentes, C. A. The O-Zr (Oxygen-Zirconium) System. *Bull. Alloy Phase Diagrams* **7,** 116–124 (1986).

33. Béranger, G. & Lacombe, P. Contribution a l'étude de la cinetique de l'oxydation du zirconium α et de la diffusion de l'oxygène dans le metal sous-jacent a l'oxyde. *J. Nucl. Mater*. **16,** 190–207 (1965).

34. Dünwald, H. & Wagner, C. Influence of constitution of cuprous oxide on electrical properties. *Zeitschrift für Phys. Chemie* **22,** 212–215 (1933).

35. Motta, A. T. *et al*. Microstructure and growth mechanism of oxide layers formed on Zr alloys studied with micro-beam synchrotron radiation. *Zirconium in the Nuclear Industry: 14th International Symposium, ASTM STP 1467* 205–232 (2005).

36. Nanikawa, S. *et al*. Correlation between characteristics of oxide films formed on Zr alloys in BWRs and corrosion performance. *Zirconium in the Nuclear Industry: 12th International Symposium, ASTM STP 1354* 815–835 (2000).

37. Yilmazbayhan, A., Breval, E., Motta, A. T. & Comstock, R. J. Transmission electron microscopy examination of oxide layers formed on Zr alloys. *J. Nucl. Mater*. **349,** 265–281 (2006).

38. Tejland, P. & Andrén, H. O. Origin and effect of lateral cracks in oxide scales formed on zirconium alloys. *J. Nucl. Mater*. **430,** 64–71 (2012).

39. Parise, M., Sicardy, O. & Cailletaud, G. Modelling of the mechanical behavior of the metal–oxide system during Zr alloy oxidation. *J. Nucl. Mater*. **256,** 35–46 (1998).

40. Hutchinson, B., Lehtinen, B., Limbäck, M. & Dahlberg, M. A study of the structure and chemistry in Zircaloy-2 and the resulting oxide after high temperature corrosion. *Zirconium in the Nuclear Industry: 15th International Symposium, ASTM STP 1505* 269–281 (2007).

41. Godlewski, J. Raman Spectroscopy Study of the Tetragonal-to-Monoclinic Transition in Oxide Scales and Determination of Overall Oxygen Diffusion by Nuclear Microanalysis of O18. *Zirconium in the Nuclear Industry: 9th International Symposium, ASTM STP 1132* 416–435 (1991).

42. Garzarolli, F., Seidel, H., Tricot, R. & Gros, J. P. Oxide growth mechanism on zirconium alloys. *Zirconium in the Nuclear Industry: 9th International Symposium, ASTM STP 1132* 395–415 (1991).

43. Wei, J. *et al*. The effect of Sn on autoclave corrosion performance and corrosion mechanisms in Zr-Sn-Nb alloys. *Acta Mater*. **61,** 4200–4214 (2013).

44. Polatidis, E. *et al*. Residual stresses and tetragonal phase fraction characterisation of corrosion tested Zircaloy-4 using energy dispersive synchrotron X-ray diffraction. *J. Nucl. Mater*. **432,** 102–112 (2013).

45. Yardley, S. S. *et al*. An investigation of the oxidation behaviour of zirconium alloys using isotopic tracers and high resolution SIMS. *J. Nucl. Mater*. **443,** 436–443 (2013).

46. David, G., Geschier, R. & Roy, C. Etude de la croissance de l'oxyde sur le zirconium et le zircaloy-2. *J. Nucl. Mater*. **38,** 329–339 (1971).

47. Bouineau, V. *et al*. A New Model to Predict the Oxidation Kinetics of Zirconium Alloys in a Pressurized Water Reactor. *Zirconium in the Nuclear Industry: 15th International Symposium, ASTM STP 1505* 405–429 (2008).

48. Cox, B. The Oxidation and Corrosion of Zirconium and its Alloys V. Mechanism of Oxide Film Growth and Breakdown on Zirconium and Zircaloy-2. *J. Electrochem. Soc*. **108,** 24–30 (1961).

49. Kofstad, P. *High temperature oxidation of metals. John Wiley & Sons Inc., New York, N. Y* (1966).

50. Atkinson, A. Transport processes during the growth of oxide film at elevated temperature. *Rev. Mod. Phys*. **57,** 437–470 (1985).

51. Garner, A. *et al*. The microstructure and microtexture of zirconium oxide films studied by transmission electron backscatter diffraction and automated crystal orientation mapping with transmission electron microscopy. *Acta Mater*. **80,** 159–171 (2014).

52. Kruger, R. M., Adamson, R. B. & Brenner, S. S. Effects of microchemistry and precipitate size on nodular corrosion resistance of Zircaloy-2. *J. Nucl. Mater*. **189,** 193–200 (1992).

53. Garzarolli, F., Cox, B. & Rudling, P. Corrosion and Hydriding (A.N.T. International Report). (2012).

54. Kuwae, R., Sato, K., Higashinakagawa, E., Kawashima, J. & Nakamura, S. Mechanism of zircaloy nodular corrosion. *J. Nucl. Mater*. **119,** 229–239 (1983).

55. Motta, A. T. *et al*. Microstructural characterization of oxides formed on model Zr alloys using synchrotron radiation. *Zirconium in the Nuclear Industry: 15th International Symposium, ASTM STP 1505* 486–506 (2008).

56. Preuss, M. *et al*. Studies regarding corrosion mechanisms in zirconium alloys. *Zirconium in the Nuclear Industry: 16th International Symposium, ASTM STP 1529* 649–681 (2011).

57. Frankel, P. *et al*. The effect of Sn on corrosion mechanisms i advanced Zr-cladding for PWR. *Zirconium in the Nuclear Industry: 17th International Symposium, ASTM STP 1543* (2014).

58. Pêcheur, D., Filippov, V. P., Bateev, A. B. & Ivanov, J. J. Mössbauer investigations of the chemical states of tin and iron atoms in zirconium alloy oxide film. *Zirconium in the Nuclear Industry: 13th International Symposium, ASTM STP 1423* 135–151 (2002).

59. Hulme, H. *et al*. An X-ray absorption near-edge structure (XANES) study of the Sn L3 edge in a Zircaloy-4 oxide film. *Submitt. Publ.*

60. Tupin, M., Pijolat, M., Valdivieso, F. & Soustelle, M. Oxidation kinetics of ZrNbO in steam: Differences between the pre- and post-transition stages. *J. Nucl. Mater.* **342,** 108–118 (2005).

61. Klepfer, H. H. Zirconium — niobium binary alloys for boiling water reactor service part I — corrosion resistance. *J. Nucl. Mater.* **9,** 65–76 (1963).

62. Ibrahim, E. F. & Cheadle, B. A. Development of zirconium alloys for pressure tubes in CANDU reactors. *Can. Metall. Q.* **24,** 273–281 (1985).

63. Coleman, C. E., Gilbert, R. W., Carpenter, G. J. C. & Weatherly, G. C. Precipitation in Zr-2. 5 Wt.-% Nb During Neutron Irradiation. *Phase Stab. Dur. Irradiat.* 587–599 (1980).

64. Ramasubramanian, N., Perovic, V. & Leger, M. Hydrogen Transport in the Oxide and Hydrogen Pickup by the Metal During Out-and In-Reactor Corrosion of Zr-2.5 Nb Pressure Tube Material. *Zirconium in the Nuclear Industry: 12th International Symposium, ASTM STP 1354* 853–876 (2000).

65. Wadman, B. & Andren, H.-O. Microanalysis of the matrix and the oxide–metal interface of uniformly corroded Zircaloy. in *Zirconium in the Nuclear Industry: 9th International Symposium, ASTM STP 1132* 461–475 (1991).

66. Ivermark, M. Characterisation of the Matrix Chemistry in Zirconium Alloys. *PhD Thesis, Univ. Manchester* (2009).

67. Pêcheur, D., Lefebvre, F., Motta, A. T., Lemaignan, C. & Wadier, J. F. Precipitate evolution in the Zircaloy-4 oxide layer. *J. Nucl. Mater.* **189,** 318–332 (1992).

68. Cheng, B.-C., Kruger, R. M. & Adamson, R. B. Corrosion behaviour of irradiated Zircaloy. *Zirconium in the Nuclear Industry: 10th International Symposium, ASTM STP 1245* 400–418 (1994).

69. Chemelle, P., Knorr, D. B., Van Der Sande, J. B. & Pelloux, R. M. Morphology and composition of second phase particles in Zircaloy-2. *J. Nucl. Mater.* **113,** 58–64 (1983).

70. Garzarolli, F., Cox, B. & Rudling, P. Optimization of Zry-2 for high burnups. *Zirconium in the Nuclear Industry: 16th International Symposium, ASTM STP 1529* 711–727 (2011).

71. Wang, C. T., Eucken, C. M. & Graham, R. A. Investigation of nodular corrosion mechanism of Zircaloy products. *Zirconium in the Nuclear Industry: 9th International Symposium, ASTM STP 1132* 319–345 (1991).

72. Cox, B. & Sheikh, H. I. Redistribution of the alloying elements during Zircaloy-2 oxidation. *J. Nucl. Mater.* **249,** 17–32 (1997).

73. Cox, B. *et al.* Waterside corrosion of zirconium alloys in nuclear power plants. *IAEA TECDOC* **996,** 124 (1998).

74. Garzarolli, F., Broy, T. & Busch, R. A. Comparison of the Long-Term Behavior of Certain Zirconium Alloys in PWR, BWR and Laboratory Tests. *Zirconium in the Nuclear Industry: 11th International Symposium, ASTM STP 1295* 850–864 (1996).

75. Yang, W. J. S. & Adamson, R. B. Zirconium in the Nuclear Industry. *Zirconium in the Nuclear Industry: 8th International Symposium, ASTM STP 1023* 451–477 (1989).

76. Yang, W. J. S., Tucker, R. P., Cheng, B. & Adamson, R. B. Precipitates in Zircaloy: Identification and the effects of irradiation and thermal treatment. *J. Nucl. Mater.* **138,** 185–195 (1986).

77. Griffiths, M., Gilbert, R. W. & Carpenter, G. J. C. Phase instability, decomposition and redistribution of intermetallic precipitates in Zircaloy-2 and -4 during neutron irradiation. *J. Nucl. Mater.* **150,** 53–66 (1987).

78. Shannon, D. W. Electrical properties of ZrO_2 corrosion films. in *Proc. USAEC Symp. on Zirconium Alloy Development, Castlewood, CA, GE Report GEAP-4089*

79. Klepfer, H. H. Hydrogen uptake of zirconium alloys during water and steam corrosion. *Corrosion* **19,** 285t–291t (1963).

80. Balog, M., Schieber, M., Michman, M. & Patai, S. The chemical vapour deposition and characterization of ZrO 2 films from organometallic compounds. *Thin Solid Films* **47,** 109–120 (1977).

81. Howlader, M. M. R., Shiiyama, K., Kinoshita, C., Kutsuwada, M. & Inagaki, M. The electrical conductivity of zircaloy oxide films. *J. Nucl. Mater.* **253,** 149–155 (1998).

82. Taylor, D. F. An oxide-semiconductance model of nodular corrosion and its application to Zirconium alloy development. *J. Nucl. Mater.* **184,** 65–77 (1991).

83. Cox, B., Gauducheau, F. & Yin-Mei, W. Cathodic sites on Zircaloy surfaces. *J. Nucl. Mater.* **189,** 362–369 (1992).

84. Ramasubramanian, N. Localised electron transport in corroding zirconium alloys. *J. Nucl. Mater.* **55,** 134–154 (1975).

85. Ramasubramanian, N., Billot, P. & Yagnik, S. Hydrogen evolution and pickup during the corrosion of zirconium alloys: a critical evaluation of the solid state and porous oxide electrochemistry. *Zirconium in the Nuclear Industry: 13th International Symposium, ASTM STP 1423* 222–242 (2002).

86. Cox, B. A mechanism for the hydrogen uptake process in zirconium alloys. *J. Nucl. Mater.* **264,** 283–294 (1999).

87. Zuzek, B. E., Abdata, J. R., Barlloche, C. A., Nacional, C. & Atomlca, D. E. The H-Zr (Hydrogen_Zirconium) System. *Bull. Alloy Phase Diagrams* **11,** 385–395 (1990).

88. Zhao, Z. *et al.* Identification and characterization of a new zirconium hydride. *J. Microsc.* **232,** 410–421 (2008).

89. Zhao, Z. *et al.* Characterization of Zirconium Hydrides and Phase Field Approach to a Mesoscopic-Scale Modeling of Their Precipitation. *Zirconium in the Nuclear Industry: 15th International Symposium, ASTM STP 1505* 29–52 (2008).

90. Northwood, D. O. Gamma and delta hydrides in zirconium alloys. *J. Less Common Met.* **48,** 173–175 (1976).

91. Zuzek, E., Abriata, J. P., San-Martin, A. & Manchester, F. D. The H-Zr (hydrogen-zirconium) system. *Bull. Alloy phase diagrams* **11,** 385–395 (1990).

92. Carpenter, G. J. C. Precipitation of Gamma-Zirconium Hydride in Zirconium. *Acta Metall.* **26,** 1225–1235 (1978).

93. Bailey, J. E. Electron microscope observations on the precipitation of zirconium hydride in zirconium. *Acta Metall.* **11,** 267–280 (1963).

94. Bradbrook, J. S., Lorimer, G. W. & Ridley, N. The precipitation of zirconium hydride in Zirconium and Zircaloy-2. *J. Nucl. Mater.* **42,** 142–160 (1972).

95. Blat-Yrieix, M. & Bouffioux, P. *Course Material 'Metallurgy and properties of Zr alloys for nuclear applications' Chapter: 'Impact of H Pick-up: Embrittlement, RIA, post-irradiation creep' CEA, INSTN.* (2011).

96. Blat, M. & Noel, D. Detrimental role of hydrogen on the corrosion rate of zirconium alloys. *Zirconium in the Nuclear Industry: 11th International Symposium, ASTM STP 1295* 319–335 (1996).

97. Blat, M., Legras, L., Noel, D. & Amanrich, H. Contribution to a better understanding of the detrimental role of hydrogen on the corrosion rate of Zircaloy-4 cladding materials. *Zirconium in the Nuclear Industry: 12th International Symposium, ASTM STP 1354* 563–591 (2000).

98. Garde, A. M. Enhancement of aqueous corrosion of zircaloy-4 due to hydride precipitation at the metal-oxide interface. *Zirconium in the Nuclear Industry: 9th International Symposium, ASTM STP 1132* 566–594 (1991).

99. Berry, W. E., Vaughan, D. A. & White, E. L. Hydrogen Pickup During Aqueous Corrosion of Zirconium Alloys. *Corrosion* **17,** 109t–117t (1961).

100. Cox, B. in *Advances in Corrosion Science and Technology* 173–391 (Springer, 1976).

101. Une, K. *et al*. Hydrogen absorption mechanism of zirconium alloys based on characterization of oxide layer. *Zirconium in the Nuclear Industry: 16th International Symposium, ASTM STP 1529* 401–432 (2011).

102. Harada, M. & Wakamatsu, R. The effect of hydrogen on the transition behavior of the corrosion rate of zirconium alloys. *Zirconium in the Nuclear Industry: 15th International Symposium, ASTM STP 1505* 384–404 (2008).

103. Couet, A., Motta, A. T., Comstock, R. J. & Paul, R. L. Cold neutron prompt gamma activation analysis, a non-destructive technique for hydrogen level assessment in zirconium alloys. *J. Nucl. Mater.* **425,** 211–217 (2012).

104. Couet, A., Motta, A. T. & Comstock, R. J. Hydrogen pickup measurements in zirconium alloys: Relation to oxidation kinetics. *J. Nucl. Mater.* **451,** 1–13 (2014).

105. Baur, K., Garzarolli, F., Ruhmann, H. & Sell, H. J. Electrochemical Examinations in 350C Water with Respect to the Mechanism of Corrosion-Hydrogen Pickup. *Zirconium in the Nuclear Industry: 12th International Symposium, ASTM STP 1354* 836–852 (2000).

106. Lindgren, M. *et al*. Towards a comprehensive mechanistic understanding of hydrogen uptake in zirconium alloys by combining atom probe analysis with electronic structure calculations. *Zirconium in the Nuclear Industry: 17th International Symposium, ASTM STP 1543* 1–25 (2014).

107. Kakiuchi, K. *et al*. Effect of iron on hydrogen absorption properties of zirconium alloys. *J. Phys. Chem. Solids* **66,** 308–311 (2005).

108. Bossis, P., Lelièvre, G., Barberis, P., Iltis, X. & Lefebvre, F. Multi-scale characterization of the metal-oxide interface of zirconium alloys. *Zirconium in*

the Nuclear Industry: 12th International Symposium, ASTM STP 1354 918–942 (2000).

109. Hatano, Y., Isobe, K., Hitaka, R. & Sugisaki, M. Role of intermetallic precipitates in hydrogen uptake of Zircaloy-2. *J. Nucl. Sci. Technol.* **33,** 944–949 (1996).

110. Hatano, Y., Hitaka, R., Sugisaki, M. & Hayashi, M. Influence of size distribution of $Zr(Fe, Cr)_2$ precipitates on hydrogen transport through oxide film of Zircaloy-4. *J. Nucl. Mater.* **248,** 311–314 (1997).

111. Elmoselhi, M. B., Warr, B. D. & McIntyre, S. A study of the hydrogen uptake mechanism in zirconium alloys. *Zirconium in the Nuclear Industry: 10th International Symposium, ASTM STP 1245* 62–79 (1994).

112. Cox, B. Pore structure in oxide films on irradiated and unirradiated zirconium alloys. *J. Nucl. Mater.* **148,** 332–343 (1987).

113. Barberis, P. & Frichet, A. Characterization of Zircaloy-4 oxide layers by impedance spectroscopy. *J. Nucl. Mater.* **273,** 182–191 (1999).

114. Oskarsson, M., Ahlberg, E., Södervall, U., Andersson, U. & Pettersson, K. Pre-transition oxidation behaviour of pre-hydrided Zircaloy-2. *J. Nucl. Mater.* **289,** 315–328 (2001).

115. Ni, N. Study of Oxidation Mechanisms of Zirconium Alloys by Electron Microscopy. PhD Thesis, University of Oxford (2011).

116. Ploc, R. A. Mechanism of deuterium pickup in Zr-2.5 Nb alloy. *Mater. High Temp.* **17,** 29–34 (2000).

117. Kido, T., Senda, Y., Tukuta, Y., Hayashi, H. & Murai, K. Quantitative assessment of irradiation effect on creep and corrosion properties of Zr-Base alloys. *Zirconium in the Nuclear Industry: 13th International Symposium, ASTM STP 1423* 780–795 (2002).

118. Perkins, R. A. & Busch, R. A. Corrosion of Zircaloy in the Presence of LiOH. *Zirconium in the Nuclear Industry: 9th International Symposium, ASTM STP 1132* 595–612 (1991).

119. Jeong, Y. H., Baek, J. H., Kim, S. J., Kim, H. G. & Ruhmann, H. Corrosion characteristics and oxide microstructures of Zircaloy-4 in aqueous alkali hydroxide solutions. *J. Nucl. Mater.* **270,** 322–333 (1999).

120. Hillner, E. *Hydrogen absorption in Zircaloy during aqueous corrosion, effect of environment.* (Westinghouse Electric Corp. Bettis Atomic Power Lab., Pittsburgh, 1964).

121. Billington, D. S. & Crawford, J. H. *Radiation damage in solids.* (Princeton Univ. Press, 1961).

122. Kinchin, G. H. & Pease, R. S. The displacement of atoms in solids by radiation. *Reports Prog. Phys.* **18,** 1 (1955).

123. Onimus, F. *Course Material 'Metallurgy and properties of Zr alloys for nuclear applications' Chapter: 'Irradiation effect, effect on microstructure, crepp and growth' CEA, INSTN.* (2011).

124. Norgett, M. J., Robinson, M. T. & Torrens, I. M. A proposed method of calculating displacement dose rates. *Nucl. Eng. Des.* **33,** 50–54 (1975).

125. Osetsky, Y. N., Bacon, D. J. & de Diego, N. Anisotropy of point defect diffusion in alpha-zirconium. *Metall. Mater. Trans. A* **33,** 777–782 (2002).

126. Vérité, G., Willaime, F. & Fu, C. C. Anisotropy of the vacancy migration in Ti, Zr and Hf hexagonal close-packed metals from first principles. *Solid State Phenom.* **129,** 75–81 (2007).

127. Domain, C. Ab initio modelling of defect properties with substitutional and interstitials elements in steels and Zr alloys. *J. Nucl. Mater.* **351,** 1–19 (2006).

128. Pasianot, R. C. & Monti, A. M. A many body potential for α-Zr. Application to defect properties. *J. Nucl. Mater.* **264,** 198–205 (1999).

129. Christien, F. & Barbu, A. Effect of self-interstitial diffusion anisotropy in electron-irradiated zirconium: A cluster dynamics modeling. *J. Nucl. Mater.* **346,** 272–281 (2005).

130. Ackland, G. J., Wooding, S. J. & Bacon, D. J. Defect, surface and displacement-threshold properties of α-zirconium simulated with a many-body potential. *Philos. Mag. A* **71,** 553–565 (1995).

131. Griffiths, M. A review of microstructure evolution in zirconium alloys during irradiation. *J. Nucl. Mater.* **159,** 190–218 (1988).

132. Northwood, D. O. *et al.* Characterization of neutron irradiation damage in zirconium alloys — an international 'round-robin' experiment. *J. Nucl. Mater.* **79,** 379–394 (1979).

133. Griffiths, M. & Gilbert, R. W. The formation of c-component defects in zirconium alloys during neutron irradiation. *J. Nucl. Mater.* **150,** 169–181 (1987).

134. Holt, R. A. & Gilbert, R. W. c-Component dislocations in neutron irradiated zircaloy-2. *J. Nucl. Mater.* **116,** 127–130 (1983).

135. Griffiths, M. & Gilbert, R. W. The formation of c-component defects in zirconium alloys during neutron irradiation. *J. Nucl. Mater.* **150,** 169–181 (1987).

136. Garzarolli, F., Dewes, P., Maussner, G. & Basso, H.-H. Effects of high neutron fluences on microstructure and growth of Zircaloy-4. *Zirconium in the Nuclear Industry: 8th International Symposium, ASTM STP 1023* 641–657 (1989).

137. Gilbert, R. W., Farrell, K. & Coleman, C. E. Damage structure in zirconium alloys neutron irradiated at 573 to 923 K. *J. Nucl. Mater.* **84,** 137–148 (1979).

138. Williams, C. D., Adamson, R. B. & Olshausen, K. D. *Effects of boiling water reactor irradiation on tensile properties of Zircaloy*. (Conference: European conference on irradiation behaviour of fuel cladding and core component materials, Karlsruhe, F.R. Germany, 3 Dec 1974;, 1974).

139. Adamson, R. B. Effect of texture on stress corrosion cracking of irradiated zircaloy in iodine. *J. Nucl. Mater.* **92,** 363–365 (1980).

140. Fidleris, V. The irradiation creep and growth phenomena. *J. Nucl. Mater.* **159,** 22–42 (1988).

141. Adamson, R. B. Irradiation growth of Zircaloy. *Zirconium in the Nuclear Industry, ASTM STP 633* 326 (1977).

142. Adamson, R. B., Tucker, R. P. & Fidleris, V. High-temperature irradiation growth in Zircaloy. in *Zirconium in the Nuclear Industry: 5th International Symposium, ASTM STP 754* 208–234 (1982).

143. Murgatroyd, R. A. & Rogerson, A. Irradiation growth in annealed zircaloy-2. *J. Nucl. Mater.* **79,** 302–311 (1979).

144. Griffiths, M., Holt, R. A. & Rogerson, A. Microstructural aspects of accelerated deformation of Zircaloy nuclear reactor components during service. *J. Nucl. Mater.* **225,** 245–258 (1995).

145. Holt, R. A. Mechanisms of irradiation growth of alpha-zirconium alloys. *J. Nucl. Mater.* **159,** 310–338 (1988).

146. Zee, R. H., Carpenter, G. J. C. & Schmidt, F. A. Purification of zirconium by electrotransport processing. *Scr. Metall.* **18,** 489–493 (1984).

147. Zee, R. H., Rogerson, A., Carpenter, G. J. C. & Watters, J. Effect of tin on the irradiation growth of polycrystalline zirconium. *J. Nucl. Mater.* **120,** 223–229 (1984).

148. Tejland, P. *et al*. Oxidation Mechanism in Zircaloy- 2 — The Effect of SPP Size Distribution. *Zirconium in the Nuclear Industry: 17th International Symposium, ASTM STP 1543* 373–403 (2014).

149. Wadman, B., Andrén, H.-O., Nyström, A.-L., Rudling, P. & Pettersson, H. Microstructural influence on uniform corrosion of Zircaloy nuclear fuel claddings. *J. Nucl. Mater.* **200,** 207–217 (1993).

150. Hudson, D. & Smith, G. D. W. Initial observation of grain boundary solute segregation in a zirconium alloy (ZIRLO) by three-dimensional atom probe. *Scr. Mater.* **61,** 411–414 (2009).

151. Thuvander, M. & Andrén, H. O. Methods of quantitative matrix analysis of Zircaloy-2. *Ultramicroscopy* **111,** 711–714 (2011).

152. Wadman, B., Rolander, U. & Andrén, H.-O. Matrix composition of Zircaloy-4. *Le J. Phys. Colloq.* **48,** C6–299 (1987).

153. Wadman, B., Andrén, H.-O. & Rolander, U. Preferential field evaporation during atom probe analysis of Zircaloy-4. *Le J. Phys. Colloq.* **49,** C6–323 (1988).

154. Müller, E. W. Field Desorption. *Phys. Rev.* **102,** 618–624 (1956).

155. Blavette, D., Bostel, A., Sarrau, J. M., Deconihout, B. & Menand, A. An atom probe for three-dimensional tomography. *Nature* **363,** 432–435 (1993).

156. Miller, M. K., Cerezo, A., Hetherington, M. G. & Smith, G. D. W. *Atom probe field ion microscopy*. (Oxford Science Publications, 1996).

157. Miller, M. K. *Atom probe tomography: analysis at the atomic level*. (Kluwer Academic/Plenum Publishers, New York, 2000).

158. Forbes, R. G. Charge hopping and charge draining: Two mechanisms of field desorption. *Surf. Sci.* **102,** 255–263 (1981).

159. Kellogg, G. L. & Tsong, T. T. Pulsed-laser atom-probe field-ion microscopy. *J. Appl. Phys.* **51,** 1184 (1980).

160. Ernst, N. Experimental investigation on field evaporation of singly and doubly charged rhodium. *Surf. Sci.* **87,** 469–482 (1979).

161. Kingham, D. R. The post-ionization of field evaporated ions: A theoretical explanation of multiple charge states. *Surf. Sci.* **116,** 273–301 (1982).

162. Waugh, A. R. & Southon, M. J. Surface studies with an imaging atom-probe. *Surf. Sci.* **68,** 79–85 (1977).

163. Müller, E. W. The Atom-Probe Field Ion Microscope. *Rev. Sci. Instrum.* **39,** 83 (1968).

164. Müller, E. W. Energy deficits in pulsed field evaporation and deficit compensated atom-probe designs. *Rev. Sci. Instrum.* **45,** 1053 (1974).

165. Cameca Instruments LEAP 4000X Si. at <http://www.cameca.com/instruments-for-research/leap-si.aspx>

166. Brandon, D. G. The structure of field-evaporated surfaces. *Surf. Sci.* **3,** 1–18 (1965).

167. Chibane, K. & Forbes, R. G. The temperature dependence of evaporation field for Gomer-type field-evaporation mechanisms. *Surf. Sci.* **122,** 191–215 (1982).

168. Kellogg, G. L. Field ion microscope studies of single-atom surface diffusion and cluster nucleation on metal surfaces. *Surf. Sci. Rep.* **21,** 1–88 (1994).

169. Cerezo, A., Smith, G. D. W. & Clifton, P. H. Measurement of temperature rises in the femtosecond laser pulsed three-dimensional atom probe. *Appl. Phys. Lett.* **88,** 154103 (2006).

170. Miller, M. K. & Smith, G. D. W. An atom probe study of the anomalous field evaporation of alloys containing silicon. *J. Vac. Sci. Technol.* **19,** 57–62 (1981).

171. Southon, M. J. in *Field-Ion Microscopy* (eds. Hren, J. & Ranganathan, S.) 6–27 (Springer US, 1968).

172. Cerezo, A., Clifton, P. H., Gomberg, A. & Smith, G. D. W. Aspects of the performance of a femtosecond laser-pulsed 3-dimensional atom probe. *Ultramicroscopy* **107,** 720–5 (2007).

173. Arnoldi, L. *et al*. Energy deficit of pulsed-laser field-ionized and field-emitted ions from non-metallic nano-tips. *J. Appl. Phys.* **115,** 203705 (2014).

174. Thuvander, M. *et al*. Quantitative atom probe analysis of carbides. *Ultramicroscopy* **111,** 604–608 (2011).

175. Williams, C. A., Smith, G. D. W. & Marquis, E. A. Quantifying the composition of yttrium and oxygen rich nanoparticles in oxide dispersion strengthened steels. *Ultramicroscopy* **125,** 10–7 (2013).

176. Chen, Y. M., Ohkubo, T. & Hono, K. Laser assisted field evaporation of oxides in atom probe analysis. *Ultramicroscopy* **111,** 562–6 (2011).

177. Miller, M. K. & Smith, G. D. W. *Atom probe microanalysis: principles and applications to materials problems*. (Materials Research Society, 1989).

178. Henjered, A. & Norden, H. A controlled specimen preparation technique for interface studies with atom-probe field-ion microscopy. *J. Phys. E.* **16,** 617 (1983).

179. Larson, D. J. *et al*. Focused ion-beam milling for field-ion specimen preparation: *Ultramicroscopy* **75,** 147–159 (1998).

180. Larson, D. J. *et al*. Field-ion specimen preparation using focused ion-beam milling. *Ultramicroscopy* **79,** 287–293 (1999).

181. Miller, M. K., Russell, K. F. & Thompson, G. B. Strategies for fabricating atom probe specimens with a dual beam FIB. *Ultramicroscopy* **102,** 287–298 (2005).

182. Thompson, K. *et al*. In situ site-specific specimen preparation for atom probe tomography. *Ultramicroscopy* **107,** 131–9 (2007).

183. Miller, M. K. & Horton, J. A. An atom probe field ion microscope study of boron decorated boundaries in Ni_3Al. *Scr. Metall.* **20,** 789–792 (1986).

184. Horton, J. A. & Miller, M. K. Atom probe analysis of grain boundaries in rapidly-solidified Ni_3Al. *Acta Metall.* **35,** 133–141 (1987).

185. Jayaram, R. & Miller, M. K. An APFIM analysis of grain boundaries and precipitation in boron-doped NiAl. *Surf. Sci.* **266,** 310–315 (1992).

186. Valizadeh, S. *et al*. Effects of Secondary Phase Particle Dissolution on the In-Reactor Performance of BWR Cladding. *Zirconium in the Nuclear Industry: 16th International Symposium, ASTM STP 1529* 729–753 (2011).

187. Oskarsson, M., Ahlberg, E., Andersson, U. & Pettersson, K. Characterisation of pre-transition oxides on Zircaloys. *J. Nucl. Mater.* **297,** 77–88 (2001).

188. Tägstrom, P., Limbäck, M., Dahlbäck, M., Andersson, T. & Pettersson, H. Zirconium in the Nuclear Industry: Thirteenth International Symposium. *Zirconium in the Nuclear Industry: 13th International Symposium, ASTM STP 1423* 96 (2002).

189. Tejland, P. Microstructure Investigation of the Oxidation Process in Zircaloy-2 - The Effect of Intermetallic Particle Size. (PhD Thesis, Chalmers University of Technology, 2012).

190. Romero, J., Partezana, J., Comstock, R. J. & Hallstadius, L. Evolution of Hydrogen Pickup Fraction with Oxidation Rate on Zirconium Alloys. in *Submitted to TopFuel 2015* (2015).

191. Jeong, Y. H., Kim, H. G., Kim, D. J., Choi, B. K. & Kim, J. H. Influence of Nb concentration in the alpha-matrix on the corrosion behavior of Zr-xNb binary alloys. *J. Nucl. Mater.* **323,** 72–80 (2003).

192. Urbanic, V. F., Warr, B. D., Manolescu, A., Chow, C. K. & Shanahan, M. W. Oxidation and deuterium uptake of Zr-2.5 Nb pressure tubes in CANDU-PHW reactors. *Zirconium in the Nuclear Industry: 8th International Symposium, ASTM STP 1023* 20–34 (1989).

193. Wadman, B. Mechanisms of Uniform Corrosion of Zirconium Alloys in Water and Steam. (PhD Thesis, Chalmers University of Technology, 1993).

194. Hudson, D. Zirconium Oxidation on the Atomic Scale. (PhD Thesis, University of Oxford, 2010).

195. Ellingham, H. J. T. Reducibility of oxides and sulfides in metallurgical processes. *J Soc Chem Ind* **63,** 125–133 (1944).

196. Hyuk Baek, J. & Hwan Jeong, Y. Depletion of Fe and Cr within precipitates during Zircaloy-4 oxidation. *J. Nucl. Mater.* **304,** 107–116 (2002).

197. Atkins, P. & De Paula, J. *Elements of Physical Chemistry*. (Oxford University Press, 2012).

198. Lindgren, M. & Panas, I. Impact of additives on zirconium oxidation by water: mechanistic insights from first principles. *RSC Adv.* **3,** 21613–21619 (2013).

199. Ruehle, M. & Wilkens, M. Defocusing Contrast of Cavities - 1. Theory. *Cryst Lattice Defects* **6,** 129–140 (1975).

200. Ni, N. *et al*. Porosity in oxides on zirconium fuel cladding alloys, and its importance in controlling oxidation rates. *Scr. Mater.* **62,** 564–567 (2010).

201. Ni, N. *et al*. How the crystallography and nanoscale chemistry of the metal/oxide interface develops during the aqueous oxidation of zirconium cladding alloys. *Acta Mater.* **60,** 7132–7149 (2012).

202. Cabrera, N. & Mott, N. F. Theory of the oxidation of metals. *Reports Prog. Phys.* **12,** 163 (1949).

203. Yao, M. Y. *et al*. The effect of final annealing after β-quenching on the corrosion resistance of Zircaloy-4 in lithiated water with 0.04 M LiOH. *J. Nucl. Mater.* **435,** 63–70 (2013).

204. Griffiths, P. R. & De Haseth, J. A. *Fourier transform infrared spectrometry*. (John Wiley & Sons, 2007).

205. Banwell, C. N. & McCash, E. M. *Fundamentals of molecular spectroscopy*. (McGraw-Hill London, 1983).

206. Klimiankou, M., Lindau, R. & Möslang, A. Energy-filtered TEM imaging and EELS study of ODS particles and Argon-filled cavities in ferritic-martensitic steels. *Micron* **36,** 1–8 (2005).

207. Jäger, W. *et al*. Density and pressure of helium in small bubbles in metals. *J. Nucl. Mater.* **111-112,** 674–680 (1982).

208. McGibbon, A. J. Application of PEELS on a STEM to the problem of inert gas bubbles in solids. in *Institute of Physics Conference Series* **119,** 109–112 (IOP Publishing Ltd, 1991).

209. Herbig, M. *et al*. Atomic-scale quantification of grain boundary segregation in nanocrystalline material. *Phys. Rev. Lett.* **112,** 126103 (2014).

210. Menand, A., Cadel, E., Pareige, C. & Blavette, D. Three-dimensional atomic scale microscopy with the atom probe. *Ultramicroscopy* **78,** 63–72 (1999).